Enhancing Patient-Specific Trigeminal Nerve Visualization and Neuromodulation.

by

Sulagna Sahu

A Dissertation Presented in Partial Fulfillment
of the Requirements for the Degree
Doctor of Philosophy

Approved September 2023 by the
Graduate Supervisory Committee:

Rosalind Sadleir, Chair

Stephen H. Tillery
Sharon Crook
Scott Beeman
James Abbas

ARIZONA STATE UNIVERSITY

December 2023

ABSTRACT

Non-invasive visualization of the trigeminal nerve through advanced MR sequences and methods like tractography is important for studying anatomical and microstructural changes due to pathology like trigeminal neuralgia (TN), facial dystonia, multiple sclerosis, and for surgical pre-planning. The use of specific anatomical markers from CT, MPRAGE and cranial nerve imaging (CRANI) sequences, enabled successful tractography of patient-specific trajectory of the frontal, nasociliary, infraorbital, and mandibular nerve branches extending beyond the cisternal brain stem region and leading to the face. Performance of MPRAGE sequence together with the advanced T2-weighted CRANI sequence with and without a gadolinium contrast agent, was studied to characterize identification efficiency in smaller nerve structures in the extremities. A large FOV nerve visualization exam inclusive of the anatomy of all trigeminal nerve distal branches can be obtained within an acquisition time of 20 minutes using pre-contrast CRANI and MPRAGE. Post-processing with MPR and MIP images improved nerve visualization.

Transcranial electrical stimulation techniques (TES) have been used for the treatment of multiple neurodegenerative diseases. These techniques involve placing electrodes on the scalp with multiple peripheral branches of the trigeminal nerve crossing directly under that may be stimulated. This was studied through hybrid computational realistic axon models. These models also facilitated studying the effects of electrode drift during experiments on the recruitment of peripheral nerves. An optimal point of lowest threshold was found while

displacing the nerve horizontally i.e., the activation thresholds of both myelinated and unmyelinated axons increased when the electrodes were displaced medially and decreased to a certain extend when the electrodes were displaced laterally, after which further lateral displacement led to increase of thresholds. Inclusion of unmyelinated axons in the modeling provided the capability of finding maximum stimulation amplitude below which side effects like pain sensation may be avoided. In the case of F3 – F4 electrode montage the maximum amplitude was 2.39 mA and in case of RS – LS montage the maximum amplitude was 2.44 mA. Such modeling studies may be useful for personalization of TES devices for finding optimal positioning of electrodes with respect to target and stimulation amplitude range that minimizes side effects.

DEDICATION

Dedicated to my sister, Tanaya Sahu, for bearing the brunt of being the elder child and paving the way.

ACKNOWLEDGMENTS

I would like to express my heartfelt gratitude to my advisor, Dr. Rosalind Sadleir, for her support and guidance throughout my PhD journey. She always pushed me to delve deeper into the subject matter to develop a comprehensive understanding of topics. Her expertise and insightful feedback have been extremely instrumental in shaping my research and career pursuits. I would also like to thank the members of my dissertation committee, Dr. Stephen H. Tillery, Dr. James Abbas, Dr. Sharoon Crook, and Dr. Scott Beeman, for their valuable feedback which have helped me refine my research and improve the quality of my dissertation. I'm extremely grateful to neuroradiologist, Dr. Jeremy Hughes and his students Dane Hellwig and Chad Morrison for providing knowledge on neuroanatomy and verifying my trigeminal nerve studies.

I extend my gratitude to my parents, Ms. Simita Sahu and Mr. Srikanta Sahu and my older sister Tanaya Sahu for unconditional love and for always having my back. I am grateful to my partner Lee Bernard (to be Dr. soon) for lending a lot of positive energy during this journey and encouraging me to look at the bigger picture. I have been fortunate to have extremely supportive friends, and I would like to acknowledge Dattaraj, Nikita, Amit, Rujuta, and Mrudula for providing much needed respite in this journey.

All the people I met at Dr. Sadleir's lab have always been supportive. I would especially like to acknowledge previous colleague Dr. Munish Chauhan for his mentorship. I'm also

grateful to past and present lab members including Dr. Saurav Sajib, Dr. Neeta Kumar, Dr. Fanrui Fu, and Enock Boayke for their support.

I'm thankful to all the faculty and staff I met and friends I made at SBHSE who made this journey so much easier. I'm grateful to the people I met while conducting clinical studies at BNI, especially Sharmeen Maze for largely helping with MRI acquisitions. Finally, I would like to express my deep appreciation to the participants of my study, without whom this research would not have been possible.

Studies in this thesis were funded mostly by the National Institute of Health (NIH) award RF1MH114290 to Dr. Sadleir and partially by Defense Advanced Research Projects Agency (DARPA) award N66001-17-2-4018 to Dr. Tillery.

TABLE OF CONTENTS

Page

LIST OF TABLES

LIST OF FIGURES

Figure Page

FIGURE Page

FIGURE Page

FIGURE Page

FIGURE Page

ABBREVIATIONS

CRANI – Cranial Nerve Imaging

MPRAGE - Magnetization-Prepared Rapid-Acquisition Gradient-Echo

SNR – Signal to Noise Ratio

ROI – Region of Interest

MIP – Maximum Intensity Projection

MPR – Multi-Planar Reformatting

V1 – Ophthalmic nerve

V2 – Maxillary nerve

V3 – Mandibular nerve

FA – Fractional Anisotropy

DTI – Diffusion Tensor Imaging

HARDI – High Angular Resolution Diffusion Imaging

FOV – Field of View

TES – Transcranial Electrical Stimulation

tDCS - Transcranial Direct Current Stimulation

tACS - Transcranial Alternating Current Stimulation

MRG – McIntyre, Richardson, and Grill

AP – Action Potential

LC - Locus Coeruleus

FEM – Finite Element Modelling

TNS – Trigeminal Nerve Stimulation

PNS – Peripheral Nerve Stimulation

SON - Supraorbital Nerve

STN – Supratrochlear Nerve

ITN – Infratrochlear nerve

ION – Infraorbital nerve

ATN – Auriculotemporal nerve

ZTN – Zygomaticotemporal Nerve

BN – Buccal Nerve

RS – Right Supraorbital

LS – Left Supraorbital

AF – Activation Fraction

M_AF – Activation Fraction of Myelinated axons

UM_AF - Activation Fraction of Unmyelinated axons

CHAPTER 1

INTRODUCTION

In the ever-evolving landscape of medical imaging and neurology, the convergence of advanced imaging techniques and personalized neuromodulation therapies has ushered in a new era of precision medicine. This field holds immense promise for the development of patient-specific therapeutic interventions for neurological and psychiatric disorders. Neurodegenerative and psychiatric conditions, ranging from epilepsy and depression to Parkinson's disease and chronic pain, often present multifaceted challenges, necessitating a nuanced approach to diagnosis and treatment. Standard therapies, while valuable, may not always provide the desired outcomes, and their widespread application can lead to variability in responses among patients. It is in this context that the fusion of advanced MR techniques and neuromodulation emerges as a pioneering strategy. Such multi-disciplinary approaches may empower clinicians and researchers to move beyond the constraints of one-size-fits-all treatments and embark on a path towards personalized surgical planning, therapy, and dynamic treatment plan adjustment.

This thesis explores two main topics:

1.1. Imaging the trigeminal nerve.

Conventionally, T1-weighted sequences have been used as structural images to study cranial nerves, but newer T2-weighted structural scans have reported better

visualization of cranial nerves [1]–[3]. These structural MR imaging methods don't provide directional information and hence cannot be directly used to obtain trajectory of nerves. Diffusion tensor imaging (DTI) enables characterization of tissue microstructure directionality by imaging local water diffusion. Fiber tractography algorithms enable visualization of white matter tracts by reconstructing connectivity pathways from DTI data. Tractography of cranial nerves depends on multiple factors like region of interest (ROI) selection, fractional anisotropy threshold, tracking step size, tracking curvature threshold and type of tracking algorithm [4]–[7]. Some tractography studies have traced the 3D trajectory of the trigeminal nerve within the brainstem and in portions anterior to Meckel's cave in the brain [8]–[11]. In many studies, the occurrence of false positives and false negatives during tractography were reduced by using actual anatomical references through manual ROI placement [9], [12], [13]. Tract guiding ROIs from cadaveric studies/histology/other imaging modalities have been used as references [7]. The three branches of the trigeminal nerve, named as the ophthalmic, maxillary, and mandibular nerves exit the skull via the supraorbital, infraorbital, and mental foramina respectively. These foramina provide good reference waypoint ROIs for guiding tractography streamlines outside the brain. Nerve localization from MR images requires high resolution and signal to noise ratio (SNR). The CRANI sequence [3], [14] is a novel three dimensional TSE short-TI inversion recovery (STIR) black-blood acquisition that uniformly suppresses signal from fat,

muscle and blood enabling better peripheral nerve detection and can provide anatomical identification for tractography markers.

1.2. Neuromodulation of peripheral trigeminal nerves.

Noninvasive transcranial electrical stimulation (TES) methods are increasingly being tested to alter cognition and treat diseases [15]. Neuromodulation is the alteration of neural activity by delivering electrical or pharmaceutical agents to the nervous system [16], [17]. Stimulation of the trigeminal nerve has been used successfully in clinical trials to treat epilepsy, ADHD, migraine, and other psychiatric conditions [18]–[22]. Other non-invasive neuromodulation methods include transcranial direct current stimulation (tDCS) which uses weak direct currents targeting cortical neurons [23] and transcranial alternating current stimulation (tACS) which use alternating currents targeting endogenous oscillations of the brain [24], [25]. Administration of tDCS and tACS involves injecting current through electrodes placed on the scalp. However, current flow modelling studies have shown that skull and soft tissue act as a barrier to current flow [26]–[28], for example, Voroslakos et al. [29] performed experiments on live rats and cadaver brains and found that only about 25% of scalp-applied currents enters the brain and maximum current density can be seen in foraminal and extracranial regions. This could lead to excitation of cranial nerves near the electrodes, and these effects possibly interact with other neuromodulation effects of transcranial electrical stimulation (TES) methods [30]. While it has been found that stimulation of a specific cranial nerve could

not be achieved through non-invasive stimulation, a targeted set of nerves could be successfully recruited [31] for example stimulation through electrodes on the forehead activate both trigeminal and optic nerves. As afferent cranial nerve axons project directly to higher order brain networks, studying their response to non-invasive stimulations can provide a better mechanistic understanding of stimulation therapies.

1.3. Research needs

Non-invasive visualization of the trigeminal nerve can provide insights about abnormalities affecting the cranial nerves and aid in diagnosis and treatment planning for multiple diseases like trigeminal neuralgia (TN), multiple sclerosis of the nerve, and focal dystonia [32]. The CRANI sequence developed by Cruyssen et al. [14] that has shown excellent visualization of extraforaminal trigeminal nerves. Diffusion tractography is a specialized MRI technique that utilizes diffusion-weighted imaging (DWI) data to visualize and map the fiber pathways in the brain and can be used to investigate the anatomical connectivity of cranial nerves and study microstructural changes occurring due to pathology [12], [33], [34].

To date, there have been no diffusion tensor imaging (DTI) based studies using subject-specific data where the entire courses of trigeminal nerve branches have been tracked outside the cisternal brain region. The branches of the trigeminal nerve exit the skull via the supraorbital, infraorbital, and mental foramina into the face. The location of these foramina and other extra foraminal anatomical markers seen using advanced CRANI images, provide reference information for guiding DTI tractography. Using high SNR and

high contrast imaging, in conjunction with identification of foramina and anatomical markers, should provide a means of tracing trigeminal nerve branches from origin in brainstem to terminations with high accuracy.

Multiple TES method are currently being investigated for therapeutic purposes [15], however, it is possible that existing external electrical stimulation methods have additional neuromodulation effects on cranial nerves and their projections [30], [31] and have not been studied extensively. Response of nerves to stimulation can be affected by multiple factors like nerve location and shape, electrode shape and location, stimulation waveform and duration, which need optimization [35]–[37]. The extent to which peripheral branches of the trigeminal nerve get activated during TES needs to be further investigated. Variability seen during clinical administration of stimulation currents due to nerve and electrode movement and excitability of peripheral nerve fibers can be studied through realistic computational models to understand the need for patient-specific imaging-based optimization of neuromodulation parameters.

The specific aims investigated in this thesis are:

1.3.1. Visualization of the trigeminal nerve outside the brain.

To perform probabilistic tractography, we acquired MPRAGE, DTI and CRANI images of human subjects. Foramina location and peripheral anatomical markers for tractography guidance were informed through multi-modality co-registration of MR and CT images and intra-subject linear registration of MPRAGE and CRANI data. We also studied the

efficiency of characterizing different distal trigeminal nerve branches using a combination of MPRAGE and CRANI sequence.

1.3.2. Development of computational models to study trigeminal nerve stimulation (TNS).

We created a computation system by first simulating electric fields induced from external applied currents in a realistic finite element model of the head. This was combined with NEURON models of intracranial trigeminal nerve axons with geometry obtained from tractography and tested with pulsatile waveforms. In a second step, hybrid models including realistic peripheral trigeminal nerve fascicles were created. The activation fractions of the peripheral nerve fascicles in the presence of candidate TES waveforms were studied to see changes in excitability due change of nerve location and electrode drift and established the importance of patient-specific modeling.

CHAPTER 2

BACKGROUND

The main concepts used in conducting research included in this thesis are discussed below:

2.1. Trigeminal nerve – a discussion on anatomy.

The trigeminal nerve is the fifth and largest cranial nerve. It is responsible for providing sensory information from the face and controlling the motor functions of the muscles involved in chewing and speaking [38]. It originates from the brainstem, specifically from the trigeminal nucleus located in the pons which also houses the locus coreleus [39]. It has both sensory and motor components, with three main branches that innervate different areas of the face [38]–[40] (Figure *1*).

2.1.1. Ophthalmic nerve (V1):

This is the first branch of the trigeminal nerve and is responsible for sensory input from the upper face. It originates from the trigeminal ganglion, which is a collection of sensory cell bodies located in the middle cranial fossa within the skull. From there, it enters orbit through the superior orbital fissure, which is a bony opening in the skull located at the posterior part of the orbit. Within the orbit, the ophthalmic nerve divides into several branches that supply specific areas of the upper face. These branches include:

- Frontal nerve: This branch is responsible for providing sensory innervation to the forehead and scalp.
- Supraorbital nerve: It emerges from the frontal nerve and provides sensory innervation to the skin of the forehead, scalp, and the upper eyelid.
- Supratrochlear nerve: It arises from the frontal nerve and provides sensory innervation to the skin of the forehead and the upper eyelid near the nose.
- Lacrimal nerve: This branch innervates the lacrimal gland, which produces tears, as well as the skin of the lateral part of the upper eyelid.
- Nasociliary nerve: This is a major branch of the ophthalmic nerve that supplies sensory innervation to various structures in the orbit and face. It gives rise to several smaller branches, including the anterior ethmoidal nerve, which supplies sensation to the nasal cavity and septum, and the long ciliary nerves, which provide sensory innervation to the cornea and iris of the eye.

2.1.2. Maxillary nerve (V2) [38], [39]:

The second branch of the trigeminal nerve provides sensory innervation to the middle part of the face. It also originates from the trigeminal ganglion and exits the skull through the foramen rotundum, which is a bony opening situated in the sphenoid bone. After which, the maxillary nerve enters the pterygopalatine fossa, a small space located behind the maxilla (cheekbone). Within this fossa, the maxillary nerve gives rise to several branches that supply specific areas of the middle face:

- Infraorbital nerve: It is a major branch of the maxillary nerve and provides sensory innervation to the lower eyelid, upper lip, and the skin of the cheek.
- Zygomatic nerve: The maxillary nerve gives off zygomatic branches that innervate the skin over the zygomatic (cheek) bone.
- Superior alveolar nerves: These branches provide sensory innervation to the upper teeth and gums.
- Middle superior alveolar nerve: It supplies sensation to the premolar teeth and surrounding tissues.
- Anterior superior alveolar nerve: This branch provides sensory innervation to the canine and incisor teeth, as well as the adjacent tissues.
- Posterior superior alveolar nerve: It innervates the molars and the surrounding structures.

The maxillary nerve also gives rise to other smaller branches, such as the nasopalatine nerve (innervating the nasal septum and palate) and the infraorbital nerve branches (supplying the skin of the lower eyelid, side of the nose, and upper lip).

2.1.3. Mandibular nerve (V3) [38], [39]:

This is the third and largest branch of the trigeminal nerve and is responsible for both sensory and motor functions related to the lower part of the face. The

mandibular nerve originates from the trigeminal ganglion and exits the skull through the foramen ovale, which is a bony opening situated in the greater wing of the sphenoid bone. After which, the mandibular nerve gives rise to several branches that innervate specific regions and structures:

- Buccal nerve: This branch provides sensory innervation to the skin of the cheek, as well as the buccal mucosa (inner lining of the cheek).
- Masseteric nerve: This branch is responsible for supplying motor innervation to the masseter muscle, enabling its contraction, and facilitating the essential function of mastication (chewing and biting).
- Auriculotemporal nerve: It supplies sensory innervation to the external ear and the skin over the temple area.
- Lingual nerve: This branch provides sensory innervation to the anterior two-thirds of the tongue, including taste sensation, and the floor of the mouth.
- Inferior alveolar nerve: It supplies sensory innervation to the lower teeth, lower gums, and the chin. It also gives off the mental nerve, which provides sensory innervation to the skin of the lower lip and chin.

In summary, the trigeminal nerve first exits the skull through three main openings called foramina: the superior orbital fissure (for V1), the foramen rotundum (for V2), and the foramen ovale (for V3). All the trigeminal nerve branches further divide into smaller peripheral nerves and reach their respective sensory targets which provide sensory innervation to the entire face.

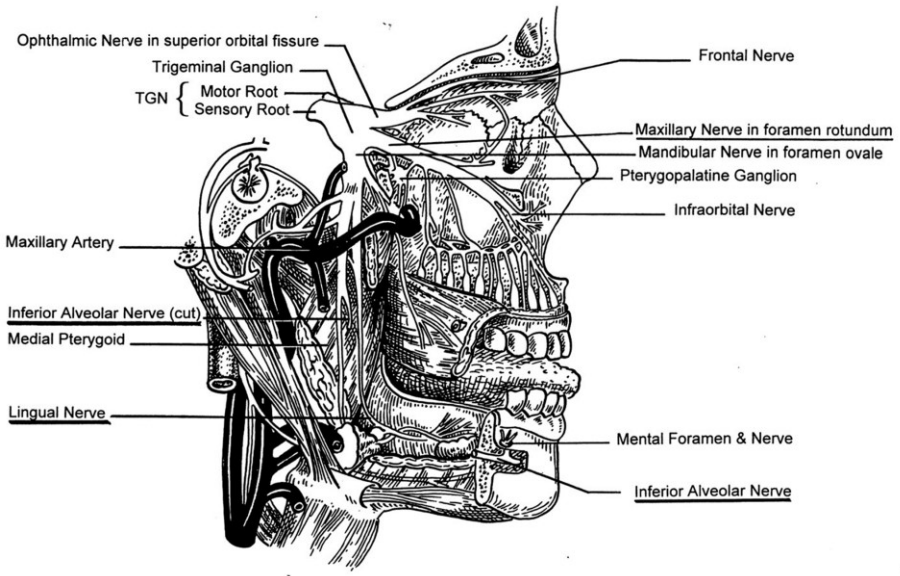

Figure 1 Anatomy of the trigeminal nerve representing the foramen where the sub-branches exit the skull. Figure adapted from research by Marur et al. [38]

Visualizing the location and geometry of cranial nerves is useful for understanding various pathologies relating to cranial nerves, and for preoperative surgical planning and image-guided surgery [41], [42].

2.1.4. Physiology and pain pathway

The ophthalmic and maxillary branches of trigeminal nerve are entirely sensory whereas the mandibular branch has mixed motor and sensory functions [39]. The nerves fibers consist of a mix of myelinated and unmyelinated axons of which all the unmyelinated axons are sensory afferents meaning they convey nociceptive (pain), temperature, and

touch signals from the face and head to the brain and are crucial for detecting potentially harmful or damaging stimuli in these regions. Efferent axons in the trigeminal nerve branches are myelinated. Shown below (Figure 2) is the ascending pain pathway (taken from paper by Bista et al. [43]) associated with unmyelinated axons in peripheral trigeminal nerves.

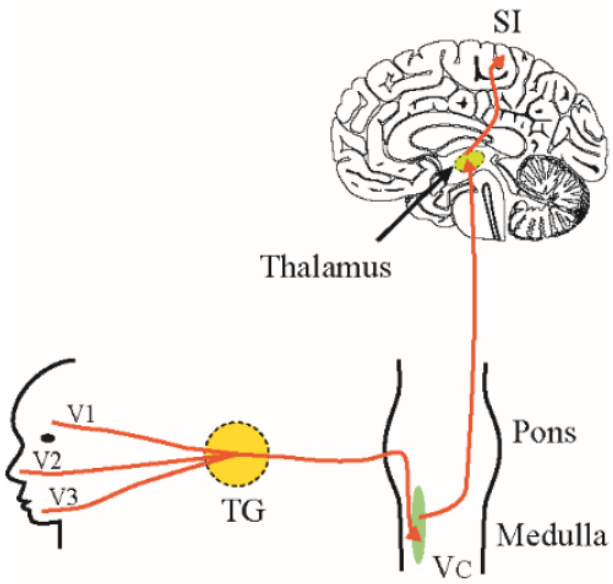

Figure 2 Ascending pathway involved in transmitting pain stimuli. A pain stimulus maybe caused due to environmental factors or due to external current stimulation activating the afferent axons. Figure taken from [43].

The trigeminal pain pathway involves the transmission of pain sensations from the face and mouth through the afferent unmyelinated axons in the three peripheral nerve branches (V1, V2, and V3) of the trigeminal nerve [44]. The cell bodies of sensory neurons are in the trigeminal ganglion (TG). They send their projections centrally to

synapse with second-order neurons in the trigeminal spinal nucleus caudalis (VC). These second-order neurons then ascend to reach the thalamus. Within the thalamus, nociceptive information is further relayed to the primary somatosensory cortex (SI), where the brain processes and interprets the painful stimuli [43], [45].

2.2. MR imaging of the trigeminal nerve

2.2.1. Magnetic Resonance Imaging (MRI)

MRI is a medical imaging technique based on the principles of nuclear magnetic resonance used to visualize the internal structures of the body in detail [46], [47]. In the presence of a strong magnetic field (usually provided by superconducting magnets), hydrogen nuclei (protons) align themselves with this magnetic field. When radiofrequency (RF) pulses are applied at the resonant frequency of these nuclei (known as the Larmor frequency), they temporarily flip out of alignment. After the RF pulse is turned off, the excited protons return to their equilibrium alignment with the magnetic field. This return to equilibrium is characterized by two relaxation processes [47]:

- T1 (Spin-Lattice Relaxation): This is the process by which protons recover longitudinally along the magnetic field. It determines the image contrast in T1-weighted images.
- T2 (Spin-Spin Relaxation): This is the process by which protons lose phase coherence as they return to equilibrium, causing signal dephasing. It determines the image contrast in T2-weighted images.

The returning signals from the protons are detected by coils in the MRI machine. These signals are weak and may require sophisticated receiver coils and amplification. To create an image, MRI uses magnetic field gradients, which are superimposed on the main magnetic field. These gradients encode spatial information in the MRI signal. By varying the strength and timing of these gradients, it's possible to differentiate signals from different locations within the body and produce data in the frequency domain (k-space) which can then be transformed into the spatial domain to produce an image.

Most equations describing the behavior of nuclear magnetic spins in a magnetic field and the resulting magnetization are derived from the Bloch equations [48], [49]. Bloch assumed that the individual nuclei in a sample could be represented by a single vector M, now called net magnetization (A/m). In the lab coordinates, M (A/m) is a vector rotating in space and can be resolved into three time-dependent orthogonal components: $M_x(t)$, $M_y(t)$, and $M_z(t)$. Bloch used T1 and T2 relaxation constants to account for signal decay and restoration of equilibrium of nuclear magnetization after generation of the NMR signal. Following are the Bloch equations:

Equation 1

$$M_x(t) = M_0 e^{-\frac{t}{T2}} \sin \omega t$$

Equation 2

$$M_y(t) = M_0 e^{-\frac{t}{T2}} \cos \omega t$$

Equation 3

$$M_z(t) = M_0(1 - e^{-\frac{t}{T1}})$$

Where $M_x(t)$ and $M_y(t)$ are the transverse components and $M_z(t)$ is the longitudinal component, M_0 is the equilibrium magnetization, and ω is the angular frequency (rad/sec).

2.2.2. Diffusion imaging.

Diffusion weighted imaging (DWI) is a technique which maps displacement of water molecules in a subject and provides helpful information about tissue microstructure and orientation [50], [51]. Diffusion tensor imaging (DTI) describes diffusion of water molecules using diffusion tensors which provide the magnitude and degree of anisotropy and the orientation of diffusion [52]. In practice, DWI is commonly used in clinical and research settings to investigate tissue properties, where it can be used to detect and characterize conditions like stroke, tumors, and demyelinating diseases [33], [53], [54].

The Stejskal-Tanner (ST) equation [55] is a fundamental equation in the field of DWI. This equation describes the relationship between the diffusion-weighted MRI signal and the properties of the diffusion process being measured.

Equation 4

$$S = S_0 e^{-bD}$$

Equation 5

$$b = \gamma^2 G^2 \delta^2 (\tau - {}^{\delta}/_{3})$$

Where, S is the signal strength with the presence of pulse-field gradients, S_0 is the signal strength without any gradients, G is the strength of gradient used (T/m), δ is the duration for which the gradient is played (s), τ is the delay between the two gradient applications (s), b is the weighting factor (s/mm^2) and D is the diffusion coefficient (m^2s^{-1}).

The following information can be inferred from the ST equations:

- The signal intensity S is lower when diffusion weighting is applied compared to the baseline signal S_0. The extent of this signal attenuation is determined by the diffusion coefficient D and the diffusion weighting factor b.
- The diffusion coefficient D represents the rate of molecular diffusion within the tissue and measures how fast water molecules diffuse in a particular direction.
- The diffusion weighting factor b is determined by the MRI sequence parameters, including gradient strength, gradient duration, and time between the application of the gradients. Higher values of b result in stronger diffusion weighting and greater signal attenuation.
- By acquiring multiple images with different b-values, the data can be fit to the Stejskal-Tanner equation and to calculate the apparent diffusion coefficient D. This allows for the quantification of tissue diffusivity, which can be used to study tissue microstructure and detect abnormalities.

2.3. Noninvasive brain stimulation

2.3.1. Neurophysiology

The human nervous system consists of two main components [56], [57]:

- Central Nervous System (CNS): This includes the brain and spinal cord. The brain is the control center of the body, responsible for processing information, making decisions, and coordinating various functions. The spinal cord is a long, thin bundle of nerves that extends down from the brain and serves as a communication pathway for the rest of the body.
- Peripheral Nervous System (PNS): The PNS includes all the nerves and ganglia (clusters of nerve cell bodies) outside the brain and spinal cord. It is further divided into two main components: Somatic nervous system which controls voluntary muscle movements and transmits sensory information from the body to the CNS, and autonomic nervous system which regulates involuntary bodily functions, such as heart rate, digestion, and respiratory rate.

All the components work together to transmit signals, process information, and regulate various bodily functions, allowing the body to respond to its environment.

2.3.2. Mechanisms behind tDCS and tACS

Low amplitude direct current (DC) stimulation is not strong enough to generate an action potential but rather works in bringing a neuron closer to or farther from firing by de- or hyperpolarizing its resting membrane voltage. A positive (anodal) current facilitates depolarization and hence increases excitability, and a negative (cathodal) current facilitates hyperpolarization of neurons decreasing excitability. Induction of plasticity is mostly

achieved by modulating synaptic plasticity between the pre-synaptic neuron and the post-synaptic neuron in the form of a long-term potentiation (LTP)- or long-term depression (LTD)-like plasticity.

This concept forms the basis of transcranial Direct Current Stimulation (tDCS) methods which have seen clinical usage in the treatment of depression, migraine, epilepsy, modulation of learning in motor functions [25], [35]. Response of a single neuron to tDCS currents are dictated by factors like orientation of neuron with respect to electric field, and morphology. It is also seen that different sub-populations of neurons in the brain are modulated differently depending on receptor subtypes and the concentration and activity of their modulators.

Glutamate is a neurotransmitter involved in most excitatory processes in the central nervous system [58]. NMDA and AMPA are two types of ionotropic glutamate receptors (present on the post- synaptic cell) [59]. Anodal DC stimulation incrementally depolarizes somatic membranes leading to release of glutamate from the presynaptic cell. Low-amplitude DCS may influence the NMDA receptor activity by altering the membrane potential of neurons. When a weak electrical current is applied, it can change the resting membrane potential of neurons, making them more likely to depolarize. This depolarization can facilitate the activation of NMDA receptors, which are essential for the induction of LTP.

During the start of anodal DC stimulation, NMDA receptor is blocked (NMDA is unblocked only during coincident presence of both glutamate and postsynaptic

depolarization) and excitatory post synaptic potential (EPSP) is mediated only by AMPA type receptors. On continued application of DC stimulation, EPSPs due to AMPA receptors depolarize the post-synaptic cell. Due to continued release of glutamate from input pre-synaptic neuron, the NMDA receptors on the post-synaptic neuron becomes active leading to the influx of Ca2+ ions which increase synaptic strength by a cascade of biochemical events and hence leading to LTP. Activation of Ca2+ dependent protein kinases lead to the addition of more AMPA type receptors into the postsynaptic membrane. This increases responsiveness of postsynaptic neurons to incoming glutamate and causes larger summation of EPSPs. This makes the synapse stronger and leads to further LTP.

Parra et al. [60] in their research have shown that coherent polarization of a population of neurons through extracellular fields can further increase the coherence of the population's firing times. If DC stimulation is applied to a group of neurons, their neural activity generates extracellular field potentials which can further coherently influence more groups of neurons. This can lead to the progressive polarization of a fully connected network leading to LTP.

One of the primary mechanisms proposed for tACS is through neural oscillations. Neural oscillations are rhythmic patterns of electrical activity in the brain, such as alpha (8-12 Hz), beta (13-30 Hz), and gamma (30-80 Hz) oscillations [61]. By delivering electrical currents at specific frequencies, tACS aims to synchronize or entrain these neural oscillations in the target brain region. This entrainment may influence cognitive processes that are associated with those particular frequencies [61], [62]. Another proposed mechanism for tACS is

through influencing the firing rates of neurons in the stimulated brain area. The alternating current can cause neurons to fire at the same frequency as the stimulation, facilitating communication between neurons within that frequency band. This modulation of firing rates may enhance the processing of information related to the stimulated frequency [61], [62]. Similar to tDCS, tACS is also considered to have network-level effects and plasticity-based effects [63]. Although the understanding of many of these mechanisms is still evolving, and more research is needed to fully optimize the use of tDCS and tACS.

2.3.3. History of neuron modelling

The first models studying axons were based on mathematical equations that described the passive electrical properties of axons and focused on the cable theory, which treats the axon as a transmission line. The groundbreaking work of Alan Hodgkin and Andrew Huxley led to the creation of the Hodgkin-Huxley model [64], which described the dynamics of the action potential in unmyelinated axons. This model laid the foundation for understanding the role of ion channels in axonal conduction and paved the way for future modelling. Frankenhaeuser and Huxley [65] extended the Hodgkin-Huxley model to myelinated axons. This model considered the influence of the myelin sheath and nodes of Ranvier on action potential propagation. In the early 2002s McIntyre, Richardson, and Grill [66] built a double cable model commonly known as the MRG model which was especially useful for studying the propagation of action potentials (electrical signals) along myelinated axons. It incorporated more complex membrane dynamics with explicit representations of

the nodes of Ranvier, paranodal, and internodal sections of the axon, as well as a finite impedance myelin sheath and has been instrumental in studying the effects of electrical stimulation on axonal conduction. In recent years, computational models of both unmyelinated and myelinated axons have become increasingly biophysically detailed and account for the specific ion channel distributions along the axon and their roles in action potential initiation and propagation [67]–[69]. They also account for multiple parameters like structural biology, temperature dependence and other factors affecting axonal conduction.

The simpler form of modeling an active fiber involves solving the cable equation with Hodgkin-Huxley elements [64]. More complex nerve models can be broken down to basic cable equation methods with more terms representing currents due to added ionic channels.

Described below is a simple modeling approach to solving cable equation for a straight fiber in the presence of an external point source illustrating the basics of modelling neural stimulation.

Starting with a passive cable, the axial current (A) flowing inside the axon is given by:

Equation 6

$$r_i I_i = -\frac{\partial \mathrm{V}}{\partial \mathrm{x}}$$

Using theory of conservation of current, membrane current per unit length (A/m) is:

Equation 7

$$i_m = \frac{\partial \mathrm{I}_i}{\partial \mathrm{x}}$$

Combining the previous equations, membrane current per unit length (A/m) is:

Equation 8

$$i_m = c_m \frac{\partial \mathrm{V}}{\partial \mathrm{t}} + \frac{V}{r_m}$$

Combining the previous equations, the cable equation is:

Equation 9

$$\lambda^2 \frac{\partial^2 V}{\partial^2 x} - V = \tau \frac{V}{\partial T}$$

Where λ and τ represent the length constant and time constant respectively, c_m is the cytoplasmic capacitance (F/m) and r_m is the membrane resistance (ohm.m).

In the presence of an external electric field (as produced by point source), let the component of external electric field parallel to the straight axon be given by $e_x(x, t)$ (gradient of vector potential).

Then the electric field inside the axon can be written as a summation of the gradient of intracellular potential and parallel component of external electric field $e_x(x, t)$ (V/m) [70]:

Equation 10

$$E_i = -\frac{\partial V}{\partial x} + e_x(x, t)$$

The updated equation for axial current (A) is:

Equation 11

$$r_i I_I = -\frac{\partial V}{\partial x} + e_x(x,t)$$

Combining all the above equations the, updated cable equation describing an external point source is [70]:

Equation 12

$$\lambda^2 \frac{\partial^2 V}{\partial^2 x} - V = \tau \frac{V}{\partial T} + \lambda^2 \frac{\partial e_x}{\partial x}$$

This equation shows how peaks of membrane potential can be found where spatial gradient of extracellular electric field parallel to the axon is maximum.

The assumptions used in modeling this equation are [70], [71]:

- A low frequency (< 1Mhz) the medium is assumed to be resistive.
- Intracellular potential is only a function of the axon length and is not influenced by axon's own extracellular potential.
- The derived equation only accounts for axial electric field gradients, radial field gradients from external source do not influence action potential generation. Also, electric field from external stimulus is considered not to be distorted by the presence of the axon.

- The model is compartmentalized such that the individual compartment length is much smaller than the total length of axon and hence the extracellular potential at each compartment is constant throughout.

2.3.4. Computational modelling.

Simulations provide an effective platform to study neuromodulation effects and repeatability. Recent computational models have used realistic head models obtained by segmenting patient specific MRI data into individual tissue types [27], [36]. Biophysical nerve models can be built using software like NEURON (neuron.yale.edu) and GENESIS (genesis-sim.org) which predict the effects of stimulation using seminal works presented by Hodgkin – Huxley [64], [72], Roth [70], and McNeal [71]. A hybrid computational study of electrical stimulation generally consists of two parts: 1. use of finite element modeling (FEM) to generate induced electric potential maps in a realistic head model and 2. applying these maps to a computational NEURON model to study the effects on neural activity. NEURON and GENESIS modeling platforms assume quasi-static behavior and ignore the effects of ephaptic coupling.

During stimulation experiments, variables like nerve anatomy, electrode shape and location, as well as variation in stimulation waveforms can affect nerve excitability outcomes like activation fraction and required stimulus current and can be studied using simulation models [73]. Computational models also serve as a valuable tool for designing

and assessing diverse electrode types, including variations in geometry, materials, and the placement of active sites and also facilitate the exploration of responses of neural models when subjected to different electrical current waveforms [73], [74].

CHAPTER 3

3D CRANI AND 3D MPRAGE CAN VISUALIZE DISTAL TRIGEMINAL NERVE SEGMENTS: AN ANATOMICAL STUDY.

The trigeminal nerve is a mixed motor and sensory nerve which makes connections to higher order nuclei in the brainstem that act as sensory regulators, leading to the arousal, regulation, and coordination of neurobehavioral engagement with the environment [39], [75]. The trigeminal nerve is the largest cranial nerve and its branches the ophthalmic nerve (V1), the maxillary nerve (V2) and the mandibular nerve (V3) provide innervation to the face and are susceptible to damage from multiple pathologic conditions including neoplasm, inflammation, neurovascular compression, necrosis, infection, and trauma from surgical procedures [76],[77].

Magnetic resonance neurography (MRN) imaging sequences are designed to enhance visualization of cranial nerves (CN). MRN can aid in diagnosing nerve pathology like trigeminal neuralgia [41] and perineural tumor spread in cases of head and neck carcinoma [78], [79] and facilitate preoperative surgical planning, image-guided surgery, and post-operative care [78], [80]. However, large multi-center studies exploring the clinical usefulness and reproducibility of newer MRN sequences are lacking.

Nerve localization from MR images requires high spatial resolution and contrast and high signal-to-noise-ratio (SNR). MPRAGE [81] is a widely used and accessible clinical MR

sequence, and a recent PubMed search identified more than 650 research articles which have used MPRAGE for head and neck imaging. Although 3D T1-weighted sequences like the MPRAGE sequence have been used clinically to study cranial nerves, newer 3D T2-weighted sequences have reported improved contrast between nerve and surrounding tissue. Blitz et al. [1], [82] compared the visualization of cranial nerves using T2-weighted constructive interference in steady state (CISS) MR scans with and without contrast and found that while the intracranial regions of nerves were detected equally well on both scans, extraforaminal regions were better identified on contrast enhanced scans. Zhang et al.[83] used the 3D reversed fast imaging with steady-state precession (FISP) (3D-PSIF) with diffusion-weighted MR sequence and were able to identify extracranial trigeminal nerve branches, but could not visualize nerves in the cavernous sinus region. The 3D short tau inversion – turbo spin echo sequence for extraforaminal cranial nerve imaging (CRANI) developed by Cruyssen et al.[14] is a novel short-TI inversion recovery (STIR) black-blood acquisition that uniformly suppresses signal from fat, muscle and blood, enabling excellent visualization of extraforaminal cranial nerves. Although such sequences are T2-weighted, they use steady state free precession mechanisms which allow for some T1-weighting and hence may be enhanced using T1 contrast agents to improve cranial nerve visualization [82].

3.1. Aims

In this research, we conducted a clinical study to replicate CRANI imaging and investigated visualizing the trigeminal nerve using a combination of 3D CRANI and 3D

MPRAGE with and without gadolinium contrast enhancement. The optimal combination of sequences suitable for imaging distal branches of the V1, V2, and V3 segments were identified. We also furthered anatomical understanding of the nerve by locating a set of anatomical markers useful for detection of V1 and V2 branches on MRN. This study also validated the use of the novel MRN sequence CRANI for clinical usage in cranial nerve imaging applications.

3.2. Materials and Methods:

3.2.1. Patient population:

The study was approved by the Arizona State University Institutional Review Board. Seven healthy human subjects (4 female and 3 male) aged 18-26 were recruited after screening for health conditions including neurological disorders, history of renal disease, cancer, hypertension, diabetes, and liver disease. Selected subjects participated in an information session where their informed consent was obtained before proceeding to imaging.

3.2.2. MRI acquisitions and post-processing:

All participants underwent MR imaging in a 3 Tesla scanner (Phillips Ingenia) equipped with a 32-channel head coil. The imaging protocol consisted of pre-and post-contrast MPRAGE and CRANI. To achieve contrast enhancement, 0.1 mmol/Kg of Gadavist

(Bayer AG, Germany) was injected by the MRI technician following the pre-contrast MPRAGE and CRANI sequences. Precise imaging parameters of the sequences are described in table 1.

Table 1 Acquisition parameters for MPRAGE and CRANI

	MPRAGE	CRANI
Basic MRI technique	Multi-shot gradient echo	Turbo spin echo
TR/TE (ms)	40/4	2300/150
FOV (AL/RL/FH mm)	224/224/224	220/220/190
Acquired voxel size (AL/RL/FH mm)	0.9/0.9/0.9	0.9/0.9/0.9
Slice thickness (mm)	0.9	0.9
Acquisition time (min:sec)	06:22	11:31
TFE factor	56	N/A
TSE factor	N/A	45
Additional techniques		• MSDE "black blood" pulse • Pseudo steady state sweep

Post-processing of the scans involved multi-planar reformat (MPR) and maximum intensity projection (MIP) presentation (5 mm thickness) to visualize continuous nerve trajectories. To perform quantitative analysis of image quality, a region of interest (ROI) with a minimum size of five pixels was drawn on the optic nerve in an axial slice for each subject. The optic nerve was chosen due to its large size and easy detection. SNR calculation was calculated as 0.67 × (mean signal intensity of ROI) / (standard deviation of noise), with noise measured using multiple air ROIs [84]. A paired t-test analysis was used to compare SNR values in pre- and post- contrast images.

3.2.3. Nerve identification evaluation:

All images were transferred to an external PACS (ambrahealth.com) for imaging analysis. Three readers (Zachary Morrison (ZM), first-year radiology resident; Dane Hellwig (DH), neuroradiology fellow; and Jeremy Hughes (JH), neuroradiology attending) with 1, 5, and 13 years of experience interpreting head and neck imaging, respectively independently graded nominated extracranial branches of the V1, V2 and V3 segments bilaterally on the following sequences: MPRAGE without contrast, MPRAGE with contrast, CRANI without contrast and CRANI with contrast. All three readers received training to identify the neuroanatomy and course of the distal branches of the V1, V2, and V3 segments and standardize nerve visualization grading prior to reviewing study patients. The following branches were graded: V1 (frontal, nasociliary and lacrimal nerves); V2 (infraorbital, zygomatic, and greater palatine nerves); and V3 (masseteric, buccal, auriculotemporal, lingual and inferior alveolar nerves). Axial source images, as well as sagittal and coronal MPRs were used and the paths of the V1, V2, and V3 branches were determined by referencing anatomic atlases and tracing nerves between anatomic landmarks. Where possible, the nerves were tracked posteriorly to their respective foramina to ensure distinction between distal nerve segments and adjacent vasculature although at times. In some cases of smaller or discontinuous distal nerves, this was not possible. As in the system adopted by Fujii et al. [85], an intermediate point for each V1 and V2 nerve branch was determined (Table 2). Intermediate points used for V3 branches were taken from previously published works [85], [86].

Table 2 Neuroanatomical markers are used for visualization of V1 and V2 branches.

Nerve Branch	Intermediate Anatomical Marker
Frontal	The point at which the nerve courses between the levator palpabrae superioris and the orbital roof periosteum at the level of the posterior aspect of the globe.
Lacrimal	The point at which the nerve crosses the ophthalmic artery as it courses towards the upper margin of the lateral rectus muscle.
Nasociliary	The point at which the nerve courses beneath the superior oblique muscle at the level of the posterior border of the globe.
Infraorbital	The point at which the nerve crosses the posterior margin of the globe while coursing within the infraorbital foramen.
Zygomatic	The point at which the nerve divides into two distal branches within the inferior orbital fissure fat.
Greater Palatine	The point at which the nerve enters the greater palatine foramen.

3.2.4. Statistical Analysis:

The three independent observers rated the identification of the trigeminal nerve branches based on a 5-point system for all four scan types. A nerve branch was rated excellent (4) if both the proximal and distal portions of the nerve, relative to the intermediate point, were identified and continuous; good (3) if both the proximal and distal portions of the nerve were identified and at least one portion was continuous; fair (2) if only one of the proximal or distal portions of the nerve were identified and continuous; poor (1) if only one of the proximal or distal portions of the nerve was identified but not continuous; and none (0) if the nerve was not identified. Average ratings were calculated for each nerve category (table 1). Interobserver reliability was measured using weighted kappa analysis [87]. Kappa

values were found for pairs of observers and then averaged. The kappa analysis agreement scale was arranged as follows: ≤0.2 = poor; >0.2 to ≤0.4 = fair; >0.4 to ≤0.6 = moderate; >0.6 to ≤0.8 = good and >0.8 = excellent. All analyses were performed using the R statistical and computing software, Version 3.2.2 (http://www.rproject.org) and the irr package. A p value less than .05 was considered significant. In a small sample size such as our study, the kappa statistic formulation often overestimates probability of agreement due to chance and effectively results in a lower interobserver agreement [87]. Hence, we also calculated percentage agreement (Table 3) to provide a more comprehensive indication of nerve detection performance.

3.3. Results:

Anatomical observations for each trigeminal nerve projection and example images of nerve portions are reviewed first followed by a summary of the statistical findings.

3.3.1. Image quality analysis:

Visual inspection was performed to rule out the presence of ghosting, local blurring, and Gibbs artifacts on all the images. SNR and contrast to noise ratio (CNR) values were found with ROI placed on the optic nerve (Figure 3). In the case of MPRAGE, post-contrast SNRs were slightly higher than pre-contrast SNRs and a paired t-test analysis gave a p value of 0.016 implying statistical significance. In the case of CRANI, however, the p value found

from t-test analysis was 0.44, implying no significant difference between pre- and post-contrast SNR values. Paired t-test comparison of pre- and post-contrast CNR values did not show any statistical differences. SNR and CNR values were calculated to demonstrate the quality and reliability of the acquired data and did not provide any conclusive implications on the best sequence for nerve detection.

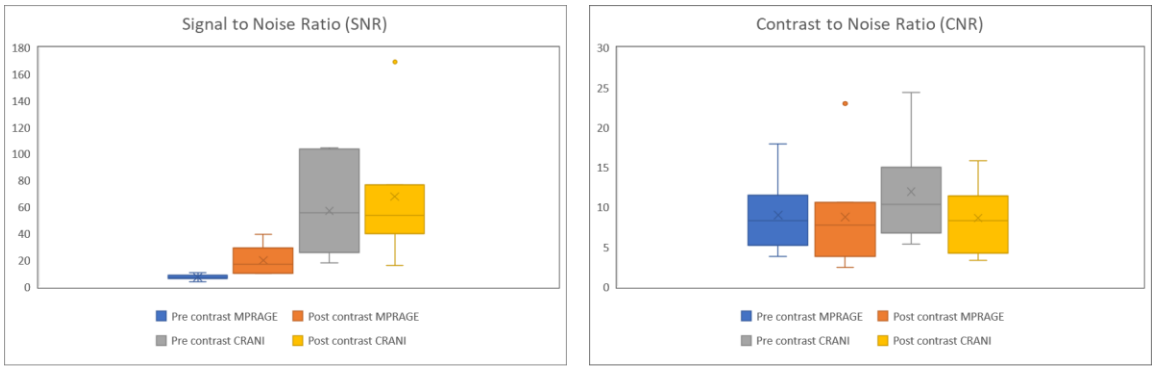

Figure 3 Comparison of SNR and CNR values in pre- and post-contrast MPRAGE and CRANI calculated by selecting ROI on the optic nerve.

3.3.2. CN V1:

Within Meckel's cave, ophthalmic n. V1 arises from the upper aspect of the gasserian ganglion and projects anteriorly through the lateral wall of the cavernous sinus below CN3 and CN4 and above V2. Just prior to passing into the orbit through the superior orbital fissure (SOF), V1 branches into the frontal, nasociliary, and lacrimal branches.

The frontal n. (Figure 4) is the largest of the three branches of V1 and is the most reproducible on imaging. As the three branches of V1 course through the SOF, the frontal n. takes a superior course and lies between the periosteum of the bony orbital roof and the muscle complex of the levator palpabrae superiororis and superior rectus muscles. The nasociliary n. is smaller than the frontal n. but larger than the lacrimal n. It also enters the orbit at the SOF and then courses medially towards the medial orbital wall crossing the optic n. as well as the ophthalmic artery, and superior ophthalmic vein. The nasociliary n. courses beneath the superior rectus and superior oblique muscles as it extends towards the anterior ethmoidal foramen. The lacrimal n. is the smallest subbranch among the three V1 branches and is therefore the least well seen by imaging. It extends from the SOF coursing laterally along the upper border of the lateral rectus muscle, ultimately terminating within the lacrimal gland.

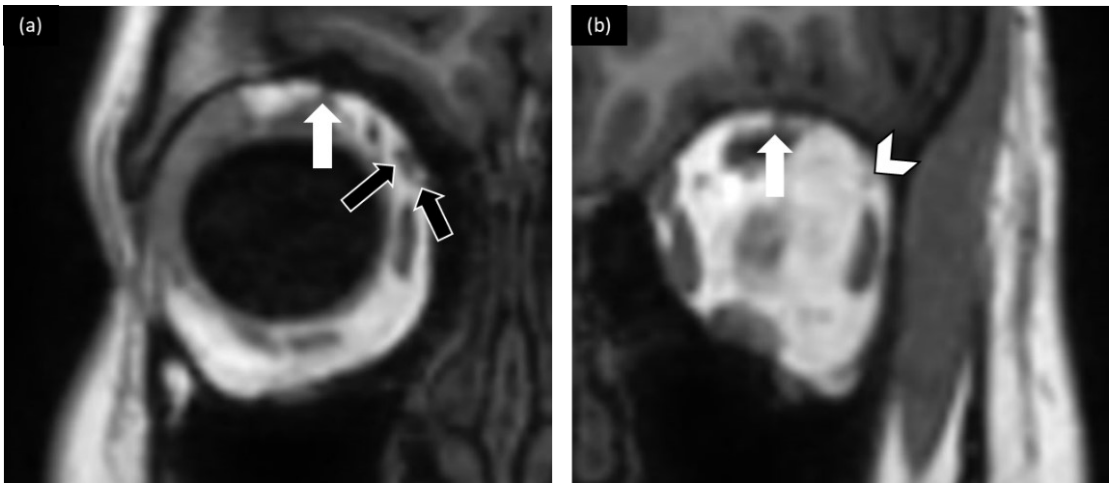

Figure 4 Coronal pre-contrast MPRAGE image sections representing branches of V1. The white arrows indicate the location of the frontal branch, black arrows indicate the nasociliary branch, and the white arrowhead indicates the lacrimal branch.

3.3.3. CN V2:

The maxillary nerve (V2) extends from the gasserian ganglion within Meckel's cave anteriorly into the lateral wall of the cavernous sinus, where it lies just inferior to V1. As the nerve exits the cavernous sinus it extends directly anterior through foramen rotundum, into the pterygopalatine fossa, and then into the inferior orbital fissure (IOF). There are numerous branches of V2 arising from the nerve intracranially, within the pterygopalatine fossa, within the IOF, and distally within the facial soft tissues. Not all subbranches are large enough to be consistently reproducible on imaging. The branches best visualized on imaging that were chosen for evaluation in our study include the infraorbital nerve, the greater palatine nerve, and the zygomatic nerve.

The infraorbital nerve is the largest of the distal V2 branches. Upon traversing the IOF within the inferior orbit, V2 extends into the inferior orbital foramen where it continues as the infraorbital nerve. The greater palatine nerve (GPN) separates from the remainder of V2 just after exiting the foramen rotundum where it enters the pterygopalatine fossa (PPF). From the PPF, the GPN extends into the greater palatine canal and exits at the greater palatine foramen, providing anatomic sites that allowed for localization of this nerve on imaging. The zygomatic nerve branches off V2 just after exiting the foramen rotundum. From there the zygomatic nerve courses through the PPF and anteriorly into the orbit via the IOF.

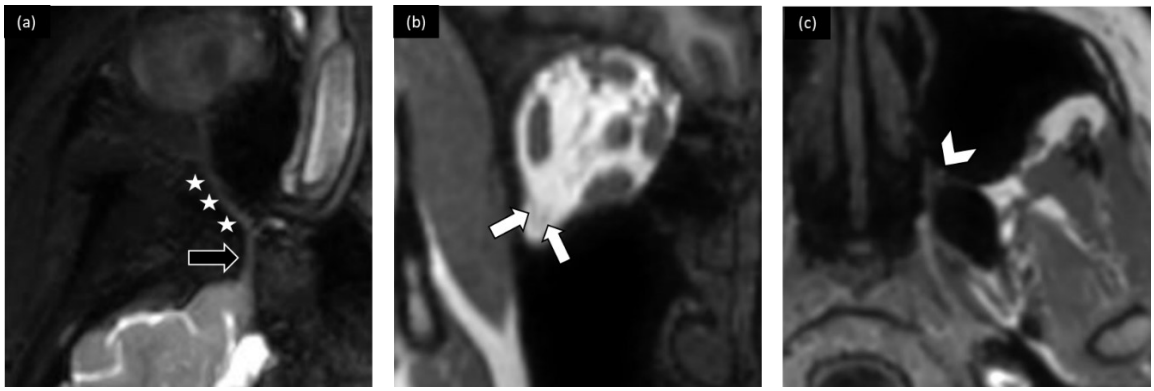

Figure 5 Pre-contrast CRANI (a) and Pre-contrast MPRAGE (b,c) images representing branches of V2. Part (a) shows an axial-MIP section illustrating the V2 nerve within foramen rotundum (black arrow) and its more distal continuation, the infraorbital nerve indicated by white stars. Part (b) shows a coronal section indicating the zygomatic branch (white arrows) just after dividing into the zygomaticotemporal and zygomaticofacial branches and (c) represents an axial section pointing to the greater palatine nerve (white arrowhead) leaving the PPF and just proximal to entering the greater palatine foramen.

3.3.4. CN V3:

The mandibular division (V3) is the largest division of the trigeminal nerve and is the only division containing motor fibers. Like V2, there are several distal branches of V3. However, only some of these are large enough to be reproducibly visualized on imaging. The branches which were evaluated in this study include the masseteric n., the buccal n., the auriculotemporal n., the inferior alveolar n., and the lingual n.

V3 extends from the gasserian ganglion within Meckel's cave inferiorly and slightly anteriorly to exit the skull base at foramen ovale. Immediately after exiting the skull base, V3 divides into anterior and posterior trunks. The anterior trunk gives off several branches including the masseteric and buccal nerves which divide in a V shaped fashion (Figure 6). These nerves may be observed in a single axial slice just beneath the skull base.

The auriculotemporal n. courses laterally from the posterior trunk of V3 just after exiting foramen ovale. The nerve has two roots which wrap around the middle meningeal artery (MMA) just before the vessel enters foramen spinosum. The two roots rejoin after wrapping around the MMA and continue further laterally, posterior to the lateral pterygoid muscle as well as the temporomandibular joint where it passes into the facial soft tissues adjacent to the superficial temporal artery (Figure 6).

The lingual nerve and the inferior alveolar nerve also arise from the posterior trunk of V3. Initially the lingual nerve and the inferior alveolar nerve course parallel to one another with the lingual nerve more medially located (Figure 7). The inferior alveolar nerve continues

laterally to enter the mandibular foramen. Prior to this point the lingual nerve takes a nearly 90 degrees turn to shift from an anterolateral projection to an anteromedial projection, a point at which these nerves can be well seen on imaging (Figure 7).

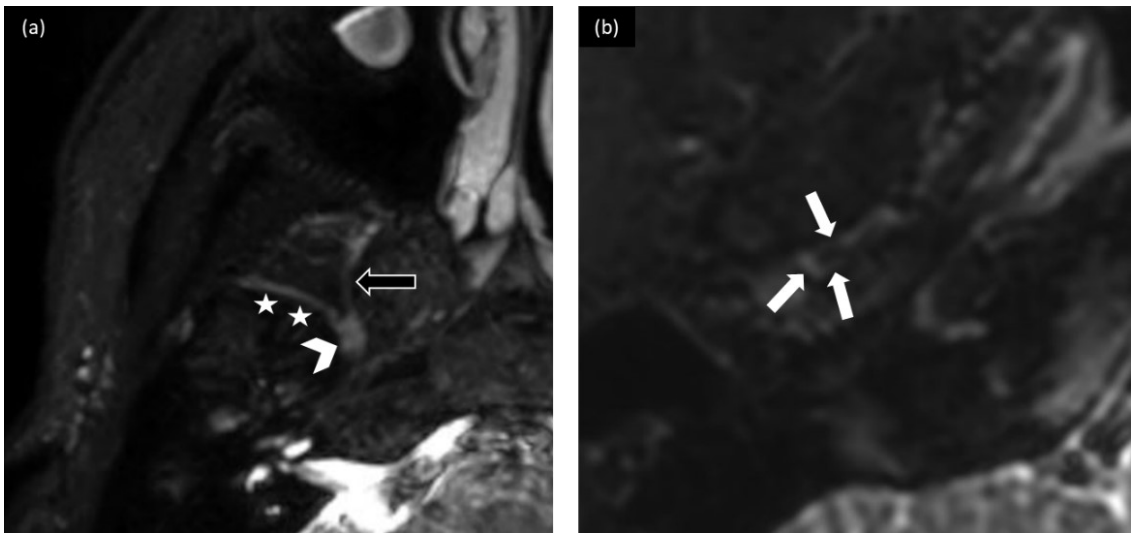

Figure 6 Pre-contrast CRANI images representing branches of V3. Part (a) shows an axial-MIP section indicating the V3 nerve (white arrowhead) and its further branching, the masseteric nerve (white stars) and the buccal nerve (black arrow). Part (b) shows an axial section indicating the auriculotemporal branch (white arrows).

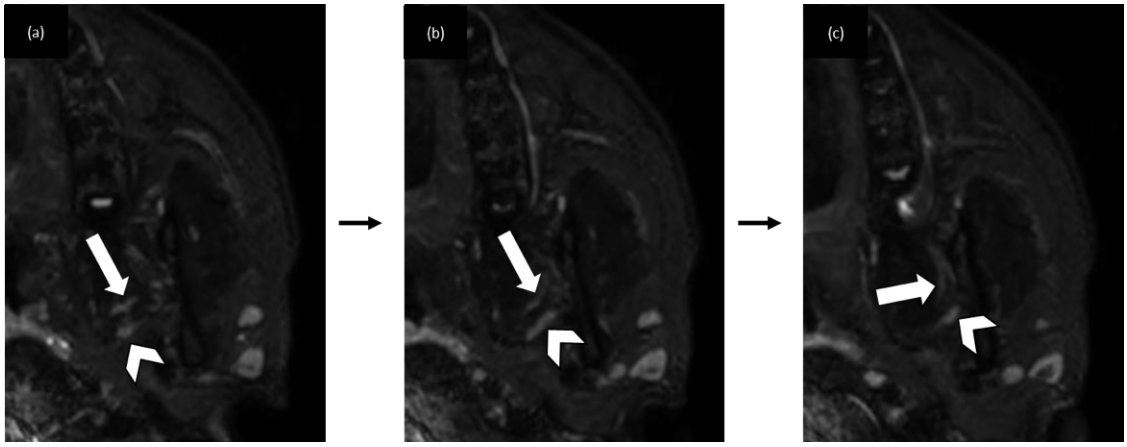

Figure 7 Pre-contrast CRANI images representing the lingual and the inferior alveolar nerves. Parts (a) through (c) represent consecutive axial slices showing how the lingual branch (white arrows) and the inferior alveolar branch (white arrowheads) travel roughly parallel to each other.

3.3.5. Kappa Analysis Results:

Pre-contrast MPRAGE outperformed CRANI for visualization of the branches of V1 and V2. However, the branches of V3 were better visualized on CRANI images, in part because these branches course in regions with more isointense muscle/soft tissue signal intensity. Three cases of kappa paradox errors were observed (denoted with *, table 3) where the kappa value was low (poor or fair agreement) even though the corresponding average observer rating (>3.5) and percentage agreement between observers was excellent (>80%). Table 3 identifies the best performing MR scan for every individual nerve branch. Bar plots including nerve detection metrics for each scan type are included in supplemental material (Figure 8).

Table 3 Nerve detection metrics for every branch and the corresponding imaging sequence which provided best identification.

Nerve branch		Best performing MR sequence	Observer ratings average	Kappa value average	Percentage agreement
Ophthalmic (V1)	Frontal	Pre contrast MPRAGE	3.9	1	100
	Lacrimal	Pre contrast MPRAGE	3.6	0.79	76.2
	Nasociliary	Pre contrast MPRAGE	3.5	0.37*	90.5
Maxillary (V2)	Infraorbital	Pre contrast MPRAGE	3.9	0.107*	80.9
	Zygomatic	Pre contrast MPRAGE	3.1	0.802	80.9
	Greater Palatine	Pre contrast MPRAGE	3.4	0.61	80.9
Mandibular (V3)	Masseteric	Post contrast CRANI	3.2	0.81	71.43
	Buccal	Pre contrast CRANI	1.4	0.75	59.53
	Auriculotemporal	Pre contrast CRANI	3.5	0.83	85.7
	Lingual	Pre contrast CRANI	3.9	0.69	85.7
	Inferior alveolar	Pre contrast CRANI, Post contrast CRANI	3.9	0.15*	85.7

*Parallax error where erroneously low kappa values were computed despite high interobserver agreement.

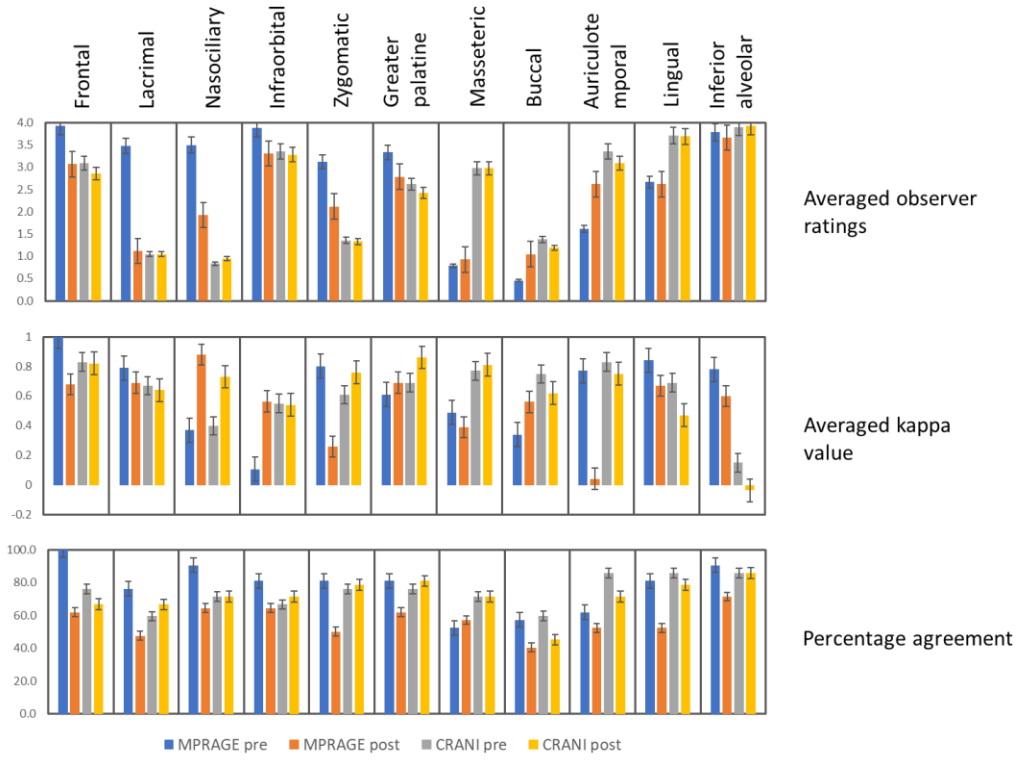

Figure 8 Clustered bar plots representing nerve identification metrics corresponding to every nerve branch.

3.4. Discussion:

A comprehensive study of the trigeminal nerve anatomy and its visualization using the novel CRANI sequence and the MPRAGE sequence with and without contrast enhancement was performed. Excellent visualization was found for all branches of ophthalmic nerve on pre-contrast MPRAGE images, with average observer rating > 3.5 and excellent interobserver agreement. In the case of the nasociliary branch, the computed kappa score was 0.37. However, we determined that this was a result of kappa parallax

error as the percentage agreement was 90%. We conclude that excellent visualization of the nasociliary branch was possible.

The branches of maxillary nerve were also identified on pre-contrast MPRAGE images with good to excellent observer identification ratings. Interobserver agreement was good to excellent. As in the nasociliary branch, paradoxically low kappa values were seen in infraorbital branch identification. Post-contrast MPRAGE images provided hyper-intense representation of neurovascular structures and presented conflict in nerve identification. These were therefore less useful for nerve identification.

The CRANI sequence can achieve nerve specific contrast enhancement due to the use of innovative MSDE pulse in combination with a PSS sweep within a short acquisition time [3], [14]. In our study, we found CRANI to provide better visualization in cases of the mandibular branches, most likely due to uniform fat and venous suppression near the mandibular nerve. Two mandibular branches frequently studied clinically, the inferior alveolar and the lingual nerve, may be injured during dental surgeries and may also be involved in mandibular carcinoma[80], [88]. The distal regions of both these nerves were well identified on the pre-contrast CRANI images with average observer ratings of 3.9. This is also consistent with the results obtained from CRANI studies conducted by Cruyssen et al. [14], [89] and Casselman et al. [3] Our results were also in agreement with the study performed by Fujii et al. [85] where they used MR imaging with the 3D double-echo steady-state with water excitation (DESS-WE) sequence retrospectively to identify of the extracranial branches of the mandibular nerve. We furthered their study by determining

anatomical markers useful for studying the continuity of ophthalmic and maxillary nerve branches and validated the visualization of mandibular branches with CRANI. In comparison the CRANI sequence provided better visualization in the case of the auriculotemporal branch, and this may be due to CRANI's ability to provide homogeneous fat suppression and fewer susceptibility effects. However, in contrast to other CN identification studies[89], [90], we did not observe improved visualization or improved interrater reliability scores in post-contrast MPRAGE or post-contrast CRANI imaging compared to pre-contrast imaging in our group of normal healthy adults. Although, it should be noted that post contrast imaging would be expected to aid in detection of these nerves in the pathologic state. For example, perineural spread is well assessed on MRN and post contrast imaging with fat suppression[78].

Identification of nerves posed challenges due to discontinuity or signal drop out at multi-tissue interfaces and confusion with blood vessels [7]. T2-weighted sequences have poor contrast between vessels and nerves, potentially leading to mischaracterization of nerve when there is little or no intervening CSF. In cases with potential conflict, nerve identification was cross-referenced to make sure segments of the nerve were observed at the same location on both MPRAGE and CRANI to rule out blood vessels. This challenge was observed in the case of masseteric and the buccal nerve. These branches both arise from the anterior trunk of V3. However, as they travel through muscle it is easier to identify the masseteric but not the buccal nerve. This was reflected in the lower average observer rating of 1.4 obtained for the buccal nerve compared to 3.2 for the masseteric nerve.

Improved nerve identification following contrast administration was observed only in the case of the masseteric nerve, whereas pre- and post-contrast CRANI results for the buccal nerve were similar.

Overall, a comprehensive method to identify the trigeminal nerve anatomy using the novel CRANI sequence in combination with the MPRAGE sequence has been presented. This study may aid in image-guided diagnostics and surgery planning and tractography studies. Similar landmark identification strategies can also be extended to the other cranial nerves.

The small sample size of the study also provided some limitations which may explain the cases of kappa parallax error observed. Interobserver reliability values may also have been affected by the different levels of experience of the three readers. However, our results imply robust reproducibility among clinical personnel of varying experience levels to identify nerves using methods described in our study. Larger studies are needed to investigate sequences best suitable to evaluate distal cranial nerve branches in the pathologic state to facilitate the clinical usage of newer MRN techniques such as CRANI.

3.4.1. Conclusion:

A large FOV nerve visualization exam inclusive of the anatomy of all trigeminal nerve distal branches can be obtained within an acquisition time of 20 minutes using pre-contrast CRANI and MPRAGE. Post-processing with MPR and MIP images improved nerve visualization. Further, nerve-specific ROI selection can shorten the scan time of the clinical

examination. We did not observe an added benefit to nerve identification following the administration of gadolinium contrast agent, although, this might be useful in cases with pathology.

CHAPTER 4

TRACTOGRAPHY OF DISTAL TRIGEMINAL NERVE BRANCHES.

The trigeminal nerve is the largest cranial nerve, and it transmits both sensory and motor information like pain, temperature, and touch from the face to higher order nuclei in the brain. Proper functioning of the trigeminal nerve can be disrupted due to multiple pathological conditions like trigeminal neuralgia (TN), neurovascular compression, traumatic brain injury, perineural spread, multiple sclerosis and focal dystonia [32], [76], [77]. Visualization of the location of cranial nerves can be useful for diagnosing pathologies, and for preoperative surgical planning and image-guided surgery [32].

Many T1 and T2 weighted sequences are widely used as structural scans to clinically to assist physicians with nerve examinations [7], [76]. Many newer advanced T2 weighted sequences provide excellent identification of cranial nerves and have been able to localize both cisternal brainstem region and distal extraforaminal regions [7], [10], [13], [76], [78]. However, another field of MRI, called diffusion MRI (dMRI) which maps displacement of water molecules in a subject can provides helpful information about tissue microstructure and orientation that structural images cannot provide [91]. Through a method called tractography, qualitative and quantitative metrics about microstructural changes in cases of pathology can be derived from dMRI data [92]. Hodaie et. al [12] and Chen et. al [93] have reported that fractional anisotropy (FA) values were significantly lower in affected

TN areas after surgery and re-occurrence of pain in later stages also correlated with reversal of FA values. Measures like nerve volume and axial diffusivity from DTI analysis also provided understanding of demyelination and pathogenesis [93]–[95].

Multiple studies have investigated tractography of the trigeminal nerve using various MR acquisition methods and tractography algorithms [9][13][8], [96]–[98]. However, most studies have focused on tractography of the root-entry zone and cisternal region of TN (located inside the brainstem) (Figure 10) which are mostly affected by conditions like trigeminal neuralgia due to vascular compression [32], [93], [99], [100]. Trigeminal neuralgia can also occur due other pathological conditions like lesions, multiple sclerosis, and injury due to trauma or surgical procedures [41], [77] which may affect the entire length and peripheral regions of the nerves. Peripheral divisions of branches of TN often get damaged during dental surgery or tumor therapies and pre-operative visualization of nerve tracts has also helped neurosurgeons and physicians avoid damage to surrounding nerves during procedures [8], [32]. Tractography of peripheral TN branches outside the brainstem region will help advance DTI based reference information for radiologists and neurosurgeons for diagnostics and surgery planning and need to be studied extensively.

The trigeminal nerve exits the root-entry-zone (REZ) (Figure 10) in the brainstem from the trigeminal nuclei and travels distally to enter the trigeminal ganglion after which it divides into three branches namely the ophthalmic, maxillary, and mandibular branches which further subdivide and innervate the face. Most DTI based studies have visualized portions of the trigeminal nerve in the cisternal portion of the brain before branching [5], [10], [13].

Some tractography studies have found 3D trajectory of the trigeminal nerve within the brainstem and in portions anterior to Meckel's cave in the brain [13][7]. Some studies successfully identified the spinal trigeminal tract and branching or branch-like structure [96]. To our knowledge, there are no DTI studies where tractography of the trigeminal nerve has been followed outside the brain region extending up to periphery.

Most tractography studies involve selection of a start point anatomical marker or seeding ROI identified on corresponding T1 or T2 weighted anatomical MR scans or identified from other imaging modalities like histology, and CT. For trigeminal nerve, most studies have used seeding ROIs in the cisternal region [7], [98]. Further adding extra tract guiding ROIs typically in the meckel's cave (MC) or trigeminal ganglion region (Figure 10) has been shown to reduce the occurrence of false positives and false negatives during tractography. Using multiple ROIs restricts fiber selection and aids in achieving continuous tracts across multiple multi-fiber tractography methods [7].

Successful DTI tractography of cranial nerves depends on multiple factors like DTI acquisition parameters, ROI selection, type of tracking algorithm, fractional anisotropy threshold, tracking step size, and tracking curvature threshold [7]. Multiple tracking algorithms exist in literature and can be broadly classified as deterministic or probabilistic [13], [101]. Considering limitations like curvature, bending or branching of nerves, probabilistic tractography has shown better results in tracking small fibers, white matter, and cranial nerves [97][102][101]. Amir Zolal et al. [97] found that High angular resolution DTI scans are preferable for the DTI-based depiction of the cranial nerves. Xie et al. [98]

found that tracking of branching structures of trigeminal nerve was best achieved with a two-tensor model and an acquisition using b = 1000 or b = 2000 s/mm². In general, b > 1000 s/mm² acquisitions provided the best-rated tracking results. Further research is needed to improve both sensitivity and specificity of the depiction of the TN anatomy using dMRI. Most studies use >50 DW directions and an optimal b-value of the range 2,000-3,000 s/mm2 [98]. One research group [98] found that a two-tensor tractography method for TN tracking was able to identify more TN structures that a one-tensor fiber model, although, other studies found that using a multi-fiber tensor model also generated more false positive TN fibers [86], [103]. Using multiple ROIs to guide tractography outcomes can lead to less false positives.

4.1. Aims

In this study, we have created a tractography pipeline which utilizes peripheral anatomical markers to guide tractography of the trigeminal nerve beyond the brainstem region. Branches of the ophthalmic, maxillary, and mandibular nerves exit the skull via the supraorbital, infraorbital, and mental foramina as the ophthalmic, respectively, into the face. Locations for supraorbital and infraorbital foramen easily found from CT and MPRAGE data were used as peripheral markers. Peripheral anatomical markers identified from advanced nerve specific MR sequence CRANI in the previous study were also investigated with the tractography pipeline. We analyzed DTI data from five healthy subjects to successfully map the trajectory of the frontal, nasociliary, infraorbital, and mandibular nerves in extraforaminal peripheral regions. For every nerve case, the mean

FA values and streamline connectivity were calculated. Tractography was performed on both hemispheres separately and contralateral similarity analysis was done.

4.2. Methods involved in creating tractography pipeline:

4.2.1. MR acquisitions:

The protocols for structural data acquisitions (MPRAGE and CRANI) are described in Table 2. In the same clinical study, diffusion data following the HARDI protocol [104] which uses Echo Planar Imaging (EPI) was also acquired for every subject. Data was collected at b-values of 100 s/mm^2 (6 directions) and 1000 s/mm^2 (64 directions) with 2 mm isotropic resolution and matrix size of 240 × 240 × 100 mm^3. Two 6-direction DWI data sets were gathered with reversed phase encode directions to remove effects of background eddy currents. A 3D human head and neck CT scan image was downloaded from an online repository (http://www.pcir.org).

4.2.2. Data pre-processing:

The diffusion data was processed using FMRIB Software Library (https://fsl.fmrib.ox.ac.uk/fsl) for every individual subject. The processing involved converting DICOM images to NIfTI format, linear registration of

structural data to DWI space and removal of magnetic inhomogeneity effects using the FSL's topup procedure. FSL's BEDPOSTx tool uses Bayesian estimation methods to determine fiber orientation in each voxel from the DWI data [105]. The brain mask typically provided to the BEDPOSTx algorithm in regular tractography pipelines is found from extracting the brain region, instead, we altered this step and used a mask covering the entire head region to facilitate estimation of diffusion parameters at all voxels to aid tractography outside the brain.

4.2.3. Selection of anatomical priors:

Tractography was performed for the left and right hemispheres independently. A seed mask and a waypoint guiding mask were placed on the starting point of the trigeminal nerve in the cisternal brainstem region and a peripheral location respectively for each branch being investigated (table 4). To evaluate the use of peripheral anatomical landmarks in aiding tractography of extraforaminal trigeminal nerve branches two separate strategies were used. Method 1 used a combination of MPRAGE and CT data and method 2 used a combination of MPRAGE and CRANI data for waypoint ROI identification. Tractography of the frontal and infraorbital nerves were investigated by both the methods and the nasociliary, mandibular nerves were found only using the second method.

4.2.3.1. Method 1: Combination of MPRAGE and CT

The supraorbital foramen and the infraorbital foramen were identified on 3D CT data and masks were placed (figure 8). These masks were further transformed onto DTI data by a series of registrations. The CT data was registered through non-linear inter-subject registration (FSL flirt) with MPRAGE which was further registered using intra-subject linear registration (FSL flair) with diffusion space.

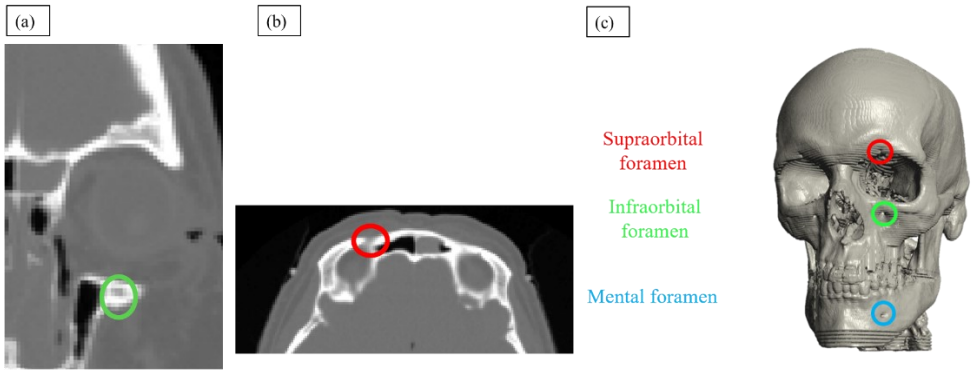

Figure 9 Axial (b) and coronal (a) slices of CT data showing supraorbital and infraorbital foramen. Figure (c) shows a 3D reconstruction image for better visualization.

4.2.3.2. Method 2: Combination of MPRAGE and CRANI:

The second method of locating waypoint ROIs involved using a novel T2 weighted sequence CRANI which provides nerve specific imaging [14]. This sequence helped visualize more extraforaminal anatomical landmarks allowing for the tractography of more nerve branches than method 1. The masks were transformed through intra-subject linear registration to DTI. As compared to method 1 this step

did not require multi-modality registration and hence had less chances of mask location error. Table 4 summarizes the waypoint ROIs used in method 2 and the corresponding branch of trigeminal nerve studied through tractography.

Table 4 Peripheral waypoint ROIs from MRAGE and CRANI used for tractography.

Nerve branch	Peripheral anatomical markers	MRI sequence best for locating waypoint markers
Frontal n.	Supraorbital foramen	MPRAGE
Infraorbital n.	Maxillary n. waypoint near foramen rotundum + Infraorbital foramen	MPRAGE + CRANI
Nasociliary n.	Anterior ethmoidal foramen	MPRAGE
Mandibular n.	Mandibular n. waypoint anterior to foramen ovale (before division of nerve into Buccal and Masseteric branches)	CRANI

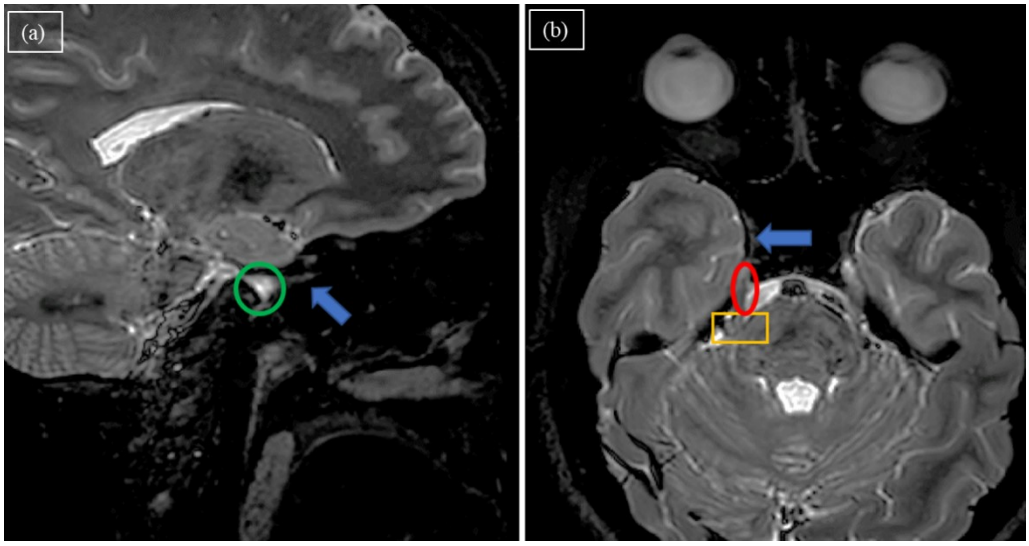

Figure 10 Trigeminal nerve ROI region detected on CRANI images. The yellow rectangle outlines the root entry zone (REZ) (b). Red circle indicates the cisternal portion (CP) (b). The blue arrows show the beginning of ophthalmic nerve projection (a,b). This region located just anterior to brainstem (green circle) represents the Meckel's cave (MC) region which houses the trigeminal ganglion (a).

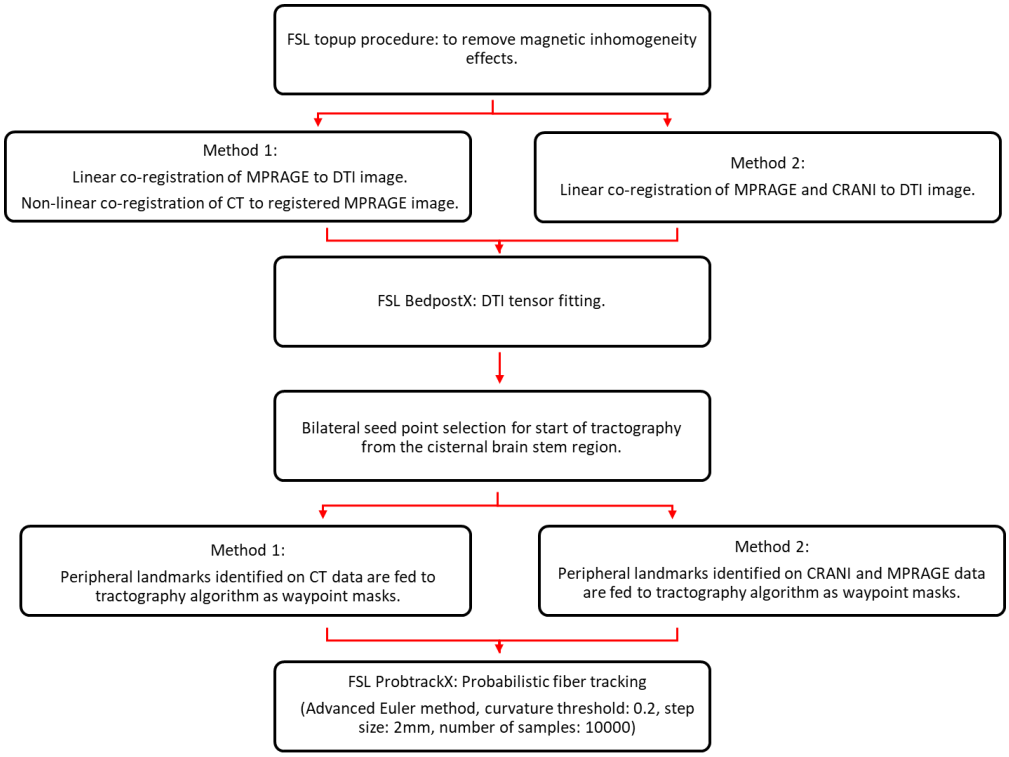

Figure 11 Tractography workflow for pipelines using anatomical markers from CT (method 1) and CRANI images (method 2).

4.2.4. Tractography

Probabilistic fiber tracking was performed using FSL's probtrackX function [105]. Each branch of the trigeminal nerve was tracked individually and bilaterally using the modified Euler algorithm [97], [105]. The number of samples was set at 10000, curvature threshold was 0.2 with loop check on and step size was set at 2 mm, to match the acquisition voxel resolution. The entire pipeline to successfully perform tractography is shown in (Figure 11).

4.2.5. Statistical analysis:

Connectivity measure quantifies the strength of connection between the seed and waypoint. To calculate connectivity for a tract, in FSL's probtrackX tool, the peripheral ROI was listed as both the waypoint mask and the termination mask and the waytotal count was recorded. This was then normalized by dividing the waytotal count by the number of voxels in the seed ROI to account for the differences in size of the seed and anatomy. The tractography streamlines were thresholded at 2 percent to eliminate spurious tracts.

Fractional anisotropy (FA) is a scalar value between zero and one that describes the degree of anisotropy of a diffusion process. A value of zero means that diffusion is isotropic, i.e., it is unrestricted in all directions. The tracts were overlaid with DTI FA maps and mean FA value was calculated for every individual nerve. Range of FA values observed in literature for trigeminal nerve are: 0.3159 ± 0.1159 [10].

4.2.5.1. Contralateral hemisphere comparisons:

Connectivity and FA values for the left-side tracts were recorded and compared to the values of right-side tracts using a non-parametric Wilcoxon signed rank test in the case of every subject. A p value of <0.05 was considered statistically significant. In a healthy adult subject, comparison between contralateral FA values should not be statistically significant, else it would imply a pathological condition along the nerve or error in ROI placements or tractography.

4.3. Tractography results

The following sections describes tractography results pictorially for every nerve case obtained using method 2, results from method 1 and finally lists statistical findings.

4.3.1. V1 branches - frontal nerve and nasociliary nerve:

Among the 5 subjects' data where method 2 tractography was performed, frontal nerve and nasociliary branches was successfully tracked in every case.

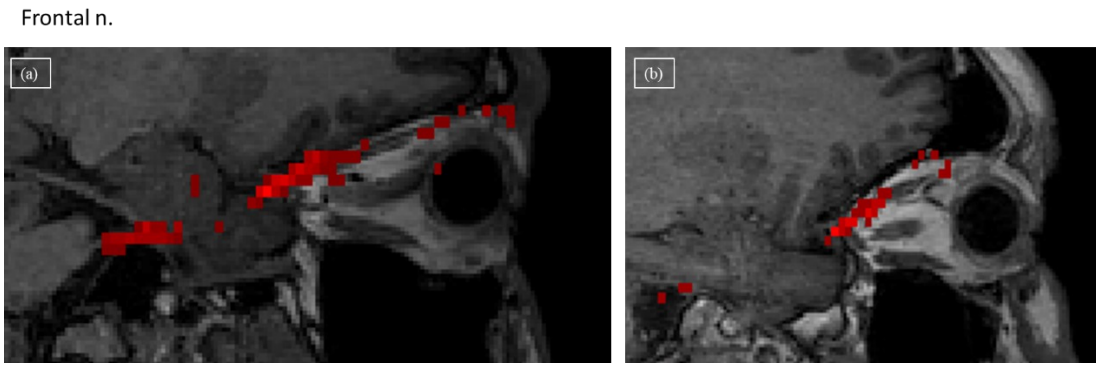

Figure 12 Frontal nerve projections on sagittal MPRAGE slices obtained using method 2.

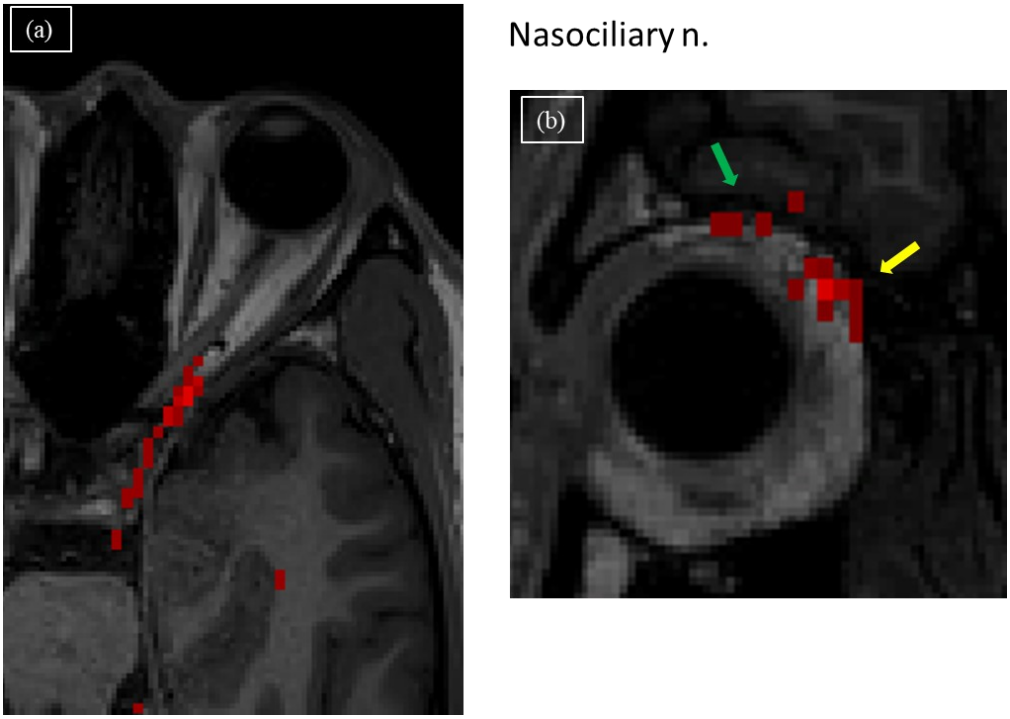

Figure 13 Nasociliary nerve branches depicted for two subjects on MPRAGE Image using method 2. The left figure (a) shows an axial view of tracked nasociliary branch. The figure on the right shows a coronal view. Tractography was able to identify both supraorbital foramen (green arrow) and anterior ethmoidal foramen (yellow arrow).

4.3.2. V2 branches – infraorbital nerve:

Using method 2, where the infraorbital foramen was directly identified on MPRAGE (table 4), produced better results for infraorbital n. tractography with branch detection in 4 subjects.

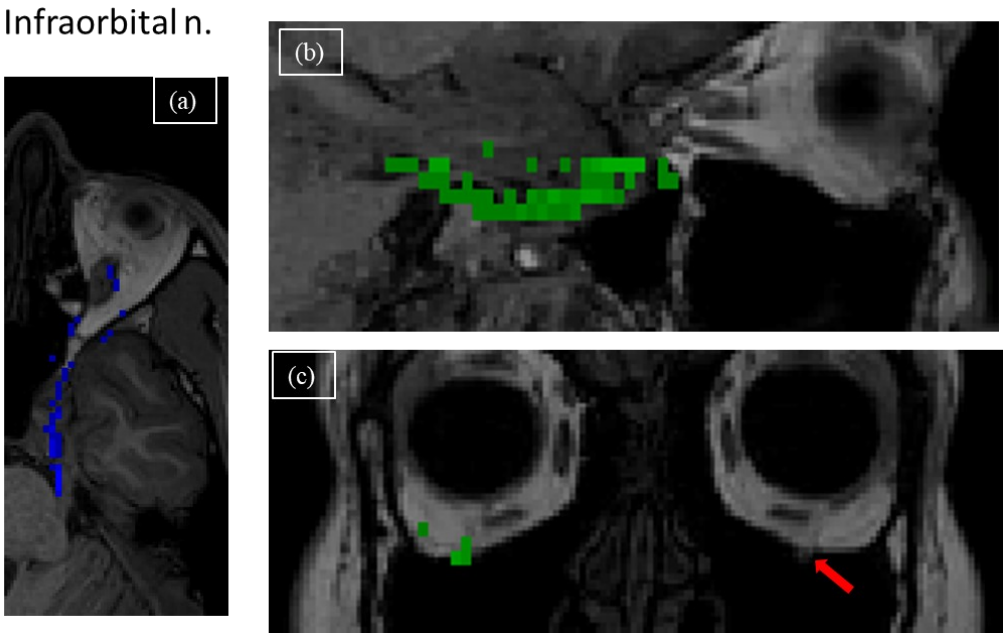

Figure 14 Infraorbital nerve tracts shown on MPRAGE Image using method 2. Three orientations of the tracked nerve infraorbital nerves are represented, axial (a), sagittal (b) and coronal (c). In the coronal image (c) the tract is overlaid only on one hemisphere and the infraorbital nerve (red arrow) can be seen in the other hemisphere to verify the tractography methods.

4.3.3. V3 branches – mandibular nerve:

The mandibular nerve was tracked using method 2 only as markers were detected on CRANI (table 4). The mandibular nerve was harder to track due to reasons like smaller FOV of diffusion images compared to structural image, partial volume effects, and edge artifacts on DTI. Attempts were made at tracking the nerve after it sub-divided into masseteric and buccal nerves by using extra waypoint markers, but only branch-like structures were detected (Figure 15).

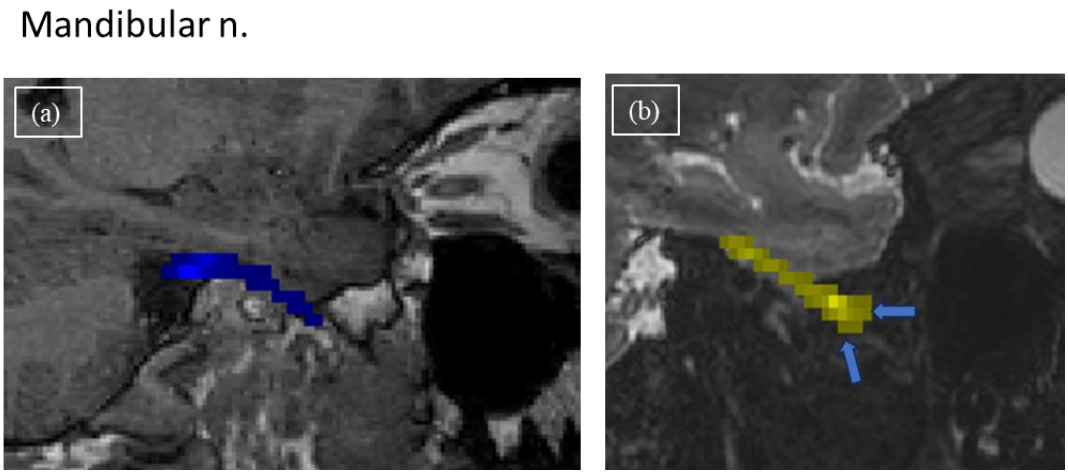

Figure 15 Mandibular nerve tracts shown on sagittal MPRAGE slices using method 2. The first figure (a) shows the mandibular division tract just after it originates from REZ and crosses trigeminal ganglion. The second figure (b) represents one case of mandibular tracts where branch like structures (blue arrows) indicating the branching of buccal and masseteric nerves could be seen.

4.3.4. Results from method 1:

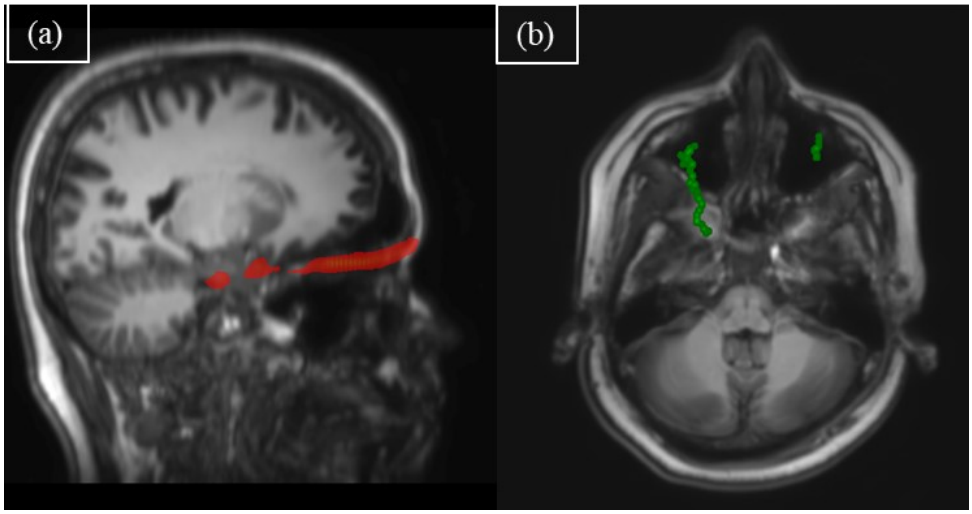

Figure 16 Frontal and infraorbital tracts from method 1.Projection of frontal n. (a) is shown on sagittal MPRAGE image and project of infraorbital tract is shown on an axial slice (b).

The frontal branch was tracked in all analyzed datasets using method 1, but the infraorbital was only detected on 2 subjects used. This is due to misalignment errors of CT-registered waypoint markers due to artifacts from multi subject deformable registration between CT and MPRAGE.

4.3.5. Statistical inferences:

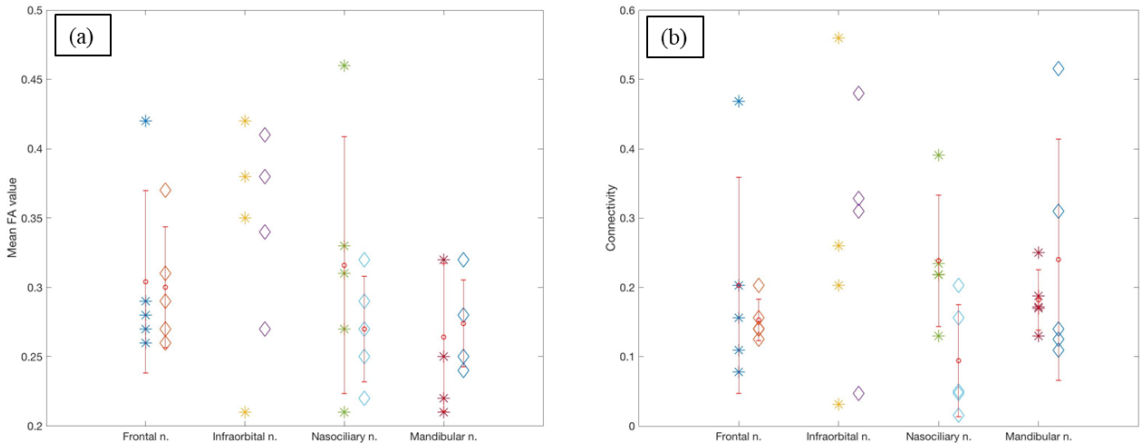

Figure 16: Scatter plots representing tractography metrics : mean FA (a) and connectivity values (b) found across all subjects for every individual nerve tracked.

4.3.5.1. Contralateral hemisphere comparisons:

Table 5 Intra subject statistical comparison between contralateral hemispheres.

	FA comparison: p value	Connectivity comparison: p value
Sub 1	0.69	0.91
Sub 2	0.23	0.86
Sub 3	0.3	1
Sub 4	0.48	0.79

Sub 5	0.34	0.057

From contralateral analysis all subjects had a p value > 0.05 implying no statistical significance. This means that the mean FA values and tract connectivity values were not statistically different for left and right hemispheres for every subject which is expected in a population of healthy adult subjects.

4.4. Discussion

In this study we performed DTI based tractography to non-invasively map the peripheral projections of the following trigeminal nerve branches: 1. Frontal nerve; 2. Nasociliary nerve; 3. Infraorbital nerve; and 4. Mandibular nerve. We incorporated the use of peripheral anatomical waypoint markers found using two methods into a probabilistic tractography pipeline. The first method localized markers only for the frontal and infraorbital nerve from a combination of MPRAGE and CT images. The second method used a combination of MPRAGE and advanced T2 weighted CRANI images to localize peripheral waypoint ROIs which were taken from a previous systematic nerve identification study presented in Chapter 3.

Using method 2 for tractography, we were able to track the trigeminal nerve in the cisternal brainstem region and even replicate the few studies [96][9] that were able

to delineate branch-like structures to indicate trigeminal nerve branching after the nerve exits the trigeminal ganglion. We were able to take this further and analyze systematically the delineation of the peripheral trigeminal nerve branches in their correct anatomic orientation through our tractography pipeline which incorporates peripheral ROIs. The projections for frontal and nasociliary nerves were successfully detected in every case. In some cases, detecting the masseteric and buccal nerve landmarks was harder and hence tractography could was performed using mandibular nerve landmark before branching. Tractography of the infraorbital nerve was seen to be more streamlined with the use of an intermediate landmark ROI on the maxillary nerve, implying that the use of multiple guiding ROIs helped reduce false positives. Tractography failed in only one case for infraorbital nerve using method 2, probably due to susceptibility artifact near infraorbital foramen.

For every nerve case we analyzed streamline connectivity strength and mean FA. Our main statistical findings were (1) Within individual subjects there were no statistical differences between tractography metrics from left and right hemispheres, which is expected of healthy adults without any neurological pathologies. (2) Comparing frontal and infraorbital nerves found using method 1 and 2 showed that method 2 had less streamline connectivity values while there was no statistical difference in mean FA values indicating that method 2 detected less false positives.

One limitation of this study is the small number of subjects, although the primary goal was to study the feasibility of incorporating peripheral landmarks in a probabilistic tractography pipeline. HARDI data which utilizes EPI technique is still prone to susceptibility artifacts at tissue-air interface [104]. Whole brain diffusion data being lower resolution is prone to partial volume effect particularly at cerebrospinal fluid (CSF) interface [100]. This study may be improved by using newer DTI sequences having very high resolution. Danyluk et al. [20] have used such a nerve specific high resolution DTI sequence for the identification of trigeminal nerves, although, such scans remain time intensive or require smaller FOVs. Other research studies [33] have aided the tractography of white matter tracts by informing tensor structure details using quantitative susceptibility maps. Vascular structures often present conflicts with anatomical identification of peripheral cranial nerve markers. This can be improved by subtracting venous projection from T2 MRI making it easier to define peripheral ROIs with greater accuracy [ref]. Other limitations include the use of probabilistic algorithms methods which are computationally intensive.

In this research we successfully created a refence atlas for peripheral trigeminal nerves in the diffusion space. In recent years, new tractography pipelines [5], [103] have been developed which can be used for a better tractography analysis along

with the current system of anatomical ROIs. Some applications of the pipeline developed in this research include:

- Use for detection of perineural spread – contralateral FA value comparison.
- Use for detection of demyelination – changes in FA value and inadequate trajectory detection.
- Creating and automating DTI atlas for trigeminal nerve.
- Personalization for neurosurgery – pre-planning for vascular conflict, trauma from dental surgery.

CHAPTER 5

HYBRID COMPUTATIONAL MODELS OF TRANSCRANIAL ELECTRICAL STIMULATION.

This chapter first explains the pipeline involved in creating a hybrid computational model and then describes stimulation studies with intracranial axon modelling. The purpose of these studies was to understand functionality of the NEURON environment, develop interpolation methods for extracellular potential and to establish precedent for use of tractography derived nerve location in a multi-scale model.

5.1. Motivation:

Biophysical nerve models can be built using software like NEURON (neuron.yale.edu) and GENESIS (genesis-sim.org) which predict the effects of stimulation using methods presented in the seminal work by McNeal [71] and Rattay [68]. These platforms assume quasi-static behavior and ignore the effects of ephaptic coupling. This chapter discusses the steps needed in setting up hybrid computational models which can be used to study trigeminal nerve stimulation.

The computational model pipeline was used to observe neural responses in an axon with straight geometry and an axon with imaging-derived realistic geometry to study the hypothesis that realistic geometries predict different neural excitability. An intracranial nerve found from tractography studies was used for this purpose. This model was also tested with pulsatile waveforms to check activation of

intracranial trigeminal nerve. Recently models are being integrated with advanced imaging techniques, such as diffusion tensor imaging (DTI) and functional MRI (fMRI). This integration allows for more accurate representation of axonal geometry and connectivity, enhancing the realism of computational simulations [106]–[108]. Most research studies that have used tractography based fiber information in a multi-scale neuron model have focused on studying cortical neurons and effects of transcranial magnetic stimulation (TMS) [106], [109], [110]. This is the first time a multi-scale model was built integrating cranial nerve location from tractography, an anatomically realistic head model and NEURON modelling.

5.2. Pipeline for constructing a computational model for TES simulation.

5.2.1. Segmentation of MR images and meshing

A structural MR image was segmented into different tissue types using SPM12 (Statistical Parametric Mapping) and Simpleware ScanIP (Synopsys Inc., Mountain View, USA) to construct a labeled high-resolution volume conductor head model with FOV 256 x 256 x 256 mm^3, using previously established in-house pipelines [111]. SPM is a popular software package used for the analysis of neuroimaging data, including automatically segmenting the five larger volume tissue types: skin, skull, CSF, gray matter, and white matter from MRI data using techniques such as tissue contrast, probabilistic segmentation, atlas-based segmentation, iterative optimization, and bias correction. The tissue masks

generated from SPM were imported into Simpleware to manually examine extent of each tissue type covered in the masks and correct for errors and to also add more labeled tissue segments for the following: muscles, fat, air, blood vessels, eyes, and ventricles. ScanIP was also used to define the electrode segments. The following electrode montage was used in the research listed in this chapter: one electrode at right supraorbital (RS) and the other on the right mastoid (RM) process. Tissue priority in the segmented head model was set as follows: white matter, gray matter, eyes, blood, air, CSF, fat, bone, muscle, skin, and electrodes to account for overlapping tissue boundaries before proceeding to meshing. The head volume was meshed into quadratic tetrahedral elements as per protocol determined to have optimal error free solutions in previous in-house research [26].

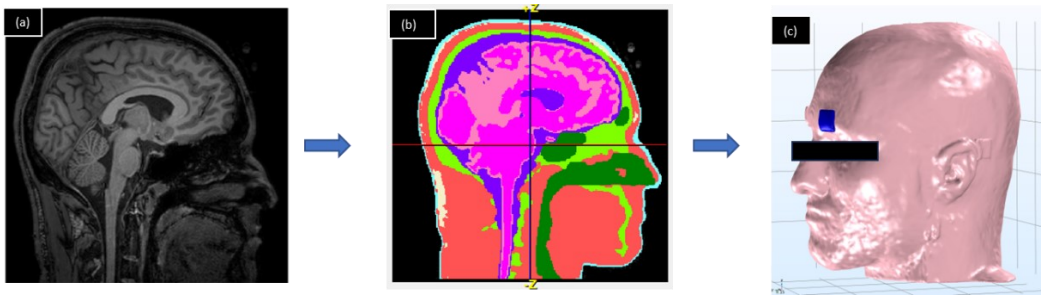

Figure 17 . Work-flow process involved in segmenting different tissue types in the head. T1-weighted MR image (a) was segmented into individual tissue components using SPM and Simpleware (b). A finite element (FE) mesh was generated from the segmented model and imported as solid volumes to COMSOL Multiphysics (c).

5.2.2. COMSOL modeling

The segmented labeled and meshed volume was then imported into COMSOL Multiphysics (Burlington, MA, USA), to model electric field and extracellular potential distributions. Individual tissue properties were assigned based on literature and are shown in table 6. For TES, 1 mA current injection was applied to one electrode (anode) and the other electrode was grounded (cathode). The COMSOL simulation calculated the electric potential distribution within the defined domain based on the Laplace equation. The boundary condition defined for electrostatic calculations were (1) inward current flow = Jn (normal current density) applied to the exposed surface of the electrode and (2) ground. This output volume represented the voltage distribution across various tissue due to TES (Figure 18).

Table 6 Assigned tissue conductivity values.

Tissue type	Electrical conductivity (S/m)	Reference
Electrode	0.6	[111]
Skin	0.43	[112]
Muscles	0.16	[113]
Fat	0.024	[114], [115]
Skull	0.01	[116]
CSF	1.79	[115]

Air	~0	-
Blood vessels	0.7	[117]
Eyes	0.5	[115]
Gray matter	0.33	[113]
White matter	0.15	[113]
Ventricles	1.79	[114], [115]

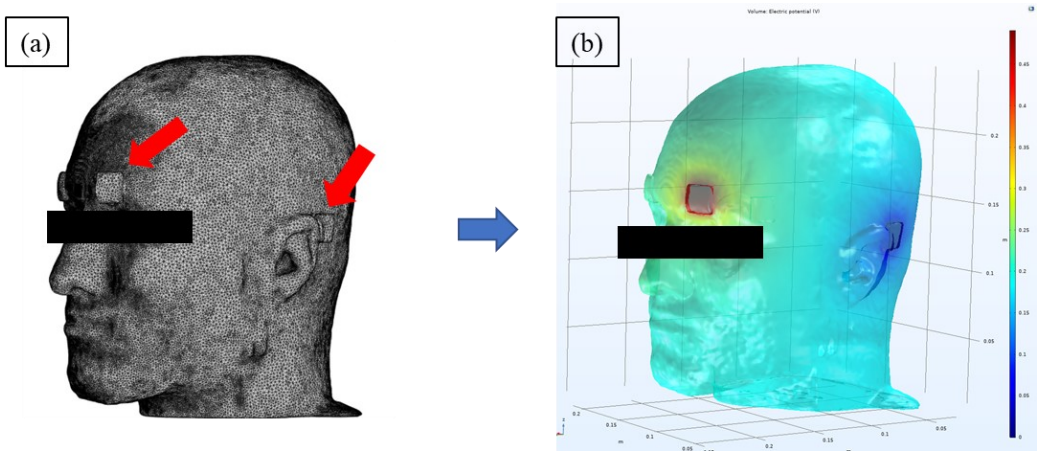

Figure 18 Simulation of TES using COMSOL Multiphysics.

The first picture (a) shows the placement of the two electrode RS-RM montage indicated by red arrows. The second picture (b) represents 3D volumetric potential values (in V) generated after TES simulation using 1mA input.

5.2.3. Building myelinated axons

The myelinated axon models were derived from two research works. The widely used MRG model which included complex membrane dynamics with explicit representations of the nodes of Ranvier, paranodal, and internodal sections of the axon (Figure 19), as well as a finite impedance myelin sheath [66], [108] and the Gaines model [118] that included extra physiological channels like the inclusion of a fast channel in the node to correctly represent sensory and motor functions. First, the Gaines model was downloaded and replicated with data found from ModelDB (accession number: 243841). Then parameters of the model like radius, total length of axon, stimulation waveform amplitude and duration were updated, and the potential input provided to the model was updated to the interpolated extracellular information derived from the current TES model. This exercise was done to verify that the shape of action potential (Figure 20) and strength-duration curve (Figure 28) from the new protocol matched the published data to validate the new updated model. The shape of space plots was also compared (Figure 21).

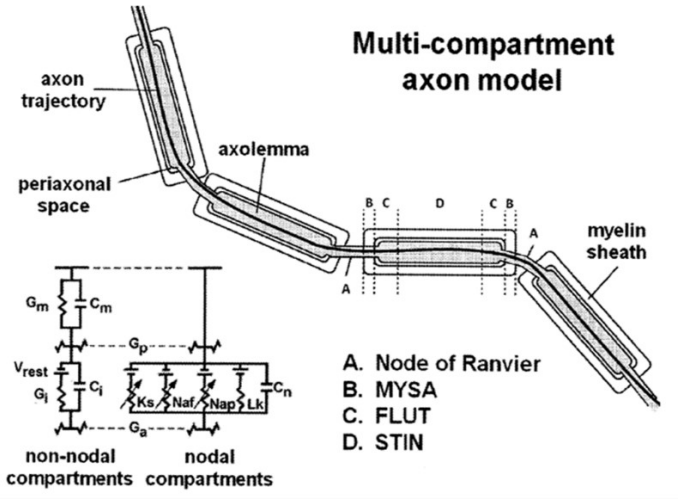

Figure 19 Structure of myelinated axon model designed by McIntyre, Richardson, and Grill [43], [54].

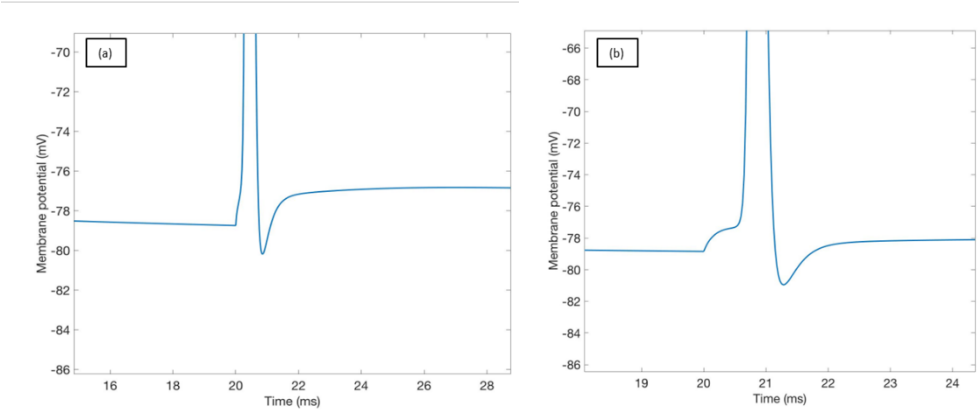

Figure 20 Action potential shape from replicated Gaines et al. [55] model (a) is similar to that found from updated model (b).

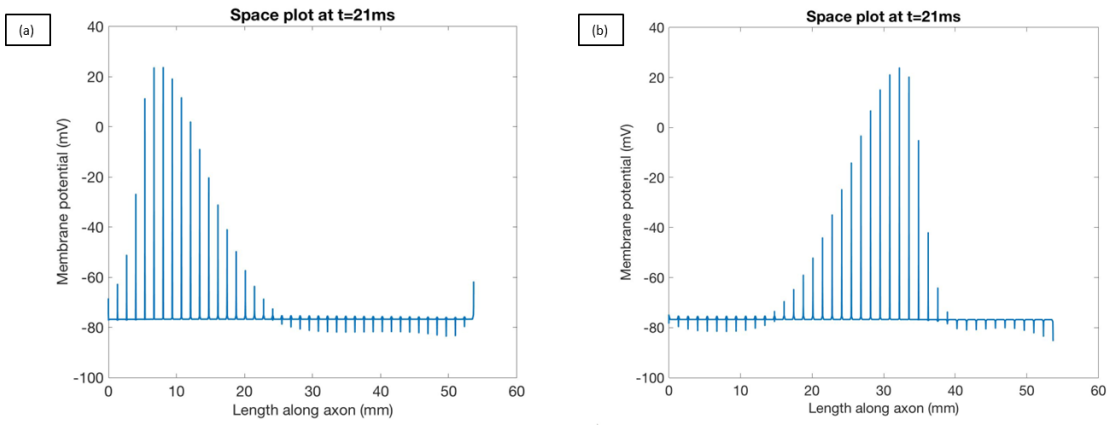

Figure 21 Comparison of space plots from replicated Gaines et al. [55] model (a) and updated model for validation (b).

Space plots for myelinated axons were represented as length along axon vs membrane potential. It should be noted that during the propagation of an action potential, higher values of membrane potential are only seen at locations representing NODE segments followed by slightly elevated values seen at MYSA segment locations, while the membrane potential values representing FLUT and STIN segments remain close to resting potential. This is observed because of the assigned physiological properties such higher channel conductivity values for NODEs and Fast Na+, Persistent Na+, Slow K+, and leakage currents responsible for nodal action potential as defined by MRG and Gaines et al. models. These space plots also align with the believed mechanism of myelinated axons, where action potentials travel by "jumping" to subsequent nodes of Ranvier and thus conduct faster than unmyelinated axons [119], [120].

5.2.4. Sampling extracellular potential

Extracellular voltage input for the NEURON model was found by mapping along axon geometry and corresponding the spatial coordinates found from MRI to volume distribution found from COMSOL. Lengths of internal components like STIN, FLUT, MYSA and NODE were assigned like those of a realistic sensory nerve following the specification used by the MRG model and Gaines et al. [66], [118]. These lengths depend on the fiber diameter and MRG originally provided collective values based on mammalian studies and Gaines et al. provided a curve fitting equation for further extrapolation.

Equation 13

$$Internodal\ length\ (\mu m) = 969.3 * \log(fiber\ diameter\ (\mu m)) - 1144.6$$

This implies that modeling two fibers of the same total length, but different diameters would have different number of nodes. An example of this variation is shown in table 7 where the number of nodes needed to represent a 60 mm length fiber is calculated. Spatial coordinates obtained from MRI nerve tract were in the mm range corresponding to the MR resolution. To match the spatial coordinates to the µm scale of internodal segments, the spatial points found from MR were further interpolated using spline techniques in MATLAB to obtain the closest fit curve that replicated the realistic axon geometry (Figure 22). The spatial points found from spline interpolation were sampled according to internal segment lengths depending on fiber diameter. Corresponding voltages from spatial coordinates sampled at the center of each segment were applied to the NEURON model.

Table 7 Variation in internodal length depending on fiber diameter.

Axon diameter (µm)	Internodal length from MRG model (µm)	No. of nodes needed to create a 60 mm length axon
5.7	500	112
8.7	1000	64
12.8	1350	46
16	1500	40

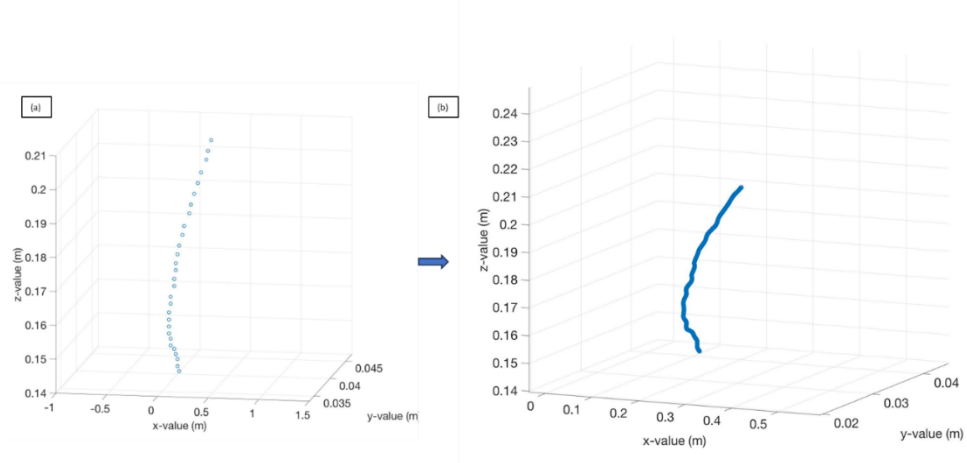

Figure 22 Spline interpolation technique used to sub sample extracellular voltage. 3-D coordinates corresponding to the location of the nerve fiber in axial slices are shown in (a). These points were further interpolated to find spatial locations matching internodal length resolutions (b).

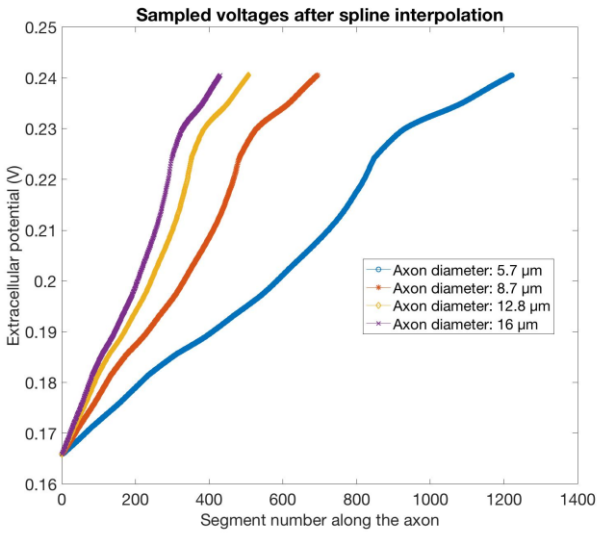

Figure 23 Sampling of extracellular potential depending on fiber diameter. The sole purpose of this figure is to demonstrate the differences in sampling of voltages seen by four fibers of the same total length located at the same position with respect to FEM but having different axon diameters and hence different number of nodes. The example here shows potential values for a peripheral supratrochlear trigeminal nerve branch.

In a fiber bundle consisting of different diameter axons, all the axons have the same total length while internodal segment lengths vary. Subsampled voltages are shown for four different diameter axons. The corresponding lengths and number of nodes are noted in table 7.

5.3. Studies with intracranial axons

5.3.1. Aims

Trigeminal nerve tractography studies provided continuous tracts with MRI-defined geometries and spatial locations in the intracranial regions for the frontal branch. As nerve fiber activation may depend on nerve orientation and trajectory relative to fields induced by transcranial electrical stimulation (TES) [106], [109], realistic axon geometries may provide more accurate spatial distribution of extracellular potentials as

compared to straight axon geometries typically used in most research models [109]. Stimulation amplitudes needed using a realistic axon trajectory may be different than a straight trajectory axon and hence may provide information on patient-specific personalization of TES sessions. The developed hybrid computational model setup was used to study and compare TES responses for two models: a realistic trigeminal nerve axon which was derived from DTI-based tractography and a straight axon model in the intracranial region.

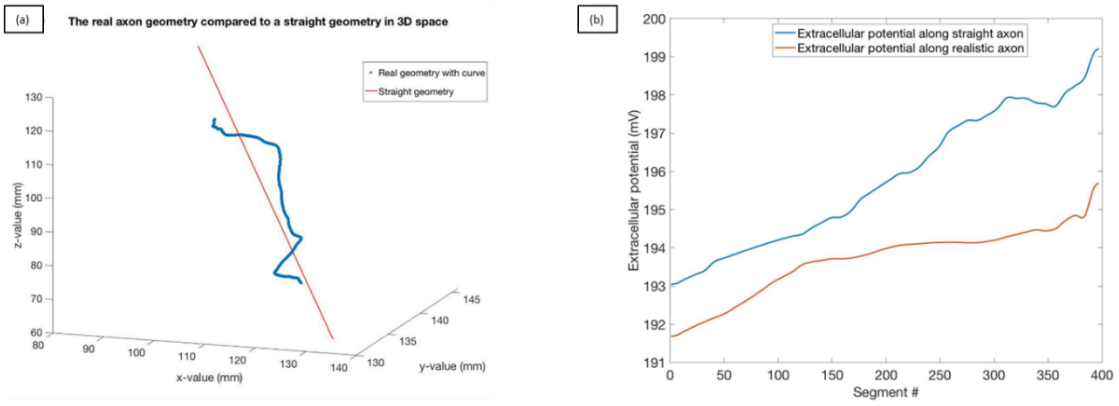

Figure 24 Setting up models for comparison of axons with straight vs. realistic geometries. Part (a) shows 3D shape of a straight axon vs. a DTI-derived realistic axon with tortuosity. Corresponding extracellular voltages are shown on the right (b). Although differences in absolute values can be seen in the two potential distributions, this may not cause a huge difference in neural response and needs further confirming from neural activation data.

5.3.2. Stimulation waveforms and neuron modelling:

Neural activation patterns were studied for pulsatile monopolar and bipolar waveforms of varying amplitudes (Figure 25). Following quasi-static assumption, the extracellular medium is purely resistive and hence a time-dependent waveform can be multiplied to the corresponding extracellular potential value at each node. The cable equation was solved in the NEURON environment [121] using backward Euler numerical methods with a time step of 0.01 ms for each condition to obtain transmembrane potentials. The straight axon geometry had the same number of total segments and length as the curved geometry but different coordinate locations in 3D space i.e., they had the same diameter.

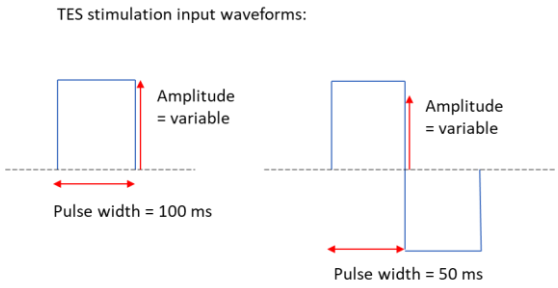

Figure 25 Shape of input waveforms used for stimulation.

5.3.3. Results from intracranial axon modelling

5.3.3.1. Comparing excitability of straight and realistic axons

The realistic axon model predicted different neural activation characteristics as compared to the straight axon model such as localized differences in the shapes of sub-threshold membrane potentials (Figure 26) and space plots (Figure 27). Nodes were either depolarized or hyperpolarized depending on the value of the double differential of voltage with respect to space.

These findings confirmed localized differences between simulations using realistic axon geometry and linear axon geometry, but the values were not different on the strength-duration plots for both (Figure 28). In case of space plots also (Figure 27), the differences observed between realistic and straight geometry were only seen for a short time right after the start of stimulation after which it evened out. This may be due to the smaller gradient of electric field distribution, as in this case (intracranial axon) the stimulating electrode is farther from the nerve, which does not cause huge differences between variation in voltage distribution seen by linear and non-linear geometries. Based solely on this experiment, using realistic geometry does not provide any added benefits.

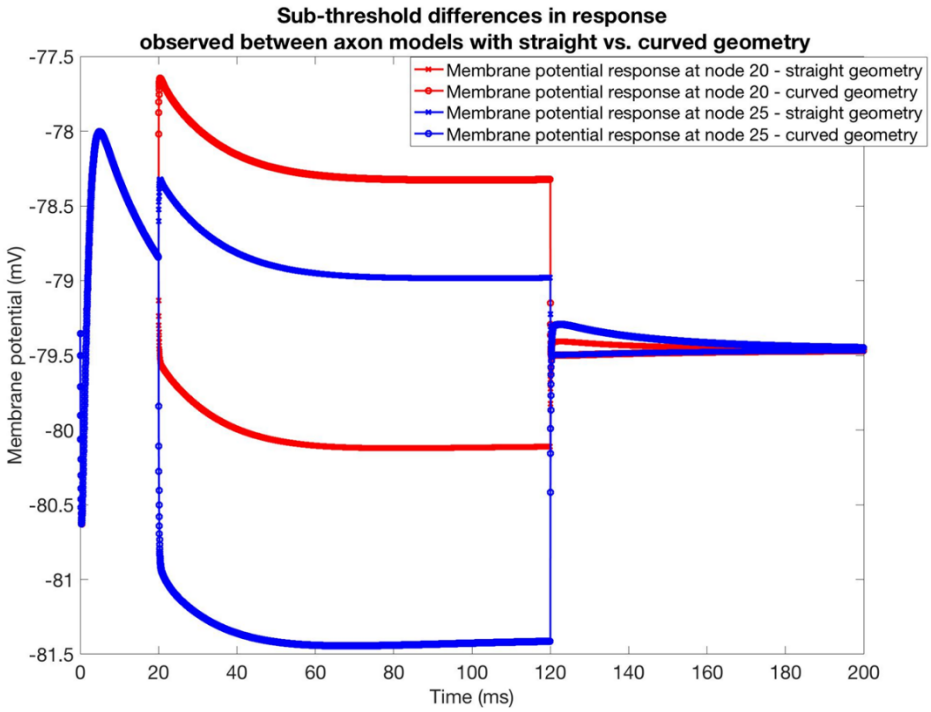

Figure 26 Sub-threshold membrane potential responses in axons with linear vs non-linear geometries. Localized differences are observed in the sub-threshold level for example in case of straight geometry axon, node 20 (red x) is depolarized, whereas node 20 (red dot) for realistic geometry axon is hyperpolarized. Similar localized differences were also observed at node 25, implying differences in extracellular potential seen from FEM by the straight vs the realistic geometry.

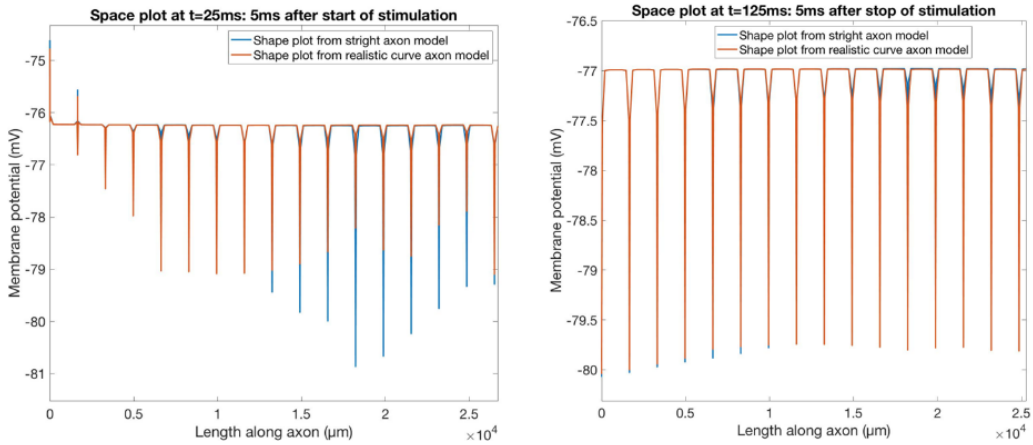

Figure 27 Space plots representing membrane potentials seen along the length of axons. Localized differences can be seen just after the start of stimulation (a) but with time the differences were not observed any more (b).

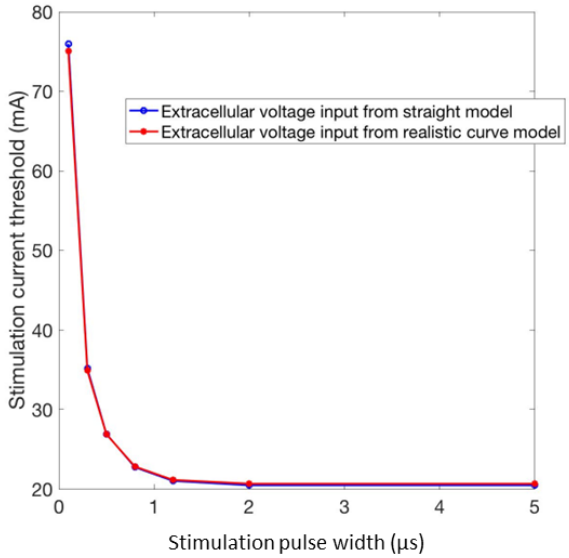

Figure 28 Comparison of strength-duration curves for axons with realistic vs. linear geometries. No difference in activation threshold values were observed.

5.3.3.2. TES of intracranial trigeminal nerve

Pulsatile monopolar and bipolar waveforms were multiplied with the extracellular voltage and applied after a delay of 50 ms. The amplitude of the input waveform was increased till action potentials were observed. An action potential (AP) was defined as a spike in membrane potentials with the peak value being greater than 0 mV. The stimulation threshold needed to see APs was observed to be 20.6 mA at 100 ms pulse width. This value is well over the established safety limit of 4 mA for TES [122] and implies that extracellular potential distributions caused due to TES in intracranial regions cannot activate cranial nerves. At the sub-threshold level, upon increasing stimulation amplitudes, level of depolarization or hyperpolarization increased (Figure

29, Figure 30). This may support the proposed tDCS mechanisms that suggest tDCS works through neuroplasticity over a long period of time, by bringing the membrane potential closer to AP thresholds [123], [124].

Figure 29 : Response to TES in an intracranial axon. Membrane potentials are shown for node 20 in response to monopolar stimulation.

At sub-threshold levels (<22 mA), node 20 was depolarized at the start of stimulation and remained depolarized till stimulation was on. The level of depolarization also increased with increasing stimulation amplitude until an AP was observed (22 mA).

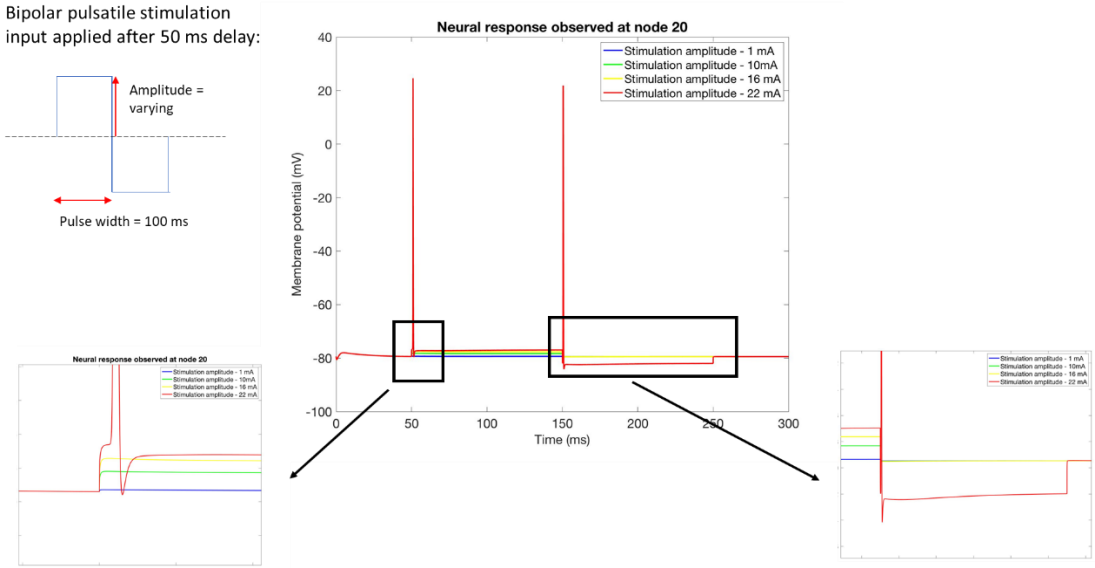

Figure 30 Response to TES in an intracranial axon. Membrane potentials are shown for node 20 in response to bipolar stimulation. Node 20 was depolarized after stimulation started and at sub-threshold stimulation levels, remained depolarized. When the polarity of the stimulation waveform switched, the node was brought back to resting potential.

5.4. Conclusion and discussion

Steps needed in building a realistic computational model with anatomically accurate volume head model combined with biophysical neuron modelling were successfully established. This protocol was used in all subsequent neuron modelling studies.

Recently there has been increased interest in incorporating imaging based information into neural computational pipeline in order to account for variabilities in human anatomy from person to person [15], [106]. To this effect, a study was designed to observe excitability differences between DTI-derived nerve fiber and a fiber with straight geometry. Although we observed some differences in parameters like value of sub-threshold membrane potential, localized differences in space plots, and AP peak values, a clear trend of changes could not be established. This model used far-field stimulation where the differences in relative change in extracellular potential experienced by the realistic vs straight geometry were not big enough to induce adequate neural excitability differences. But, in cases of near field stimulation, i.e., where the neuron in close to stimulating electrode such as in case of intraneural stimulation or peripheral nerve stimulations, realistic vs straight geometry axons could experience different extracellular voltage inputs making the need to use realistic geometries imperative.

Further, a tractography-derived neuron model representing intracranial trigeminal nerve was also used to study responses to TES. This exercise was done to check for any possible activation of intracranial nerves and study neural behavior at the sub-threshold level. Within the safety level of 4mA stimulation, AP was not observed for both monopolar and bipolar waveforms. This implied that if cranial nerves are activated during TES, the APs

start in the peripheral regions where the nerves experience greater electric field gradients. The excitability of peripheral nerves is studied in the next chapter. Subthreshold activity or oscillations play important roles in several aspects of neural function and information processing. In some neurons, subthreshold depolarization can bring the membrane potential closer to the firing threshold, making the neuron more responsive to small changes in input [29], [125]. Subthreshold activity in recurrent neural networks, such as in the prefrontal cortex, is thought to be essential for working memory. In some neuron types, dendritic branches play a significant role in processing subthreshold inputs. Dendrites can integrate signals from multiple synaptic inputs and generate local subthreshold potentials that contribute to the neuron's overall output [125], [126].

An intracranial nerve portion was used in this study as the tractography pipeline was able to provide continuous tracks only for the intracranial regions where there was no MR signal drop, artifacts, and partial volume effect. Although the landmark based tractography pipeline did not produce sufficient continuous peripheral subbranches of the trigeminal nerve, in future this landmark based pipeline can be improved by using better resolution diffusion images, focal ROIs targeting desired nerves, improved nerve specific diffusion sequences and advanced T2 weighted sequence [5], [100]. These methods may lead to peripheral nerves obtained through tractography which can then be integrated into computational neural models to make them more realistic.

CHAPTER 6

TRANSCRANIAL ELECTRICAL STIMULATION (TES) OF PERIPHERAL TRIGEMINAL NERVES – A COMPUTATIONAL STUDY

Transcranial electrical stimulation (TES) is a non-invasive technique that involves the application of electrical currents to the scalp, with the aim of modulating neural activity [123]. TES encompasses several techniques, such as transcranial direct current stimulation (tDCS), transcranial alternating current stimulation (tACS), transcranial magnetic stimulation (TMS), and peripheral nerve stimulation (PNS), among others [15], [123], [127]. The use of TES is being studied for various purposes such as cognitive enhancement and treating certain neurological disorders like epilepsy, major depressive disorder, migraine, Parkinson's disease, Schizophrenia, ADHD and more [15], [23]. The effectiveness and clinical utility of these techniques can vary, and they are often considered as adjunctive therapy in a broader treatment plan and in many cases are limited to research settings [123], [128].

The mechanisms behind TES are complex and can vary depending on the type of stimulation, the parameters of stimulation (intensity, frequency, duration), and the targeted brain regions. While tDCS and tACS are thought to work primarily by modulating cortical brain activity [123], it's possible that electrical currents applied to the scalp could also activate peripheral nerves to some extent [31]. Nerves such as the trigeminal nerve and the

vagus nerve have peripheral projections that could influence cognitive functions through their unique pathways. Asamoah et al. [129] found that application of a 1mA TES caused high electric field strengths (>20 V/m) in extracranial tissue enough to cause peripheral nerve activation. Additionally, several realistic head simulation studies [27], [28], [130] have found that the skull poses huge electrical impedance to the path of current flow and cortical brain structures receive only a fraction of the externally applied current, not enough to cause cortical neuron activation. Boekholdt et al [30], recently published a paper urging the need for more investigations into peripheral pathways, challenging the traditional understanding of TES which focuses solely on the modulation of cortical neurons through weak, subthreshold electric fields. Peripheral trigeminal nerves are important as their afferents innervate multiple regions of the head and project to higher order nuclei like the locus coeruleus (LC) through the trigeminal ganglion [75]. Activation of peripheral trigeminal nerves may activate the LC and lead to subsequent release of norepinephrine and dopamine which play a significant role in modulating various aspects of brain function. Overall, the LC-norepinephrine network has a widespread impact on cognitive functions, cortical excitability, synaptic plasticity, attention, and arousal making it a crucial component to be considered in understanding TES mechanisms [30].

Hence, targeted stimulation of trigeminal nerve has recently gained a lot of popularity and multiple clinical studies are being conducted to gauge the usefulness of trigeminal nerve stimulation (TNS) for conditions such as trigeminal neuralgia, migraine, and chronic pain

[19], [21], [131]. Most such TNS experiments consist of sessions that last multiple minutes and are typically repeated over days. During each session and between sessions separated by days, variations such as change in nerve location and electrode drift are possible. Response of nerves to stimulation can be affected by multiple factors like nerve location and shape, electrode shape and location, stimulation waveform and duration, which need optimization to further the usage of TNS for therapy. Ramaraju et al. [132] examined changes in current flow distribution in head models and found that electrode displacement affects the stability of stimulation experiments targeting cortical brain regions. A migraine therapy study by Salkim et al. [133] found that the value of stimulation current needed for the same amount of neural excitation varied significantly due to variations in neuroanatomical features and electrode orientation. Thomas et al. [123] have further studied the effect of different electrode shapes on TNS treatment of migraine and found that the clinically approved electrode shape did not comparably target the left and right peripheral sub-branches of the frontal nerve. These findings highlight the need for more computational modeling to understand variables in experimental stimulation design and to guide optimization for patient specific therapies.

6.1. Aims

In this study we used our hybrid computational systems to understand activation of peripheral trigeminal nerve models using common TES/TNS electrode montages and waveforms. The goals of this study were threefold. The first aim was to map the extent of

neural activation across the face using a standard tDCS electrode setting (F3-F4) and a pulsatile waveform. This helped understand if TES protocols activate the several branches of peripheral trigeminal nerves and may play a role in contributing towards TES mechanisms.

The second goal was to investigate if displacements in electrode location have effects on axon recruitment in case of TNS. This provided insights into levels of excitation efficacy achieved through TNS and potential for further optimization and personalization of TNS through imaging based selective electrode placement.

The third goal was to include unmyelinated axons in hybrid computational models. Unmyelinated axons in all the branches of trigeminal nerve are sensory afferents and transmit information like pain, touch, and temperature [39]. Activating unmyelinated axons may cause a sensation of pain and hence needs to be minimized during TES. We found appropriate stimulation amplitudes using modeling which minimized activation of unmyelinated axons while maximizing activation of myelinated axons.

6.2. Methods

Discussed below are the methods involved in creating a simulation model of peripheral nerve TES.

6.2.1. Imaging data

A high-resolution 3D T1-weighted structural image acquired in a 3T MRI scanner (Philips Ingenia System, Barrow Neurological Institute, Phoenix, USA) with a 240 (FH) x 240 (AP) x 200 (RL) mm^3 field-of-view (FOV) and 1 mm^3 isotropic resolution was used for head model segmentation. All procedures were performed with approval from the Arizona State University Institutional Review Board.

6.2.2. Configuration of peripheral nerves and electrode positions.

To map the excitability of the trigeminal nerve across the face, seven nerve branches were selected and drawn at different levels (Figure 31). The ophthalmic nerve branch of the trigeminal nerve exits the supraorbital foramen and branches into the peripheral supraorbital nerve (SON), the supratrochlear nerve (STN), and the infratrochlear nerve (ITN). The infraorbital nerve (ION) exits the infraorbital foramen and further branches out. The auriculotemporal nerve (ATN) and the buccal nerve are tributaries of the mandibular nerve. The zygomaticotemporal nerve (ZTN), subbranch of the maxillary division of the trigeminal nerve, exits through the zygomaticotemporal foramen. Similar to methods used by Thomas et al. [134] these selected peripheral trigeminal nerve branches were manually traced using available anatomical information from MPRAGE, CRANI, and anatomical literature references [39], [40], [75], [76]. The location of some of these branches (SON, STN and ION) was informed by MR images where the respective foramen could be visualized, using anatomical markers as described in chapter 3. Fibers drawn manually had tortuous geometry.

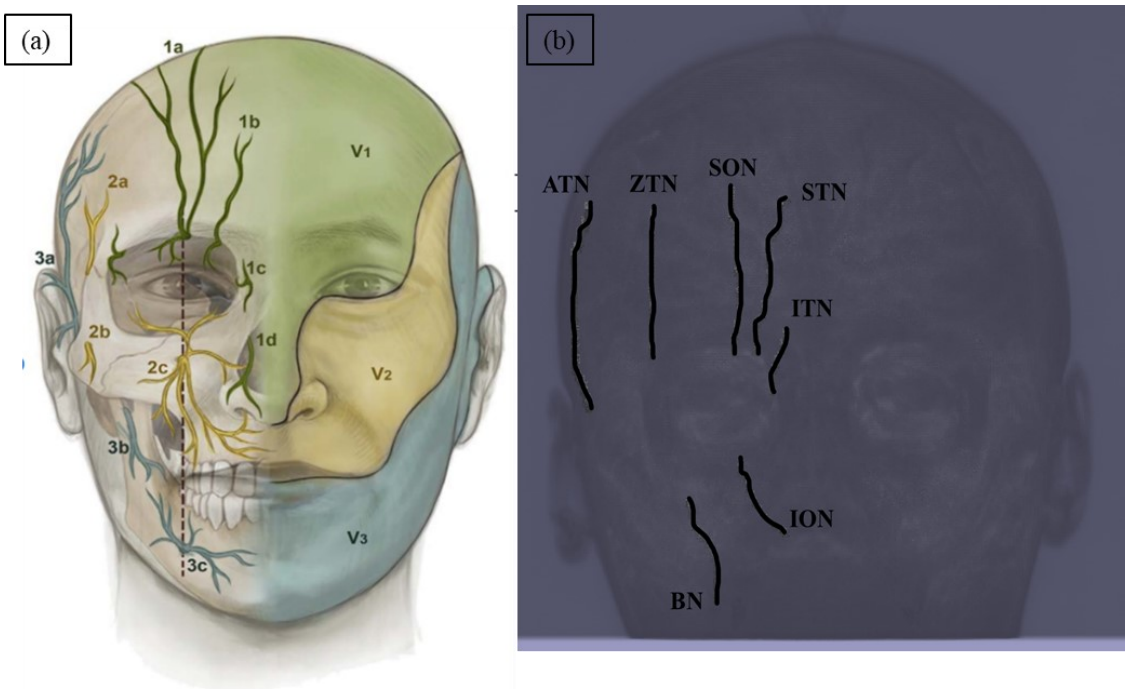

Figure 31 Anatomy of the trigeminal nerve and selected branches. Part (a) show a representation of peripheral tributaries of the trigeminal nerve adapted from research by Marur et al. [38]. The coloring divisions on the right side of the face show approximate areas innervated by the three main branches of the trigeminal nerve. Part (b) shows the seven nerves chosen for mapping TES excitability across the face. Projections of 3D nerve models have been overlapped on the human head volume model for visualization.

For TNS simulations, the electrodes were placed approximately over the supraorbital foramen (RS-LS also called Fp1-Fp2) location on both sides of the forehead (Figure 32) following the 10/20 electrode placement method.

6.2.3. FEM simulation

A labeled volume model with FOV 256 x 256 x 256 mm3, was created using methods outlined in chapter 3. The segmented labeled volume was then meshed and imported into COMSOL Multiphysics (Burlington, MA, USA), and was solved using the Laplace

equation with a current density boundary condition applied such that a total of 1 mA current injection was applied to the F3 or RS electrodes, and the other electrode grounded in each case.

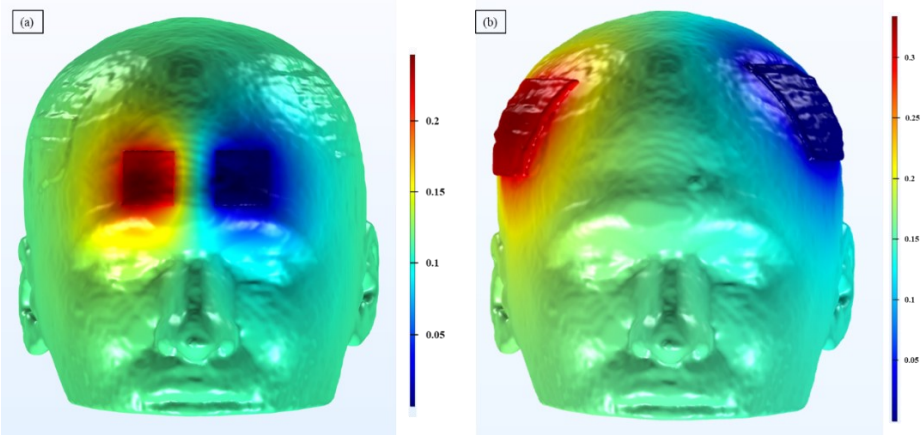

Figure 32 Trigeminal nerve branches were overlapped on voltage volume models found from FEM simulation. Part (a) represents RS-LS montage where voltage distribution ranges from 0-0.29 V and part (b) represents F3-F4 montage where voltage distribution ranges from 0-0.34 V.

6.2.4. NEURON modeling

Two axon models were developed. One to represent a sensory myelinated axon and another to represent an unmyelinated axon and are described below.

6.2.4.1. Building myelinated axons

Physiological ion channel properties of a sensory myelinated nerve containing FLUT, MYSA, STIN and NODE compartments were assigned following the specification used by Gaines et al. [118] and has been previously explained in chapter 3. The voltage input to NEURON was found by mapping along the geometry of trigeminal nerve from FEM generated volumes. An approximate length of the drawn nerve was found using 3D

coordinates of the start and end points of the nerves. The myelinated axon models were compartmentalized according to internodal lengths provided by MRG group [66] (explained in chapter 3) depending on axon diameter as shown in table 8.

Table 8 Lengths of drawn nerves and number of nodes created for myelinated axon models.

	Auriculo-temporal n.	Zygomatico-temporal n.	Supraorbital n.	Supra-trochlear n.	Infra-trochlear n.	Infraorbital n.	Buccal n.
Length of drawn nerve (mm)	64.7	56.4	61.8	59	31.4	39.2	44.6
# nodes in a myelinated axon of diameter 6um	111	99	107	102	55	67	77
# nodes in a myelinated axon of diameter 18um	41	37	39	38	21	25	29

6.2.4.2. Building unmyelinated axons

Many computational models studying peripheral nerve stimulation have only used myelinated fibers for assessing neural activity [118], [133]. Although multiple post-mortem mammalian histology studies suggest that peripheral nerve bundles consist of more than 60% unmyelinated axons [69]. Also unmyelinated axons have slower conduction velocity and higher activation threshold than myelinated axons [67], [69] making the use of unmyelinated axon models integral to understanding peripheral nerve selectivity. An unmyelinated axon model was built with ion channel properties based on the works by

Sundt et al. [135] (https://senselab.med.yale.edu/modeldb/, Accession No. 187473) and reference computation parameters needed for external stimulation were confirmed using the research by Pelot et al. [69]. The shape of action potential, strength-duration curves found from using TES simulations with unmyelinated axons were compared to the published models for verification. The range of conduction velocity values were also compared for verification (Figure 33). The shape of space plots of myelinated vs unmyelinated axons was also compared to show differences in action potential propagation.

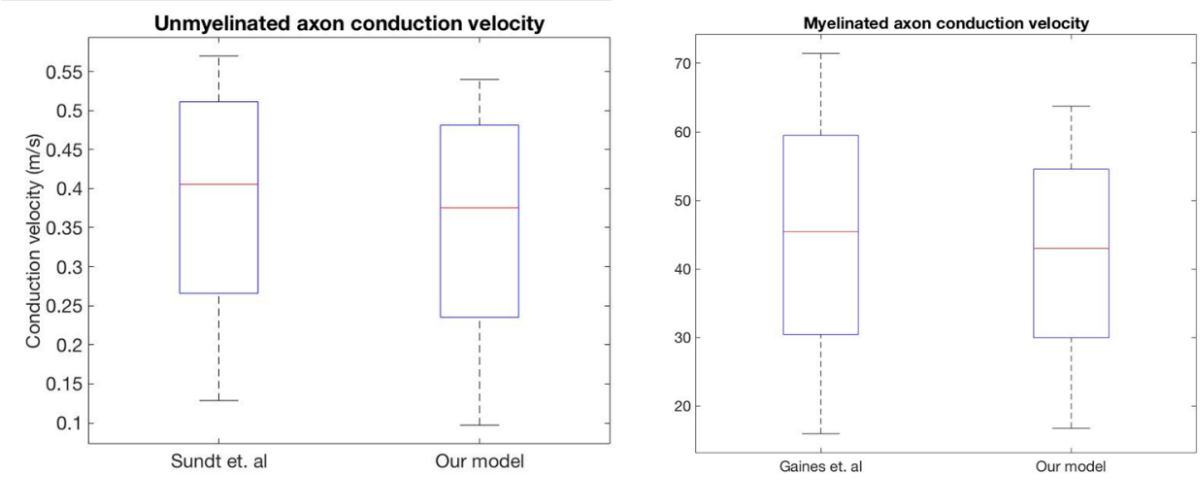

Figure 33 Difference in conduction velocity between a myelinated and unmyelinated axon and corresponding values from literature.

Conduction speed in myelinated axon is much faster than unmyelinated axon as expected. Also, the conduction speed increased with an increase in axon diameter in both cases as expected.

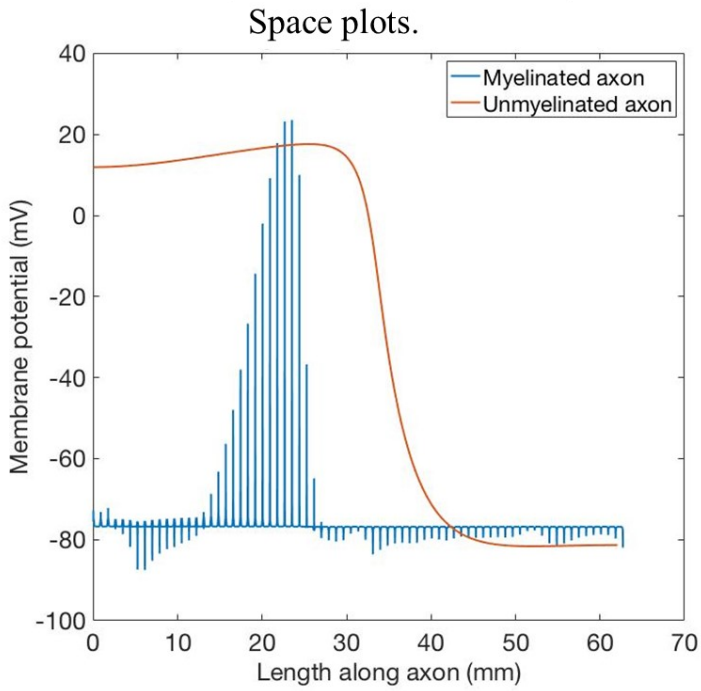

Figure 34 Difference in space plots between an unmyelinated and myelinated axon. The graph shows how membrane potential in all the segments in an unmyelinated axon (red plot) increases whereas in a myelinated axon only the NODE segments are affected (blue plot) i.e., action potentials only occur at the nodes in myelinated axons.

Following quasi-static assumption, the extracellular medium is purely resistive and hence a time-dependent waveform can be multiplied to the corresponding extracellular potential

value at each node. The cable equation [136] was solved in the NEURON environment model in each waveform condition.

6.2.5. Displacement studies

6.2.5.1. Electrode displacement

For TNS experiments, electrodes are placed approximately over the supraorbital foramen location on both sides of the forehead (RS – LS). Electrodes were displaced both horizontally (medial and lateral directions) (Figure 35) and vertically (superior direction) in increments of 1 mm. In each case, the new displaced electrode locations were outlined in Simpleware and FEM calculations were repeated to generate new extracellular voltage distributions. The induced potential information was transferred to NEURON environment to study effects on percentage activation fractions in the case of STN.

6.2.6. Statistical analysis

6.2.6.1. Building a nerve fascicle

The activation fraction for a nerve fascicle with representative realistic radius distribution was estimated statistically. As individual peripheral trigeminal nerve fascicles are in the range of 250–400 μm diameter [137], [138] which is extremely small, the extracellular voltage due to TES faced by an axon is assumed independent of its location within a single

fascicle. An axon diameter distribution is considered from relevant literature. Heasman et al. [139] performed post-mortem studies on multiple subjects and found the distribution of myelinated fiber diameters in human inferior alveolar nerves (a tributary of the trigeminal n.) to predominantly have a bimodal curve with one peak in the smaller diameter range (2-5 μm) and one in the larger diameter range (8-10 μm). Not much information was found about the diameter distribution of c-type fibers in trigeminal nerves in human subjects. The final unmyelinated fiber diameters were decided based on multiple animal studies and data from human vagus nerve distribution [69], [140]–[142].

6.2.6.2. Activation fractions

The activated axons (i.e., number of activated axons/ total number of axons), seen in a nerve fascicle due to electrode displace was calculated in every case. Fractions corresponding to activation of only myelinated and unmyelinated axons were calculated.

6.3. Results

The effects of using a pulsatile bipolar waveform of 100 ms pulse width on the recruitment of all the seven peripheral nerves were studied to identify whether peripheral nerves could be activated during common TES experiments. Further to specifically replicate focused TNS experiments, a waveform having a symmetrical biphasic current pulse of 250 μs was also used on the STN under the RS-LS montage and electrode displacement was performed.

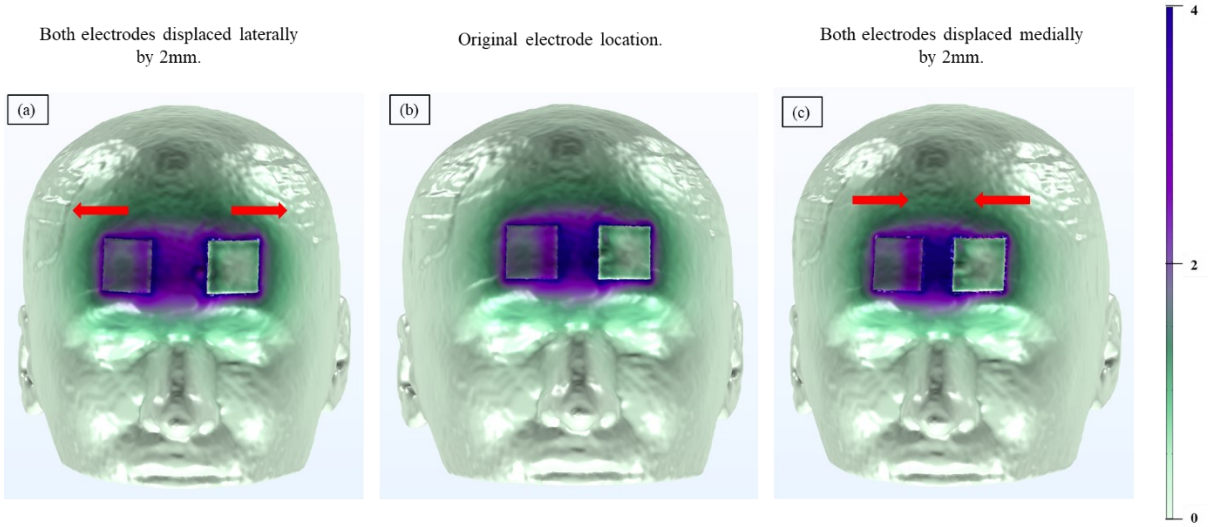

Figure 35 Representation of lateral (a) and medial (c) displacements and corresponding current density (A/m^2) values observed.

The following results were inferred from peripheral nerve TES modelling studies:

6.3.1. Fascicle diameter distribution

A fascicle consisting of 500 axons with 60% unmyelinated axon and 40% myelinated axons was considered (Figure 36). Unmyelinated axons had a peak at 2.5 µm with a standard deviation of 1.13 µm and the myelinated axon distribution had dual peaks at 5 µm and 10µm with a standard deviation of 2.75 µm.

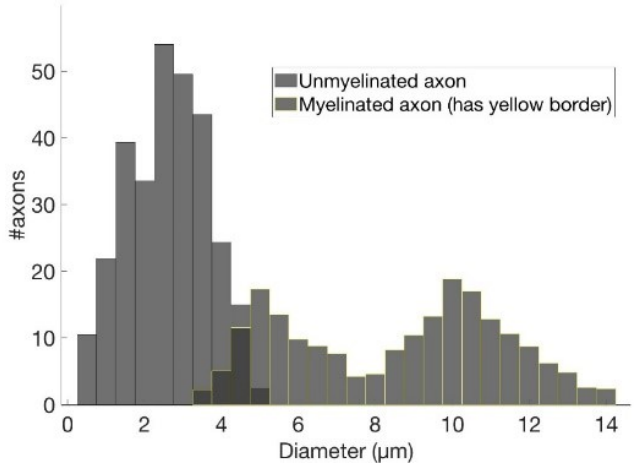

Figure 36 Example of diameter distribution in the nerve fascicle used for quantification of displacement studies.

6.3.2. Extent of nerve activation in the face using a TES waveform

Stimulation threshold required to activate the following seven peripheral branches of the trigeminal nerve: Auriculotemporal n. (ATN), Zygomaticotemporal n. (ZTN), Supraorbital n. (SON), Supratrochlear n. (STN), Infratrochlear n. (ITN), Infraorbital n. (IFN), and Buccal n. (BN) were calculated for both F3-F4 and RS-LS montages (Figure 37) using anodal stimulation. In both electrode montages, unmyelinated axons predicted higher thresholds. Nerves located directly under the anode electrode had the lowest threshold values with activation of axons within the fascicle behaving independent of fiber diameter in this zone i.e., all axons were activated. The effect of fiber diameter on activation threshold is more pronounced in fibers located farther from the electrode.

To quantify this effect further histograms for individual nerves were plotted depicting activation fraction in response to a 4 mA pulsatile waveform with 100 ms pulse width (Figure 38, Figure 39). The amplitude 4mA was chosen as it is the maximum allowed safe current injection level according to TES protocols [143].

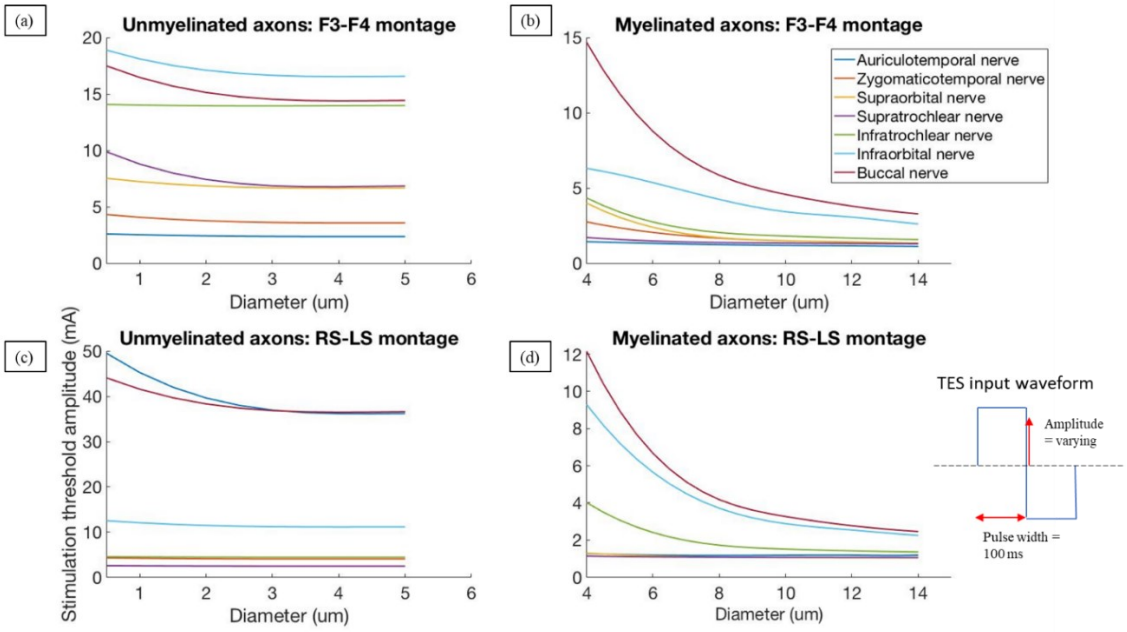

Figure 37 Stimulation threshold values for nerves across the scalp in case of two electrode montages. The required activation stimulation threshold is more sensitive to diameter for nerve branches located farther from the electrode.

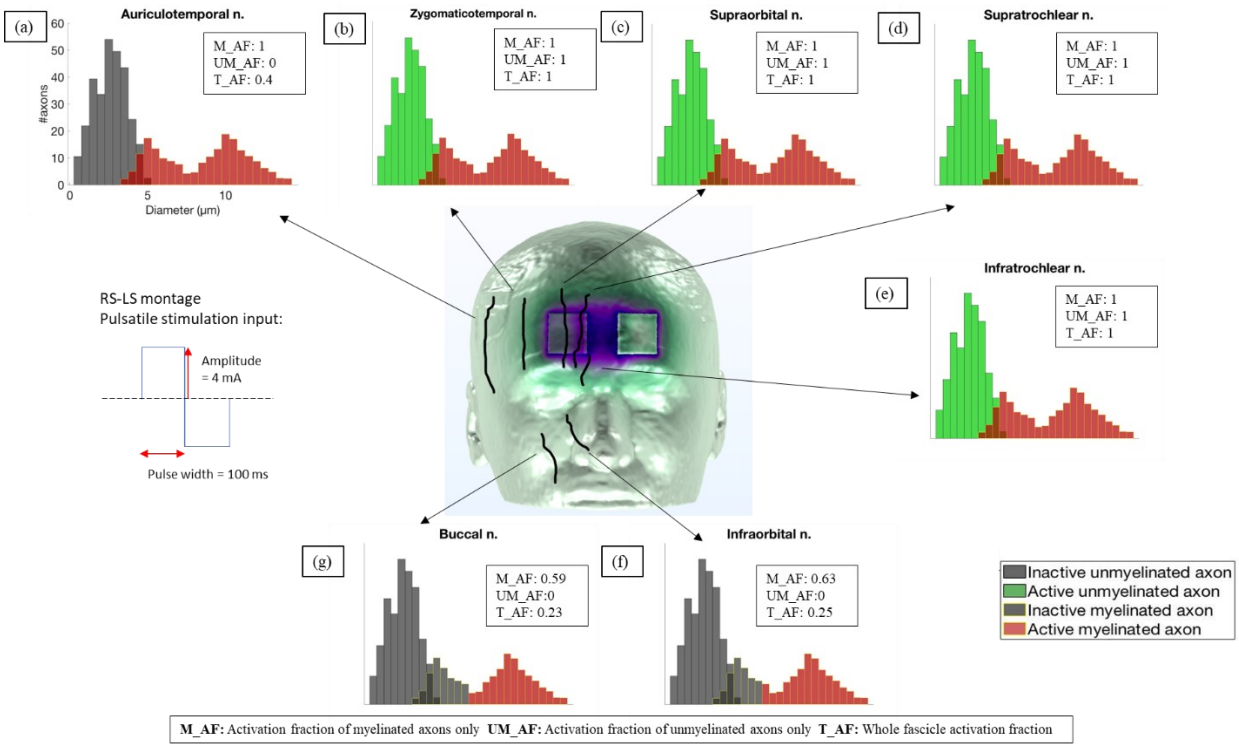

Figure 38 Representation of activation fraction across different nerve branches innervating the face: RS-LS montage. Projections of nerve branches are shown on the current density image.

All the nerve branches near the anode (ZTN, SON,STN, and ITN) were activated and had activation fractions of 1.

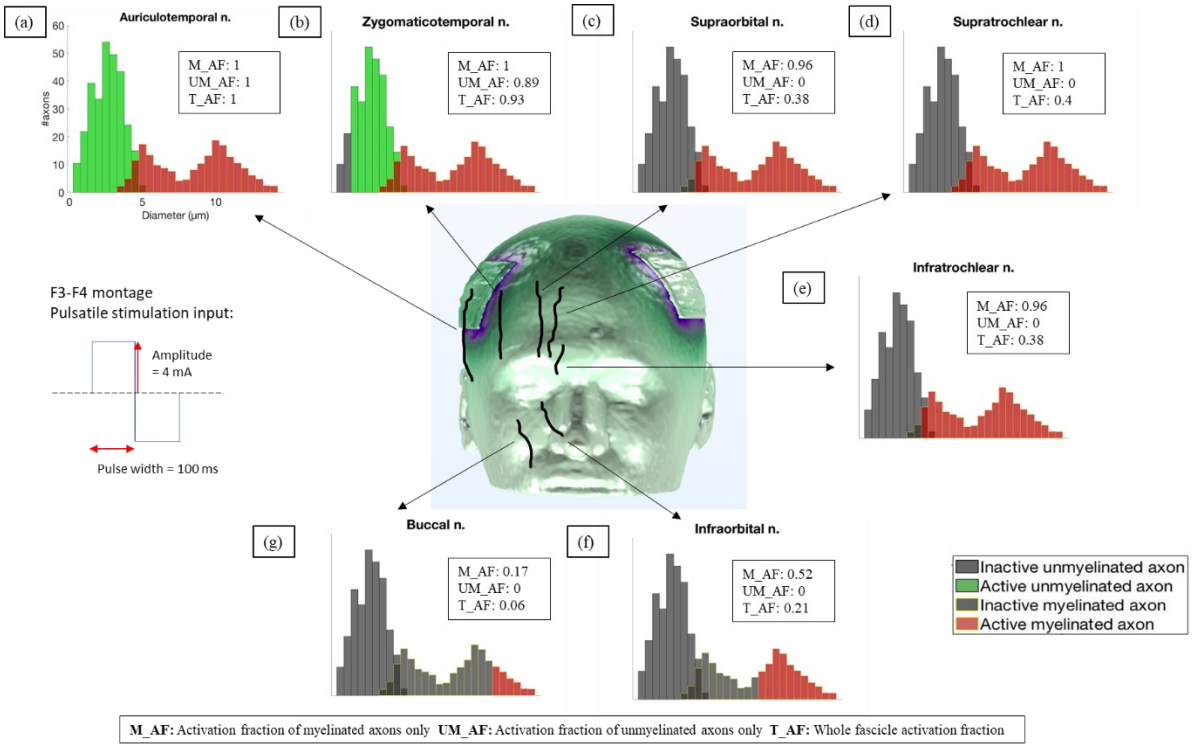

Figure 39 Representation of activation fraction across different nerve branches innervating the face: F3- F4 montage. Projections of nerve branches are shown on the current density image.

All the nerve branches in the forehead near the anode (ATN, ZTN) were activated and have total activation fraction > 0.9. Moving away from the anode along the scalp (SON, STN, ITN), most myelinated axons were still activated (M_AF > 0.9) due to their lower thresholds compared to c-type fibers. Whereas, in farther away nerve fibers (ION, BN) only larger diameters of myelinated axons were activated with no unmyelinated axon activation.

6.3.3. Displacement studies

Even with careful placement, the location of electrodes can vary over sessions due to human error [111], [144], [145]. This may reduce neural excitability and result in a lower therapeutic output. This effect was studied by causing a 1 – 3 mm displacement (to the center of both the anode and ground electrodes) in superior, medial, and lateral directions with respect to the original electrode location. This displacement amount was chosen as this the expected human error in electrode placement.

6.3.3.1. Horizontal displacement of electrodes

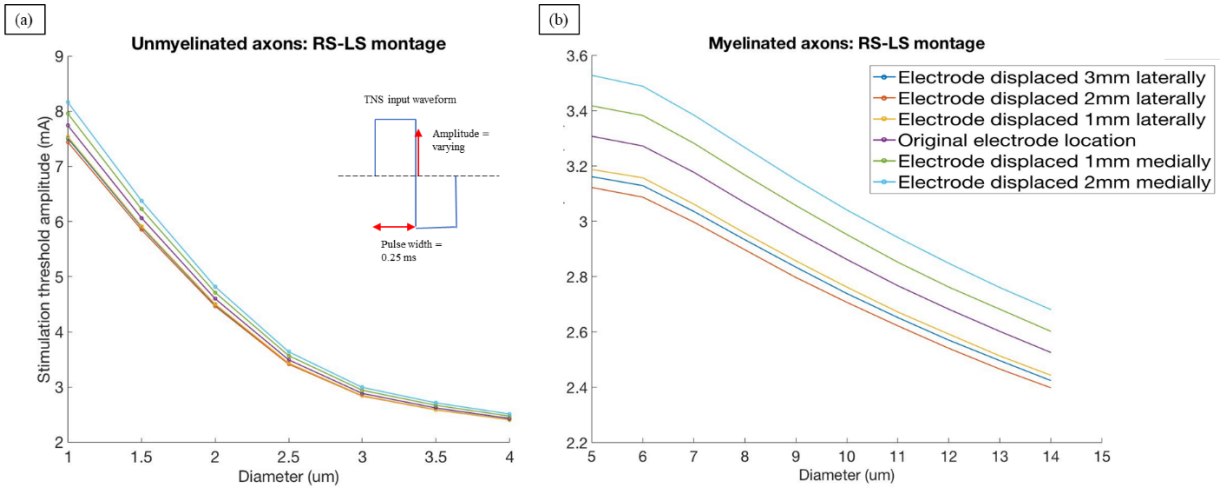

Figure 40 Change in threshold levels due to medial and lateral (horizontal) displacement of electrodes with respect to the ST branch.

The thresholds increased when the electrodes were moved horizontally closer (1 mm and 2 mm medial displacement) as the effective field strengths decreased. When the electrodes were moved horizontally farther apart from the original positioning, threshold

decreased (1 mm and 2 mm lateral displacement) up to an extent after which thresholds increase again with continued displacement (3 mm lateral displacement).

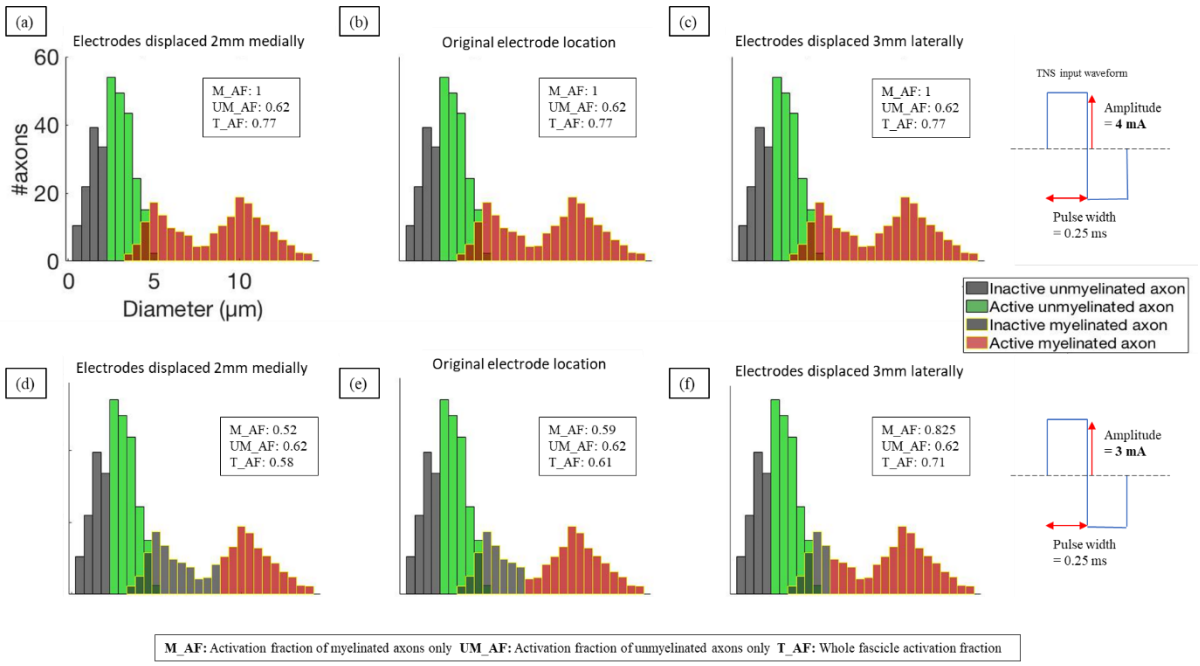

Figure 41 Activation fraction (AF) analysis to quantify neural selectivity effects in case of horizontal electrode displacement.

The top row represents the case for 4 mA stimulation, and the bottom row represents the case for 3 mA stimulation. The AFs changes (for example in case of 3 mA, the lowest AF is 0.58 (d) and highest AF is 0.71 (f)) with electrode displacement. Although, if the fascicle was considered to be recruited at 50% total AF, the ST fiber will be recruited in all electrode positioning setting imply no impact of horizonal displacement.

6.3.3.2. Vertical displacement of electrodes

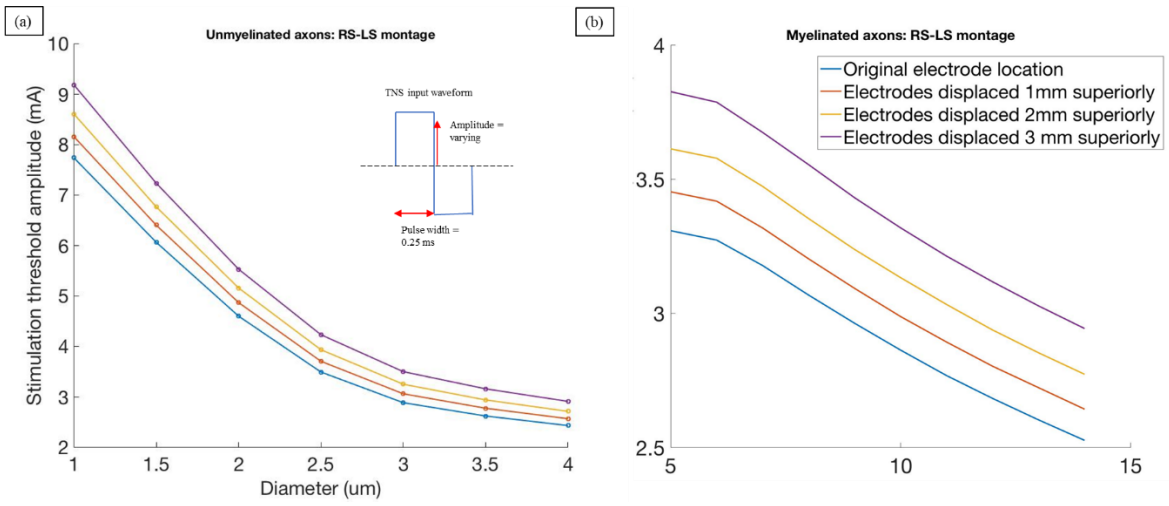

Figure 42 Change in threshold levels due to superior (vertical) displacement of electrodes with respect to the ST branch.

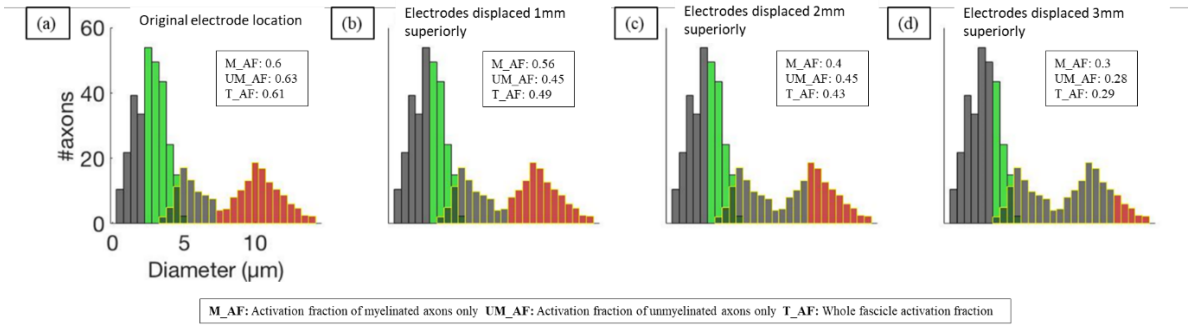

Figure 43 Activation fraction (AF) analysis to quantify neural selectivity effects in case of superior (vertical) electrode displacement.

AFs consistently decrease as the electrodes are moved in the superior direction and is consistent with the fact that the excitability of the fascicle is lower as the stimulating electrode is moved farther.

6.3.4. Significance of unmyelinated axons

As unmyelinated axons in trigeminal nerve branches are sensory afferents, activating unmyelinated axons through external stimulation may lead to sensation of pain and discomfort. Side effects of pain have often been reported by users of TES devices, for example, the Cefaly device [146] used for migraine therapy, reported over 50% subjects felt pain which was a leading cause for discontinuation. Stimulation thresholds for unmyelinated axons are higher than myelinated axons. The hybrid simulation model developed above was used to find a maximum stimulation amplitude at which no unmyelinated axons are activated but maximum myelinated axons are activated.

In the case of F3 – F4 electrode montage the maximum amplitude was 2.39 mA and in case of RS – LS montage the maximum amplitude was 2.44 mA. This was found by looking at the lowest activating threshold of the largest diameter unmyelinated axon in every case (Figure 37). The stimulation threshold from the previous experiments (Figure 38, Figure 39) was reduced to 2.2 mA and studied for activation of myelinated axons while no unmyelinated axons were active (Figure 44, Figure 45).

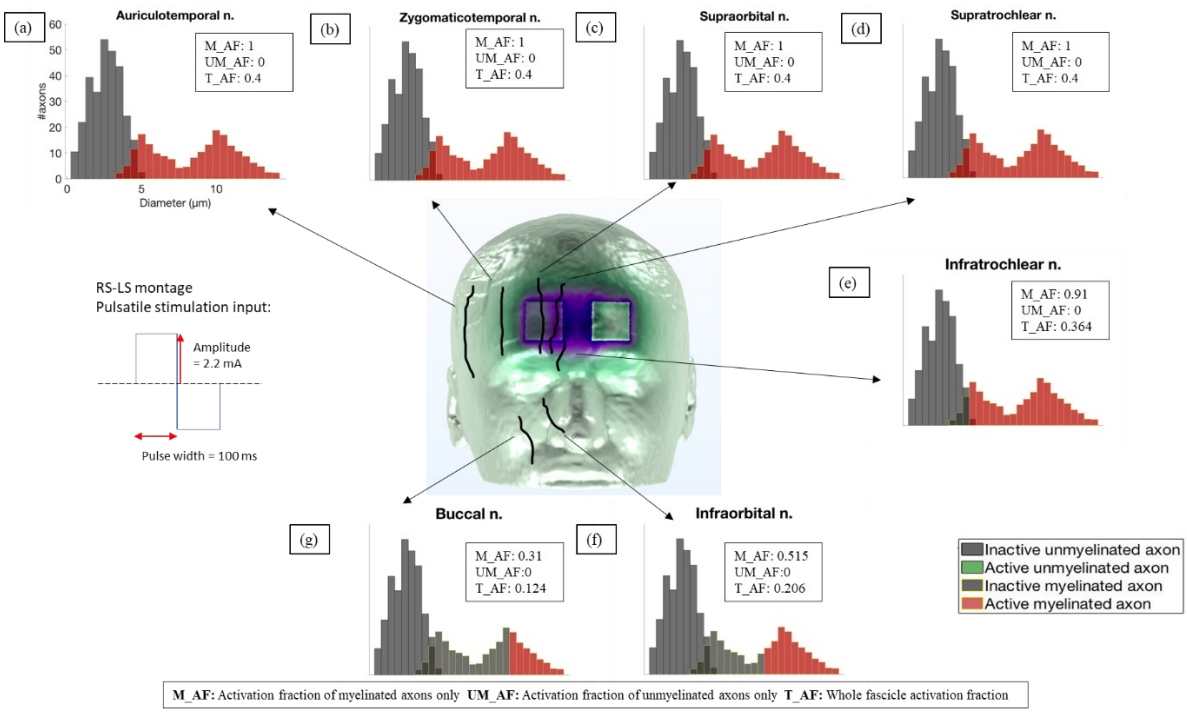

Figure 44 Representation of activation fraction across different nerve branches innervating the face: RS-LS montage for a stimulation amplitude of 2.2 mA where no unmyelinated axons are activated. Projections of nerve branches are shown on the current density image.

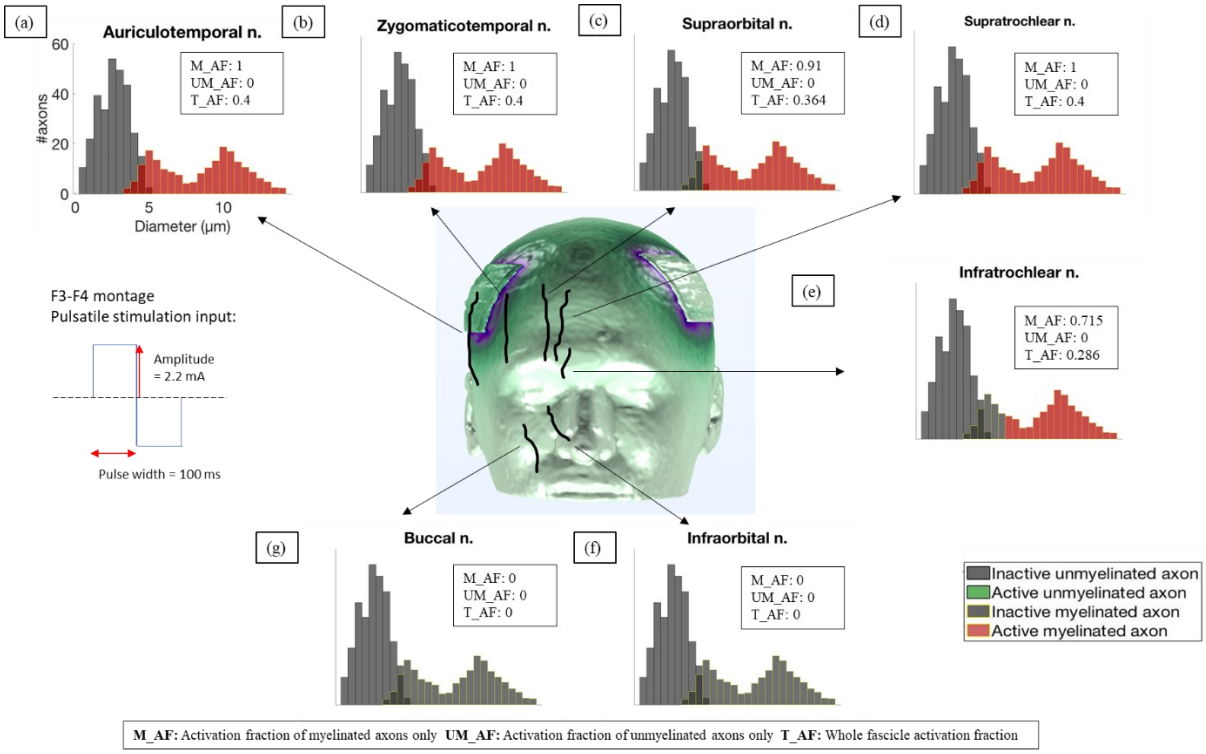

Figure 45 Representation of activation fraction across different nerve branches innervating the face: F3-F4 montage for a stimulation amplitude of 2.2 mA where no unmyelinated axons are activated. Projections of nerve branches are shown on the current density image.

6.4. Discussion

It is important to note that myelinated axons have a greater extent of activation due to their lower thresholds [67]. For both electrode montages more than 80% myelinated axons are activated in all nerve fascicles in the forehead. However unmyelinated axons become deactivated as the distance of the fascicle from the stimulating electrode increases. The axon distribution graphs (Figure 38, Figure 39) show that unmyelinated axons are the driving factor in fascicle activation level and according to literature more than 60% of fibers in a

peripheral nerve bundle are unmyelinated [69]. Although, activating unmyelinated axons may result in side-effects of pain and stimulation thresholds where only activation of myelinated axon is targeted may be used (Figure 44, Figure 45). This finding showcases the need to include unmyelinated axons in computational models of peripheral nerves for analyzing the effects of varying waveform on nerve selectivity and reduction of side effects. Many computational studies using myelinated axons consider the fiber bundle to be recruited if more than 50% of the myelinated axons are activated [67], [118]. Our findings suggest that computational fiber bundles should include both myelinated and unmyelinated axons and look for thresholds at which unmyelinated axons are inactive while >50% myelinated axons are active to maximize nerve selectivity and minimize side effects like pain. For example, at 4 mA stimulation (Figure 38), the unmyelinated activation fraction (UM_AF) is 1 for branches ZTN, SON, STN, and ITN, indicating possibility of pain sensation. But reducing the stimulation to 2.2 mA (Figure 44), for the same branches UM_AF is zero i.e., no unmyelinated axons are activated while the myelinated activation fraction (M_AF) remains >50% in every case, indicating the optimum case of nerve selectivity.

Axon selectivity refers to the ability to target and activate specific nerve fibers while avoiding side effects or the activation of others. Recent studies are focused on selectively activating desired peripheral nerve fibers [31], [67], [147]. Multiple research studies have found that displacements in nerve location and electrode location during external stimulation experiments may impact axon selectivity as displacements cause the spatial

relationship between the nerve and the electrodes [132], [144], [145]. To study this effect, we displaced the electrodes in a RS-LS montage in superior, medial, and lateral directions with respect to the ST nerve branch. An optimal point of lowest threshold was found while displacing the nerve horizontally i.e., the activation thresholds of both myelinated and unmyelinated axons increased when the electrodes were displaced medially and decreased to a certain extend when the electrodes were displaced laterally, after which further lateral displacement led to increase of thresholds. It may be beneficial for stimulation experiments to identify this optimal lowest threshold location to minimize side effects. In this case, the myelinated axons were the drivers of change in AF. This makes sense as the change in extracellular voltage distribution is relatively small between one electrode setting to another and affects myelinated axons to a greater extent as they are easily excitable.

Although the threshold values reported changes during horizontal displacements, it should be noted that total AF only changed by a small value. For example, in case of going from original electrode location to 2mm medial displacement, while the activation threshold for the smallest myelinated axon (5 μm) increased from 3.32 mA to 3.56 mA, the total activation fraction only changed from 0.61 to 0.58, implying the fiber was recruited (AF > 0.5) in both electrode settings despite displacements. This highlights the importance of studying and considering the diameter distribution of both myelinated and unmyelinated axons in computational studies investigating nerve fascicle recruitment as it can heavily influence the recruitment threshold and the threshold at which least side effects are observed.

Limitations of this study include the assumption that tissue properties are resistive and ephaptic coupling does not play a role in neural activity. The accuracy of predictions in modeling studies such as this one relies on the precise representation of anatomical structures, electrode specifications, and physiological properties of neurons and may need further improvement. To validate the computational findings and evaluate the impact of electrode positioning on peripheral nerve stimulation and pain levels, large scale clinical studies need to be conducted.

CHAPTER 7

SUMMARY AND FUTURE SCOPE.

7.1. Conclusion

Distal branches of the trigeminal nerve extending to the face were successfully identified using a combination of MPRAGE and CRANI imaging. Tractography of some of the trigeminal nerve branches outside the brain stem region was performed demonstrating the feasibility of tracking cranial nerves in DTI space using extraforaminal anatomical markers. The study demonstrates that a comprehensive large field of view (FOV) nerve visualization exam, encompassing the anatomy of all distal branches of the trigeminal nerve, can be accomplished within a relatively short acquisition time of 20 minutes using only pre-contrast CRANI and MPRAGE imaging techniques. The study suggests that the selection of nerve-specific regions of interest (ROIs) can streamline the scan time for clinical examinations, potentially making the procedure more efficient.

Additionally, the research successfully constructed hybrid computational models to explore the differences in neural excitability responses between a DTI-derived realistic intracranial trigeminal nerve axon and a straight axon using simulation models, paving the way for personalized neuromodulation simulations using tractography based nerve geometries. As intracranial axons were not excitable and did not provide much information about fiber selectivity, anatomy-informed models of peripheral nerve branches were created. The impact of nerve location shift and electrode displacement on axon recruitment

in TNS experiments, enhancing the understanding of TNS mechanisms and enabling personalized targeting. These established methods for visualizing and modeling trigeminal nerve neuromodulation can benefit researchers studying various cranial nerves for patient-specific diagnostic and therapeutic purposes.

7.2. Future scope:

The studies performed in this thesis provide background for exploring multiple more aspects of peripheral nerve imaging and neuromodulation described below:

7.2.1. Nerve visualization.

Although multiple new T-2 weighted MRI sequences are being developed, many tailored specifically towards cranial nerve imaging [1], [89], [148], few find extensive use clinically [7]. Further research should concentrate on producing more replication and usability studies spanning across multiple imaging centers and study populations. This is necessary to increase the clinical utility of newly developed sequences. Identification studies using CRANI images were performed in healthy adults and need to be extended to studying trigeminal neuralgia cases to understand anatomical changes in pathology. Similarly, more application-based studies should also explore tractography of nerves. The analysis from diffusion tractography studies can be improved by using focused field of view with higher resolution DTI acquisition as whole brain DTI acquisitions present more susceptibility error [5], [100]. The use of nerve specific DTI sequence in tractography pipeline should also be explored. The tractography pipelines established

here should be further studies in patients with trigeminal neuralgia and multiple sclerosis to understand changes in FA values in case of pathology and demyelination of nerves.

7.2.2. Peripheral computational models of neural activation.

The neuromodulation study performed in this thesis varied a few parameters (myelinated and unmyelinated axon diameters, distance of nerve from electrode and electrode drift) that affect nerve activation. Although the space of the parameters is larger can be categorized into multiple groups like pulse properties, electrode properties, axon properties, fascicle properties, and configuration properties and these need extensive research tailored towards peripheral cranial nerves [73], [74], [147], [149]. The pertinent need to include unmyelinated axons in computational fiber models was established. More animal histology and post-mortem research is needed in understanding distribution of fiber diameters in trigeminal nerves as this plays a role in understanding neural activation patterns. We concluded that peripheral trigeminal branches running directly under the stimulating electrode get activated during TES sessions. The involvement of cranial nerves in the mechanisms facilitating TES-based neuromodulation needs more research [30], [31], [129].

REFERENCES

[1] A. M. Blitz *et al.*, "Contrast-enhanced CISS imaging for evaluation of neurovascular compression in trigeminal neuralgia: Improved correlation with symptoms and prediction of surgical outcomes," in *American Journal of Neuroradiology*, 2018, vol. 39, no. 9, doi: 10.3174/ajnr.A5743.

[2] E. Ciftci, Y. Anik, A. Arslan, G. Akansel, T. Sarisoy, and A. Demirci, "Driven equilibrium (drive) MR imaging of the cranial nerves V-VIII: Comparison with the T2-weighted 3D TSE sequence," *Eur. J. Radiol.*, vol. 51, no. 3, 2004, doi: 10.1016/j.ejrad.2003.10.019.

[3] J. Casselman *et al.*, "3D CRANI, a novel MR neurography sequence, can reliable visualise the extraforaminal cranial and occipital nerves," *Eur. Radiol.*, Nov. 2022, doi: 10.1007/s00330-022-09269-2.

[4] K. A. Cauley and C. G. Filippi, "Diffusion-tensor imaging of small nerve bundles: Cranial nerves, peripheral nerves, distal spinal cord, and lumbar nerve roots-Clinical applications," *Am. J. Roentgenol.*, vol. 201, no. 2, 2013, doi: 10.2214/AJR.12.9230.

[5] T. Jacquesson *et al.*, "Full tractography for detecting the position of cranial nerves in preoperative planning for skull base surgery: Technical note," *J. Neurosurg.*, vol. 132, no. 5, 2020, doi: 10.3171/2019.1.JNS182638.

[6] A. L. Alexander, "Deterministic White Matter Tractography," in *Diffusion MRI*, 2013.

[7] T. Jacquesson *et al.*, "Overcoming Challenges of Cranial Nerve Tractography: A Targeted Review," *Clinical Neurosurgery*, vol. 84, no. 2. 2019, doi: 10.1093/neuros/nyy229.

[8] J. Ma *et al.*, "Preoperative visualization of cranial nerves in skull base tumor surgery using diffusion tensor imaging technology," *Turk. Neurosurg.*, vol. 26, no. 6, 2016, doi: 10.5137/1019-5149. JTN.13655-14.1.

[9] M. Hodaie, J. Quan, and D. Q. Chen, "In vivo visualization of cranial nerve pathways in humans using diffusion-based tractography," *Neurosurgery*, vol. 66, no. 4, 2010, doi: 10.1227/01.NEU.0000367613.09324.DA.

[10] Y. H. Koh *et al.*, “Evaluation of trigeminal nerve tractography using two-fold-accelerated simultaneous multi-slice readout-segmented echo planar diffusion tensor imaging,” *Eur. Radiol.*, vol. 31, no. 2, 2021, doi: 10.1007/s00330-020-07193-x.

[11] B. Kaya, P. Geha, I. de Araujo, I. Cioffi, and M. Moayedi, “Identification of central amygdala and trigeminal motor nucleus connectivity in humans: An ultra-high field diffusion MRI study,” *Hum. Brain Mapp.*, vol. 44, no. 4, 2023, doi: 10.1002/hbm.26104.

[12] M. Hodaie, D. Q. Chen, J. Quan, and N. Laperriere, “Tractography delineates microstructural changes in the trigeminal nerve after focal radiosurgery for trigeminal neuralgia,” *PLoS One*, vol. 7, no. 3, 2012, doi: 10.1371/journal.pone.0032745.

[13] M. Yoshino *et al.*, “Visualization of cranial nerves using high-definition fiber tractography,” *Neurosurgery*, vol. 79, no. 1, pp. 146–165, 2016, doi: 10.1227/NEU.0000000000001241.

[14] F. van der Cruyssen, T. M. Croonenborghs, R. Hermans, R. Jacobs, and J. Casselman, “3D cranial nerve imaging, a novel MR neurography technique using black-blood STIR TSE with a pseudo steady-state sweep and motion-sensitized driven equilibrium pulse for the visualization of the extraforaminal cranial nerve branches,” *Am. J. Neuroradiol.*, vol. 42, no. 3, 2021, doi: 10.3174/AJNR.A6904.

[15] E. Santarnecchi, A. K. Brem, E. Levenbaum, T. Thompson, R. C. Kadosh, and A. Pascual-Leone, “Enhancing cognition using transcranial electrical stimulation,” *Current Opinion in Behavioral Sciences*, vol. 4. 2015, doi: 10.1016/j.cobeha.2015.06.003.

[16] T. Wagner, A. Valero-Cabre, and A. Pascual-Leone, “Noninvasive human brain stimulation,” *Annual Review of Biomedical Engineering*, vol. 9. 2007, doi: 10.1146/annurev.bioeng.9.061206.133100.

[17] D. C. W. Klooster *et al.*, “Technical aspects of neurostimulation: Focus on equipment, electric field modeling, and stimulation protocols,” *Neuroscience and Biobehavioral Reviews*, vol. 65. pp. 113–141, 2016, doi: 10.1016/j.neubiorev.2016.02.016.

[18] P. G. Shekelle, I. A. Cook, I. M. Miake-Lye, M. S. Booth, J. M. Beroes, and S. Mak, "Benefits and harms of cranial electrical stimulation for chronic painful conditions, depression, anxiety, and insomnia a systematic review," *Annals of Internal Medicine*, vol. 168, no. 6. 2018, doi: 10.7326/M17-1970.

[19] J. J. McGough *et al.*, "Double-Blind, Sham-Controlled, Pilot Study of Trigeminal Nerve Stimulation for Attention-Deficit/Hyperactivity Disorder," *J. Am. Acad. Child Adolesc. Psychiatry*, vol. 58, no. 4, 2019, doi: 10.1016/j.jaac.2018.11.013.

[20] A. B. Antony, A. J. Mazzola, G. S. Dhaliwal, and C. W. Hunter, "Neurostimulation for the treatment of chronic head and facial pain: A literature review," *Pain Physician*, vol. 22, no. 5, 2019, doi: 10.36076/ppj/2019.22.447.

[21] C. M. DeGiorgio, A. Shewmon, D. Murray, and T. Whitehurst, "Pilot study of Trigeminal Nerve Stimulation (TNS) for epilepsy: A proof-of-concept trial," *Epilepsia*, vol. 47, no. 7, 2006, doi: 10.1111/j.1528-1167.2006.00594.x.

[22] L. Bradnam and C. Barry, "The Role of the Trigeminal Sensory Nuclear Complex in the Pathophysiology of Craniocervical Dystonia," *J. Neurosci.*, vol. 33, no. 47, pp. 18358–18367, 2013, doi: 10.1523/JNEUROSCI.3544-13.2013.

[23] M. C. Pellicciari and C. Miniussi, "Transcranial Direct Current Stimulation in Neurodegenerative Disorders," *Journal of ECT*, vol. 34, no. 3. pp. 193–202, 2018, doi: 10.1097/YCT.0000000000000539.

[24] S. Carvalho, J. Leite, and F. Fregni, "Transcranial Alternating Current Stimulation and Transcranial Random Noise Stimulation," in *Neuromodulation*, 2018, pp. 1611–1617.

[25] I. Moreno-Duarte *et al.*, "Transcranial Electrical Stimulation: Transcranial Direct Current Stimulation (tDCS), Transcranial Alternating Current Stimulation (tACS), Transcranial Pulsed Current Stimulation (tPCS), and Transcranial Random Noise Stimulation (tRNS)," in *The Stimulated Brain: Cognitive Enhancement Using Non-Invasive Brain Stimulation*, 2014.

[26] I. Aprinda, C. Munish, S. Benjamin, and J. S. Rosalind, "Changing head model extent affects finite element predictions of transcranial direct current stimulation distributions," *J. Neural Eng.*, vol. 13, no. 6, p. 66006, 2016, doi: 10.1088/1741-2560/13/6/066006.CHANGING.

[27] Y. Huang, A. Datta, M. Bikson, and L. C. Parra, “Realistic volumetric-approach to simulate transcranial electric stimulation - ROAST - a fully automated open-source pipeline,” *J. Neural Eng.*, vol. 16, no. 5, 2019, doi: 10.1088/1741-2552/ab208d.

[28] A. K. Kasinadhuni, A. Indahlastari, M. Chauhan, M. Schär, T. H. Mareci, and R. J. Sadleir, “Imaging of current flow in the human head during transcranial electrical therapy,” *Brain Stimul.*, vol. 10, no. 4, pp. 764–772, 2017, doi: 10.1016/j.brs.2017.04.125.

[29] M. Vöröslakos *et al.*, “Direct effects of transcranial electric stimulation on brain circuits in rats and humans,” *Nat. Commun.*, vol. 9, no. 1, 2018, doi: 10.1038/s41467-018-02928-3.

[30] L. van Boekholdt, S. Kerstens, A. Khatoun, B. Asamoah, and M. Mc Laughlin, “tDCS peripheral nerve stimulation: a neglected mode of action?,” *Mol. Psychiatry*, vol. 26, no. 2, 2021, doi: 10.1038/s41380-020-00962-6.

[31] D. Adair *et al.*, “Electrical stimulation of cranial nerves in cognition and disease,” *Brain Stimulation*, vol. 13, no. 3. 2020, doi: 10.1016/j.brs.2020.02.019.

[32] J. Shapey *et al.*, “Clinical applications for diffusion MRI and tractography of cranial nerves within the posterior fossa: A systematic review,” *Frontiers in Neuroscience*, vol. 13, no. FEB. 2019, doi: 10.3389/fnins.2019.00023.

[33] K. S. Chan, D. G. Norris, and J. P. Marques, “Structure tensor informed fibre tractography at 3T,” *Hum. Brain Mapp.*, vol. 39, no. 11, 2018, doi: 10.1002/hbm.24283.

[34] D. Thaploo, A. Joshi, C. Georgiopoulos, J. Warr, and T. Hummel, “Tractography indicates lateralized differences between trigeminal and olfactory pathways,” *Neuroimage*, vol. 261, 2022, doi: 10.1016/j.neuroimage.2022.119518.

[35] M. A. Nitsche *et al.*, “Transcranial direct current stimulation: State of the art 2008,” *Brain Stimulation*. 2008, doi: 10.1016/j.brs.2008.06.004.

[36] I. Laakso, S. Tanaka, S. Koyama, V. De Santis, and A. Hirata, “Inter-subject variability in electric fields of motor cortical tDCS,” *Brain Stimul.*, vol. 8, no. 5, 2015, doi: 10.1016/j.brs.2015.05.002.

[37] S. Lee, C. Lee, J. Park, and C. H. Im, “Individually customized transcranial temporal interference stimulation for focused modulation of deep brain structures: a simulation study with different head models,” *Sci. Rep.*, vol. 10, no. 1, pp. 1–11, 2020, doi: 10.1038/s41598-020-68660-5.

[38] T. Marur, Y. Tuna, and S. Demirci, “Facial anatomy,” *Clinics in Dermatology*, vol. 32, no. 1. 2014, doi: 10.1016/j.clindermatol.2013.05.022.

[39] M. Sindou and A. Brinzeu, “Anatomy of the Trigeminal Nerve (TGN),” in *Trigeminal Neuralgias: A Neurosurgical Illustrated Guide*, 2023.

[40] W. Joo, F. Yoshioka, T. Funaki, K. Mizokami, and A. L. Rhoton, “Microsurgical anatomy of the trigeminal nerve,” *Clinical Anatomy*, vol. 27, no. 1. 2014, doi: 10.1002/ca.22330.

[41] D. P. Seeburg, B. Northcutt, N. Aygun, and A. M. Blitz, “The Role of Imaging for Trigeminal Neuralgia,” *Neurosurg. Clin. N. Am.*, vol. 27, no. 3, 2016, doi: 10.1016/j.nec.2016.02.004.

[42] N. Romano, M. Federici, and A. Castaldi, “Imaging of cranial nerves: a pictorial overview,” *Insights into Imaging*, vol. 10, no. 1. 2019, doi: 10.1186/s13244-019-0719-5.

[43] Bista and Imlach, “Pathological Mechanisms and Therapeutic Targets for Trigeminal Neuropathic Pain,” *Medicines*, vol. 6, no. 3, 2019, doi: 10.3390/medicines6030091.

[44] N. Nonaka, N. Goto, H. Ezure, H. Ishikawa, and K. Oka, “Unmyelinated Nerve Fibers of the Human Mandibular Nerve,” *Okajimas Folia Anat. Jpn.*, vol. 77, no. 6, 2001, doi: 10.2535/ofaj1936.77.6_217.

[45] G. De Stefano *et al.*, “Unravelling the role of unmyelinated nerve fibres in trigeminal neuralgia with concomitant continuous pain,” *Clin. Neurophysiol.*, vol. 142, 2022, doi: 10.1016/j.clinph.2022.07.502.

[46] P. Tyler and S. Butt, “Basic principles of MRI,” in *Radionuclide and Hybrid Bone Imaging*, vol. 9783642024009, 2012.

[47] D. Sinclair, “MRI Principles,” *Radiography*, vol. 10, no. 3, 2004, doi:

10.1016/j.radi.2004.04.001.

[48] U. Atxitia, D. Hinzke, and U. Nowak, “Fundamentals and applications of the Landau-Lifshitz-Bloch equation,” *Journal of Physics D: Applied Physics*, vol. 50, no. 3. 2017, doi: 10.1088/1361-6463/50/3/033003.

[49] J. Hrabe, G. Kaur, and D. N. Guilfoyle, “Principles and limitations of NMR diffusion measurements,” *J. Med. Phys.*, 2007, doi: 10.4103/0971-6203.31148.

[50] E. Yang, P. G. Nucifora, and E. R. Melhem, “Diffusion MR Imaging: Basic Principles,” *Neuroimaging Clinics of North America*, vol. 21, no. 1. 2011, doi: 10.1016/j.nic.2011.02.001.

[51] R. Bammer, “Basic principles of diffusion-weighted imaging,” *Eur. J. Radiol.*, 2003, doi: 10.1016/S0720-048X(02)00303-0.

[52] S. Mori and J. Zhang, “Principles of Diffusion Tensor Imaging and Its Applications to Basic Neuroscience Research,” *Neuron*, vol. 51, no. 5. 2006, doi: 10.1016/j.neuron.2006.08.012.

[53] T. Li *et al.*, “The significance of diffusion tensor magnetic resonance imaging for patients with nasopharyngeal carcinoma and trigeminal nerve invasion,” *Med. (United States)*, vol. 96, no. 6, 2017, doi: 10.1097/MD.0000000000006072.

[54] A. L. Alexander, J. E. Lee, M. Lazar, and A. S. Field, “Diffusion Tensor Imaging of the Brain,” *Neurotherapeutics*, vol. 4, no. 3, 2007, doi: 10.1016/j.nurt.2007.05.011.

[55] P. W. Kuchel *et al.*, “Stejskal-tanner equation derived in full,” *Concepts Magn. Reson. Part A Bridg. Educ. Res.*, vol. 40 A, no. 5, 2012, doi: 10.1002/cmr.a.21241.

[56] G. Paxinos and J. K. Mai, *The Human Nervous System*. 2003.

[57] A. M. M. Sousa, K. A. Meyer, G. Santpere, F. O. Gulden, and N. Sestan, “Evolution of the Human Nervous System Function, Structure, and Development,” *Cell*, vol. 170, no. 2. 2017, doi: 10.1016/j.cell.2017.06.036.

[58] S. Vucic and M. C. Kiernan, “Transcranial Magnetic Stimulation for the Assessment of Neurodegenerative Disease,” *Neurotherapeutics*, vol. 14, no. 1. pp. 91–106, 2017, doi: 10.1007/s13311-016-0487-6.

[59] J. M. Baraban, “Viewing Brain Stimulation from a Plasticity Perspective,” in *Brain Stimulation: Methodologies and Interventions*, 2015.

[60] L. C. Parra and M. Bikson, “Model of the effect of extracellular fields on spike time coherence,” in *Annual International Conference of the IEEE Engineering in Medicine and Biology - Proceedings*, 2004, vol. 26 VI, doi: 10.1109/iembs.2004.1404271.

[61] A. V. Tavakoli and K. Yun, “Transcranial alternating current stimulation (tACS) mechanisms and protocols,” *Frontiers in Cellular Neuroscience*, vol. 11. 2017, doi: 10.3389/fncel.2017.00214.

[62] O. Elyamany, G. Leicht, C. S. Herrmann, and C. Mulert, “Transcranial alternating current stimulation (tACS): from basic mechanisms towards first applications in psychiatry,” *European Archives of Psychiatry and Clinical Neuroscience*, vol. 271, no. 1. 2021, doi: 10.1007/s00406-020-01209-9.

[63] S. Vogeti, C. Boetzel, and C. S. Herrmann, “Entrainment and Spike-Timing Dependent Plasticity – A Review of Proposed Mechanisms of Transcranial Alternating Current Stimulation,” *Frontiers in Systems Neuroscience*, vol. 16. 2022, doi: 10.3389/fnsys.2022.827353.

[64] A. L. Hodgkin and A. F. Huxley, “A quantitative description of membrane current and its application to conduction and excitation in nerve,” *Bull. Math. Biol.*, 1990, doi: 10.1007/BF02459568.

[65] B. Frankenhaeuser and A. F. Huxley, “The action potential in the myelinated nerve fibre of Xenopus laevis as computed on the basis of voltage clamp data,” *J. Physiol.*, vol. 171, no. 2, 1964, doi: 10.1113/jphysiol.1964.sp007378.

[66] C. C. McIntyre, A. G. Richardson, and W. M. Grill, “Modeling the excitability of mammalian nerve fibers: Influence of afterpotentials on the recovery cycle,” *J. Neurophysiol.*, vol. 87, no. 2, pp. 995–1006, 2002, doi: 10.1152/jn.00353.2001.

[67] C. H. Lubba *et al.*, “PyPNS: Multiscale Simulation of a Peripheral Nerve in Python,” *Neuroinformatics*, vol. 17, no. 1, 2019, doi: 10.1007/s12021-018-9383-z.

[68] F. Rattay, “Analysis of Models for External Stimulation of Axons,” *IEEE Trans. Biomed. Eng.*, 1986, doi: 10.1109/TBME.1986.325670.

[69] N. A. Pelot *et al.*, "Excitation properties of computational models of unmyelinated peripheral axons," *J. Neurophysiol.*, vol. 125, no. 1, 2021, doi: 10.1152/JN.00315.2020.

[70] B. J. Roth and P. J. Basser, "A Model of the Stimulation of a Nerve Fiber by Electromagnetic Induction," *IEEE Trans. Biomed. Eng.*, 1990, doi: 10.1109/10.55662.

[71] D. R. McNeal, "Analysis of a Model for Excitation of Myelinated Nerve," *IEEE Trans. Biomed. Eng.*, 1976, doi: 10.1109/TBME.1976.324593.

[72] M. V Mascagni and A. S. Sherman, "Numerical Methods for Neuronal Modeling," *Methods*, 1989, doi: 10.1.1.28.3083.

[73] S. Romeni, G. Valle, A. Mazzoni, and S. Micera, "Tutorial: a computational framework for the design and optimization of peripheral neural interfaces," *Nature Protocols*, vol. 15, no. 10. 2020, doi: 10.1038/s41596-020-0377-6.

[74] M. Stefano, F. Cordella, A. Loppini, S. Filippi, and L. Zollo, "A Multiscale Approach to Axon and Nerve Stimulation Modeling: A Review," *IEEE Transactions on Neural Systems and Rehabilitation Engineering*, vol. 29. 2021, doi: 10.1109/TNSRE.2021.3054551.

[75] H. A. M. Kamel and J. Toland, "Trigeminal nerve anatomy: Illustrated using examples of abnormalities," *Am. J. Roentgenol.*, vol. 176, no. 1, 2001, doi: 10.2214/ajr.176.1.1760247.

[76] G. Bathla and A. N. Hegde, "The trigeminal nerve: An illustrated review of its imaging anatomy and pathology," *Clinical Radiology*, vol. 68, no. 2. 2013, doi: 10.1016/j.crad.2012.05.019.

[77] S. Love and H. B. Coakham, "Trigeminal neuralgia: Pathology and pathogenesis," *Brain*, vol. 124, no. 12. 2001, doi: 10.1093/brain/124.12.2347.

[78] O. Medvedev *et al.*, "Perineural spread in head-and-neck malignancies: Imaging findings – An updated literature review," *Bosnian Journal of Basic Medical Sciences*, vol. 22, no. 1. 2022, doi: 10.17305/bjbms.2021.5897.

[79] C. A. Rodriguez-Russo, J. C. Junn, S. S. Yom, and R. L. Bakst, "Radiation therapy

for adenoid cystic carcinoma of the head and neck," *Cancers*, vol. 13, no. 24. 2021, doi: 10.3390/cancers13246335.

[80] R. Dessouky, Y. Xi, J. Zuniga, and A. Chhabra, "Role of MR neurography for the diagnosis of peripheral trigeminal nerve injuries in patients with prior molar tooth extraction," *Am. J. Neuroradiol.*, vol. 39, no. 1, 2018, doi: 10.3174/ajnr.A5438.

[81] M. Brant-Zawadzki, G. D. Gillan, and W. R. Nitz, "MP RAGE: A three-dimensional, T1-weighted, gradient-echo sequence - Initial experience in the brain," *Radiology*, vol. 182, no. 3, 1992, doi: 10.1148/radiology.182.3.1535892.

[82] A. M. Blitz *et al.*, "High-resolution ciss mr imaging with and without contrast for evaluation of the upper cranial nerves. segmental anatomy and selected pathologic conditions of the cisternal through extraforaminal segments," *Neuroimaging Clinics of North America*, vol. 24, no. 1. 2014, doi: 10.1016/j.nic.2013.03.021.

[83] Z. Zhang *et al.*, "3-T imaging of the cranial nerves using three-dimensional reversed FISP with diffusion-weighted MR sequence," *J. Magn. Reson. Imaging*, vol. 27, no. 3, 2008, doi: 10.1002/jmri.21009.

[84] O. Dietrich, J. G. Raya, S. B. Reeder, M. F. Reiser, and S. O. Schoenberg, "Measurement of signal-to-noise ratios in MR images: Influence of multichannel coils, parallel imaging, and reconstruction filters," *J. Magn. Reson. Imaging*, vol. 26, no. 2, 2007, doi: 10.1002/jmri.20969.

[85] H. Fujii *et al.*, "Visualization of the peripheral branches of the Mandibular division of the trigeminal nerve on 3D double-echo steady-state with water excitation sequence," in *American Journal of Neuroradiology*, 2015, vol. 36, no. 7, doi: 10.3174/ajnr.A4288.

[86] E. Burian *et al.*, "High resolution MRI for quantitative assessment of inferior alveolar nerve impairment in course of mandible fractures: an imaging feasibility study," *Sci. Rep.*, vol. 10, no. 1, 2020, doi: 10.1038/s41598-020-68501-5.

[87] A. J. Viera and J. M. Garrett, "Understanding interobserver agreement: The kappa statistic," *Fam. Med.*, vol. 37, no. 5, 2005.

[88] M. Piagkou, T. Demesticha, P. Skandalakis, and E. O. Johnson, "Functional anatomy of the mandibular nerve: Consequences of nerve injury and entrapment,"

Clinical Anatomy, vol. 24, no. 2. 2011, doi: 10.1002/ca.21089.

[89] F. van der Cruyssen *et al.*, "Magnetic resonance neurography of the head and neck: State of the art, anatomy, pathology and future perspectives," *British Journal of Radiology*, vol. 94, no. 1119. 2021, doi: 10.1259/bjr.20200798.

[90] J. Wen, N. S. Desai, D. Jeffery, N. Aygun, and A. Blitz, "High-Resolution Isotropic Three-Dimensional MR Imaging of the Extraforaminal Segments of the Cranial Nerves," *Magnetic Resonance Imaging Clinics of North America*, vol. 26, no. 1. 2018, doi: 10.1016/j.mric.2017.08.007.

[91] P. Hagmann, L. Jonasson, P. Maeder, J. P. Thiran, J. Van Wedeen, and R. Meuli, "Understanding diffusion MR imaging techniques: From scalar diffusion-weighted imaging to diffusion tensor imaging and beyond," *Radiographics*, vol. 26, no. SPEC. ISS., 2006, doi: 10.1148/rg.26si065510.

[92] C. Habas, "Basic principles of diffusion tensor MR tractography," *Journal de Radiologie*, vol. 85, no. 3. 2004, doi: 10.1016/s0221-0363(04)97579-8.

[93] S. T. Chen, J. T. Yang, M. Y. Yeh, H. H. Weng, C. F. Chen, and Y. H. Tsai, "Using diffusion tensor imaging to evaluate microstructural changes and outcomes after radiofrequency rhizotomy of trigeminal nerves in patients with trigeminal neuralgia," *PLoS One*, vol. 11, no. 12, 2016, doi: 10.1371/journal.pone.0167584.

[94] Y. Zhang *et al.*, "Diffusion Tensor Imaging of Axonal and Myelin Changes in Classical Trigeminal Neuralgia," *World Neurosurg.*, vol. 112, 2018, doi: 10.1016/j.wneu.2018.01.095.

[95] D. Q. Chen, D. D. DeSouza, D. J. Hayes, K. D. Davis, P. O'Connor, and M. Hodaie, "Diffusivity signatures characterize trigeminal neuralgia associated with multiple sclerosis," *Mult. Scler.*, vol. 22, no. 1, 2016, doi: 10.1177/1352458515579440.

[96] J. Upadhyay, J. Knudsen, J. Anderson, L. Becerra, and D. Borsook, "Noninvasive mapping of human trigeminal brainstem pathways," *Magn. Reson. Med.*, vol. 60, no. 5, pp. 1037–1046, Nov. 2008, doi: 10.1002/mrm.21682.

[97] A. Zolal *et al.*, "Comparison of probabilistic and deterministic fiber tracking of cranial nerves," *J. Neurosurg.*, vol. 127, no. 3, 2017, doi: 10.3171/2016.8.JNS16363.

[98] G. Xie *et al.*, "Anatomical assessment of trigeminal nerve tractography using diffusion MRI: A comparison of acquisition b-values and single- and multi-fiber tracking strategies," *NeuroImage Clin.*, vol. 25, 2020, doi: 10.1016/j.nicl.2019.102160.

[99] S. T. Chen, J. T. Yang, H. H. Weng, H. L. Wang, M. Y. Yeh, and Y. H. Tsai, "Diffusion tensor imaging for assessment of microstructural changes associate with treatment outcome at one-year after radiofrequency Rhizotomy in trigeminal neuralgia," *BMC Neurol.*, vol. 19, no. 1, 2019, doi: 10.1186/s12883-019-1295-5.

[100] H. Danyluk, T. Sankar, and C. Beaulieu, "High spatial resolution nerve-specific DTI protocol outperforms whole-brain DTI protocol for imaging the trigeminal nerve in healthy individuals," *NMR Biomed.*, vol. 34, no. 2, 2021, doi: 10.1002/nbm.4427.

[101] J. He *et al.*, "Comparison of multiple tractography methods for reconstruction of the retinogeniculate visual pathway using diffusion MRI," *Hum. Brain Mapp.*, vol. 42, no. 12, 2021, doi: 10.1002/hbm.25472.

[102] Y. Lilja, M. Ljungberg, G. Starck, K. Malmgren, B. Rydenhag, and D. T. Nilsson, "Tractography of Meyer's loop for temporal lobe resection—validation by prediction of postoperative visual field outcome," *Acta Neurochir. (Wien).*, vol. 157, no. 6, 2015, doi: 10.1007/s00701-015-2403-y.

[103] F. Zhang *et al.*, "Creation of a novel trigeminal tractography atlas for automated trigeminal nerve identification," *Neuroimage*, vol. 220, 2020, doi: 10.1016/j.neuroimage.2020.117063.

[104] J. G. Webster and M. Descoteaux, "High Angular Resolution Diffusion Imaging (HARDI)," in *Wiley Encyclopedia of Electrical and Electronics Engineering*, 2015.

[105] T. E. J. Behrens, H. J. Berg, S. Jbabdi, M. F. S. Rushworth, and M. W. Woolrich, "Probabilistic diffusion tractography with multiple fibre orientations: What can we gain?," *Neuroimage*, 2007, doi: 10.1016/j.neuroimage.2006.09.018.

[106] H. Seo and S. C. Jun, "Multi-scale computational models for electrical brain stimulation," *Frontiers in Human Neuroscience*, vol. 11. 2017, doi: 10.3389/fnhum.2017.00515.

[107] J. D. Griffiths, K. Shen, and P. Gleeson, "Editorial: Neuroinformatics of large-scale

brain modelling," *Frontiers in Neuroinformatics*, vol. 16. 2022, doi: 10.3389/fninf.2022.1043732.

[108] and A. C. McIntyre, Cameron C., J. Luis Lujan, "Methods for identifying target stimulation regions associated with therapeutic and non-therapeutic clinical outcomes for neural stimulation.," *U.S. Pat. 8,649,845*.

[109] N. De Geeter, G. Crevecoeur, A. Leemans, and L. Dupré, "Effective electric fields along realistic DTI-based neural trajectories for modelling the stimulation mechanisms of TMS," *Phys. Med. Biol.*, vol. 60, no. 2, pp. 453–471, 2015, doi: 10.1088/0031-9155/60/2/453.

[110] A. Nummenmaa *et al.*, "Targeting of white matter tracts with transcranial magnetic stimulation," *Brain Stimul.*, vol. 7, no. 1, pp. 80–84, 2014, doi: 10.1016/j.brs.2013.10.001.

[111] A. Indahlastari, A. Albizu, N. R. Nissim, K. R. Traeger, A. O'Shea, and A. J. Woods, "Methods to monitor accurate and consistent electrode placements in conventional transcranial electrical stimulation," *Brain Stimul.*, vol. 12, no. 2, 2019, doi: 10.1016/j.brs.2018.10.016.

[112] R. N. Holdefer, R. Sadleir, and M. J. Russell, "Predicted current densities in the brain during transcranial electrical stimulation," *Clin. Neurophysiol.*, vol. 117, no. 6, 2006, doi: 10.1016/j.clinph.2006.02.020.

[113] L. A. Geddes and L. E. Baker, "The specific resistance of biological material-A compendium of data for the biomedical engineer and physiologist," *Med. Biol. Eng.*, vol. 5, no. 3, 1967, doi: 10.1007/BF02474537.

[114] C. Gabriel, A. Peyman, and E. H. Grant, "Electrical conductivity of tissue at frequencies below 1 MHz," *Physics in Medicine and Biology*. 2009, doi: 10.1088/0031-9155/54/16/002.

[115] C. Gabriel, S. Gabriel, and E. Corthout, "The dielectric properties of biological tissues: I. Literature survey," *Phys. Med. Biol.*, 1996, doi: 10.1088/0031-9155/41/11/001.

[116] M. Akhtari *et al.*, "Conductivities of three-layer line human skull," *Brain Topogr.*, vol. 14, no. 3, 2002, doi: 10.1023/A:1014590923185.

[117] K. R. Foster and H. P. Schwan, “Dielectric properties of tissues and biological materials: a critical review.,” *Critical Reviews in Biomedical Engineering*, vol. 17, no. 1. 1989.

[118] J. L. Gaines, K. E. Finn, J. P. Slopsema, L. A. Heyboer, and K. H. Polasek, “A model of motor and sensory axon activation in the median nerve using surface electrical stimulation,” *J. Comput. Neurosci.*, vol. 45, no. 1, pp. 29–43, 2018, doi: 10.1007/s10827-018-0689-5.

[119] J. Cameron, “ Bioelectromagnetism-Principles and Applications of Bioelectric and Biomagnetic Fields, by J. Malmivuo and R. Plonsey ,” *Med. Phys.*, vol. 23, no. 8, 1996, doi: 10.1118/1.597895.

[120] J. Malmivuo and R. Plonsey, *Bioelectromagnetism: Principles and Applications of Bioelectric and Biomagnetic Fields*. 2012.

[121] M. L. Hines and N. T. Carnevale, “The NEURON Simulation Environment,” *Neural Computation*, vol. 9, no. 6. 1997, doi: 10.1162/neco.1997.9.6.1179.

[122] M. B. Iyer, U. Mattu, J. Grafman, M. Lomarev, S. Sato, and E. M. Wassermann, “Safety and cognitive effect of frontal DC brain polarization in healthy individuals,” *Neurology*, vol. 64, no. 5, 2005, doi: 10.1212/01.WNL.0000152986.07469.E9.

[123] T. Reed and R. Cohen Kadosh, “Transcranial electrical stimulation (tES) mechanisms and its effects on cortical excitability and connectivity,” *Journal of Inherited Metabolic Disease*, vol. 41, no. 6. 2018, doi: 10.1007/s10545-018-0181-4.

[124] S. Das, P. Holland, M. A. Frens, and O. Donchin, “Impact of transcranial direct current stimulation (tDCS) on neuronal functions,” *Frontiers in Neuroscience*. 2016, doi: 10.3389/fnins.2016.00550.

[125] B. V-Ghaffari, M. Kouhnavard, and T. Kitajima, “Biophysical properties of subthreshold resonance oscillations and subthreshold membrane oscillations in neurons,” *J. Biol. Syst.*, vol. 24, no. 4, 2016, doi: 10.1142/S0218339016500285.

[126] H. Bostock, C. S. Y. Lin, J. Howells, L. Trevillion, S. Jankelowitz, and D. Burke, “After-effects of near-threshold stimulation in single human motor axons,” *J. Physiol.*, vol. 564, no. 3, 2005, doi: 10.1113/jphysiol.2005.083394.

[127] T. Pashut *et al.*, "Mechanisms of magnetic stimulation of central nervous system neurons," *PLoS Comput. Biol.*, vol. 7, no. 3, 2011, doi: 10.1371/journal.pcbi.1002022.

[128] M. Bikson *et al.*, "Rigor and reproducibility in research with transcranial electrical stimulation: An NIMH-sponsored workshop," *Brain Stimulation*, vol. 11, no. 3. 2018, doi: 10.1016/j.brs.2017.12.008.

[129] B. Asamoah, A. Khatoun, and M. Mc Laughlin, "tACS motor system effects can be caused by transcutaneous stimulation of peripheral nerves," *Nat. Commun.*, vol. 10, no. 1, 2019, doi: 10.1038/s41467-018-08183-w.

[130] R. J. Sadleir, T. D. Vannorsdall, D. J. Schretlen, and B. Gordon, "Transcranial direct current stimulation (tDCS) in a realistic head model," *Neuroimage*, vol. 51, no. 4, 2010, doi: 10.1016/j.neuroimage.2010.03.052.

[131] A. M. Luckey, K. Adcock, and S. Vanneste, "Peripheral nerve stimulation: A neuromodulation-based approach," *Neuroscience and Biobehavioral Reviews*, vol. 149. 2023, doi: 10.1016/j.neubiorev.2023.105180.

[132] S. Ramaraju, M. A. Roula, and P. W. McCarthy, "Modelling the effect of electrode displacement on transcranial direct current stimulation (tDCS)," *J. Neural Eng.*, vol. 15, no. 1, 2018, doi: 10.1088/1741-2552/aa8d8a.

[133] E. Salkim, A. Shiraz, and A. Demosthenous, "Impact of neuroanatomical variations and electrode orientation on stimulus current in a device for migraine: A computational study," in *Journal of Neural Engineering*, 2020, vol. 17, no. 1, doi: 10.1088/1741-2552/ab3d94.

[134] C. Thomas, D. Q. Truong, K. Lee, C. Deblieck, X. M. Androulakis, and A. Datta, "Determination of Current Flow Induced by Transcutaneous Electrical Nerve Stimulation for the Treatment of Migraine: Potential for Optimization," *Front. Pain Res.*, vol. 2, 2021, doi: 10.3389/fpain.2021.753454.

[135] D. Sundt, N. Gamper, and D. B. Jaffe, "Spike propagation through the dorsal root ganglia in an unmyelinated sensory neuron: A modeling study," *J. Neurophysiol.*, vol. 114, no. 6, 2015, doi: 10.1152/jn.00226.2015.

[136] K. H. Hsu and D. M. Durand, "Prediction of neural excitation during magnetic

stimulation using passive cable models," *IEEE Trans. Biomed. Eng.*, vol. 47, no. 4, pp. 463–471, 2000, doi: 10.1109/10.828146.

[137] R. Haładaj, M. Polguj, and M. Topol, "Anatomical variations of the supraorbital and supratrochlear nerves: Their intraorbital course and relation to the supraorbital margin," *Med. Sci. Monit.*, vol. 25, 2019, doi: 10.12659/MSM.915447.

[138] L. F. Domeshek *et al.*, "Anatomic characteristics of supraorbital and supratrochlear nerves relevant to their use in corneal neurotization," *Eye*, vol. 33, no. 3, 2019, doi: 10.1038/s41433-018-0222-0.

[139] P. A. Heasman and A. D. G. Beynon, "Myelinated fibre diameters of human inferior alveolar nerves," *Arch. Oral Biol.*, vol. 31, no. 11, 1986, doi: 10.1016/0003-9969(86)90013-0.

[140] G. Cruccu *et al.*, "Trigeminal isolated sensory neuropathy (TISN) and FOSMN syndrome: Despite a dissimilar disease course do they share common pathophysiological mechanisms?," *BMC Neurol.*, vol. 14, no. 1, 2014, doi: 10.1186/s12883-014-0248-2.

[141] H. Nakayama, K. Noda, H. Hotta, H. Ohsawa, and Y. Hosoya, "Effects of aging on numbers, sizes and conduction velocities of myelinated and unmyelinated fibers of the pelvic nerve in rats," *J. Auton. Nerv. Syst.*, vol. 69, no. 2–3, 1998, doi: 10.1016/S0165-1838(98)00013-7.

[142] H. H. Hoffman and H. N. Schnitzlein, "The numbers of nerve fibers in the vagus nerve of man," *Anat. Rec.*, vol. 139, no. 3, 1961, doi: 10.1002/ar.1091390312.

[143] A. Antal *et al.*, "Low intensity transcranial electric stimulation: Safety, ethical, legal regulatory and application guidelines," *Clinical Neurophysiology*, vol. 128, no. 9. 2017, doi: 10.1016/j.clinph.2017.06.001.

[144] A. J. Woods, V. Bryant, D. Sacchetti, F. Gervits, and R. Hamilton, "Effects of electrode drift in transcranial direct current stimulation," *Brain Stimul.*, vol. 8, no. 3, 2015, doi: 10.1016/j.brs.2014.12.007.

[145] A. Indahlastari *et al.*, "The importance of accurately representing electrode position in transcranial direct current stimulation computational models," *Brain Stimulation*, vol. 16, no. 3. 2023, doi: 10.1016/j.brs.2023.05.010.

[146] F. Riederer, S. Penning, and J. Schoenen, “Transcutaneous Supraorbital Nerve Stimulation (t-SNS) with the Cefaly® Device for Migraine Prevention: A Review of the Available Data,” *Pain and Therapy*, vol. 4, no. 2. 2015, doi: 10.1007/s40122-015-0039-5.

[147] S. L. Helmers *et al.*, “Application of a computational model of vagus nerve stimulation,” *Acta Neurol. Scand.*, vol. 126, no. 5, 2012, doi: 10.1111/j.1600-0404.2012.01656.x.

[148] M. S. Chung *et al.*, “CS-VIBE accelerates cranial nerve MR imaging for the diagnosis of facial neuritis: comparison of the diagnostic performance of post-contrast MPRAGE and CS-VIBE,” *Eur. Radiol.*, 2021, doi: 10.1007/s00330-021-08102-6.

[149] K. Weber, “Neuromodulation and Devices in Trigeminal Neuralgia,” *Headache*, vol. 57, no. 10, 2017, doi: 10.1111/head.13166.

APPENDIX A

CRANI PROTOCOL DESIGN – PHANTOM TESTS.

In this phantom study we aimed to compare performance efficiency of recently developed T2-based MR sequence CRANI and MPRAGE and establish image acquisition parameters needed for clinical study design. The initial testing was done on a nerve phantom model before extending to humans.

Methods:

1. MRI sequences:

The 3D MPRAGE data was acquired using the following parameters: repetition time (TR)/echo time (TE) – 40/4ms, FOV - 224×224×120mm, slice thickness - 2.5mm, acquired voxel size - 2×2×2.5mm, multishot fast imaging mode with TFE factor – 56 and shot interval – 2500ms, number of slices – 48, number of averages - 4 and acquisition time - 11:22min.

The 3D CRANI data was acquired using the following parameters: TR/TE – 2300/150ms, FOV - 224×224×120mm, slice thickness - 2.5mm, acquired voxel size - 2×2×2.5mm, slice oversampling - 1.5, and number of slices - 48. TSE nerve STIR included TSE factor - 45 (startup echoes 2), number of averages - 4, black blood pulse - MSDE (mode: nerve), and acquisition time - 4:31min.

2. Nerve phantom design

An easy, cost-effective phantom model was created to represent nerves. Polyester ropes of different diameters were hung from a support and placed inside a beaker as shown in (Fig.1). The rope diameters were chosen to be larger than the slice thickness (2.5 mm) of the MR sequences for easier detection on images. Agarose-gel was prepared and poured into the beaker and left to cool (Fig. 1 (c)). This allowed the ropes to have different orientation and tortuosity inside the gel to mimic realistic differences in nerve geometries.

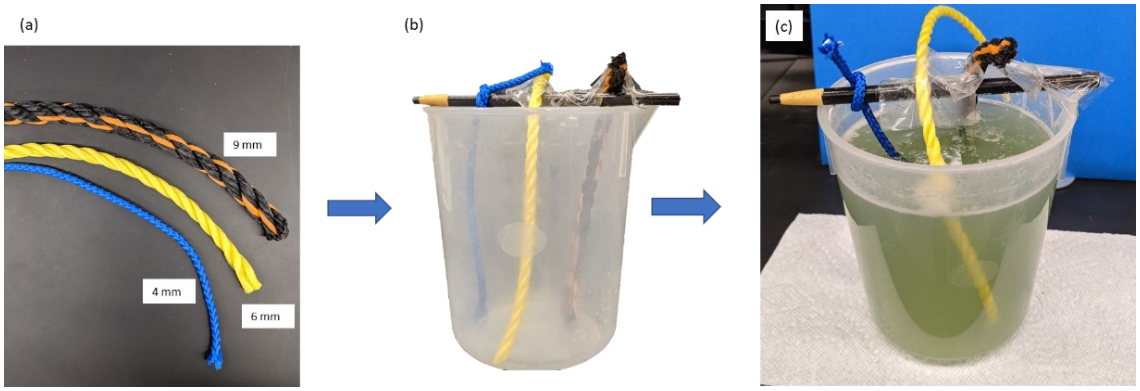

Figure 1: Nerve phantom design procedure. (a)Picture shows differences in diameters of the 3 ropes used. Picture (b) shows experimental setup inside the beaker and (c) shows corresponding setup after pouring agarose-gel.

3. Statistical analysis

For each case of different rope diameter, a region of interest (ROI) was drawn manually on the MPRAGE image by visually identifying a rope region (ROIrope) and an agarose-gel region (ROIgel). The ROIs were translated into the corresponding CRANI images. Contrast to noise ratio (CNR) was calculated to analyze performance of the two sequences. A Wilcoxon signed rank test was used to compare the CNRs obtained from MPRAGE and CRANI. Statistical significance was set to a value of $p<0.05$.

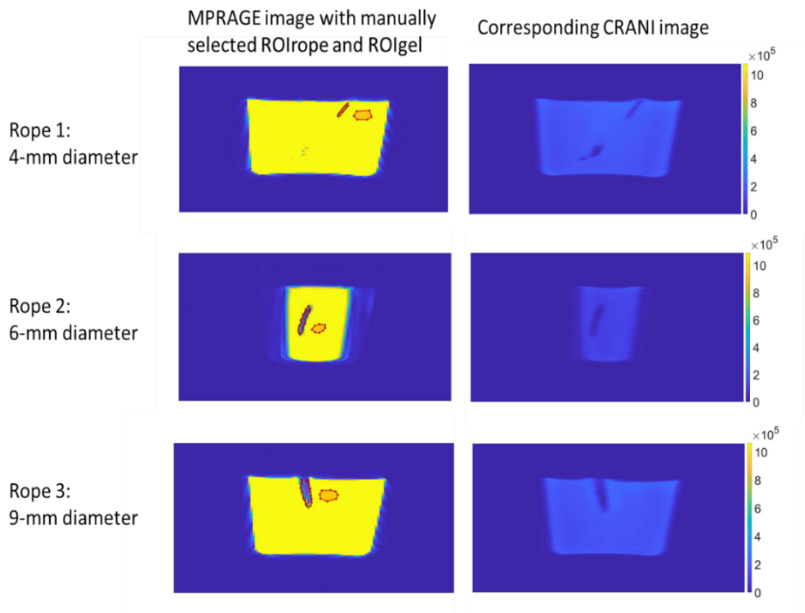

Figure 2: Images of the gel phantom. The first column represents MPRAGE data for every case with the ROIs drawn (red highlighted regions). The second column represents CRANI data corresponding to the same MPRAGE slice. The x and y dimensions in the graphs represent imaging matrix size of 124 × 124 mm^2. The colorbars represent signal intensity magnitudes.

Phantom testing results:

All three ropes in the phantom were visible in both MPRAGE and CRANI images. CNRs were calculated for both the sequences and a p value of 0.75 was seen from Wilcoxon signed rank tests implying no significant difference between the two CNRs. This implied that the image quality for 3D MPRAGE and 3D CRANI was similar. But image acquisition time was vastly different. The CRANI sequence had acquisition time of 4:31 min, almost a third of the MPRAGE acquisition time of 11:22 min. This indicates that CRANI is likely a better candidate for cranial nerve detection and tractography guidance in human subjects.